

# Modelling and diagnostics of forbidden emission lines in shocked atmospheres of Mira variables

vorgelegt von  
Dipl.-Phys. Heike Richter

Von der Fakultät II — Mathematik und Naturwissenschaften  
der Technischen Universität Berlin  
zur Erlangung des akademischen Grades  
Doktor der Naturwissenschaften (Dr. rer. nat.)

genehmigte Dissertation

Promotionsausschuß:

Vorsitzender: Prof. Dr. rer. nat. G. von Oppen

Berichter: Prof. Dr. rer. nat. E. Sedlmayr

Berichter: Priv. Doz. Dr. rer. nat. J. P. Kaufmann

Tag der wissenschaftlichen Aussprache: 24. Januar 2003

Berlin 2003

D 83



*Die geheimnisvollen Wirklichkeiten, die sich unseren Sinnen entzogen: die Naturkräfte, die Planeten, die Moleküle, die Wellen waren ein weites, riesiges Nichts, aus dem unsere Unwissenheit uns entgegensah und das wir unter Worten zu verstecken suchten.*  
Simone de Beauvoir, aus “Alle Menschen sind sterblich”



*This thesis is dedicated to Mount Stromlo Observatory  
... which burned to ashes in the devastating bushfires on the 18th of January 2003.*



# Zusammenfassung

Mira Veränderliche gehören zu der Klasse der Langperiodischen Veränderlichen (LPVs), in der Sterne mit geringer und mittlerer Anfangsmasse in einem späten Entwicklungsstadium auf dem asymptotischen Riesenast (AGB) zusammengefaßt werden. Die in solchen pulsierenden AGB-Objekten durch massive Sternwinde auftretenden erheblichen Massenverlusten von  $10^{-6} M_{\odot} \text{ yr}^{-1}$  werden in theoretischen Arbeiten (e.g. Fleischer 1992, Höfner & Dorfi 1997, Winters 2000a) durch ein Zusammenwirken von pulsationsbedingten Stoßwellen und Strahlungsdruck auf den dadurch gebildeten Staub erklärt. Obwohl Staub eine zentrale Rolle im Massenverlustmechanismus in den hydrodynamischen Modellen spielt, sind jedoch die Details des durch Stoßwellen getriggerte Staubbildungsmechanismus noch nicht vollständig geklärt. Insbesondere fehlte bislang eine Verknüpfung zwischen Modellen und Beobachtungen von Mira Atmosphären.

In dieser Arbeit werden verbotene und erlaubte Emissionslinien des einfach ionisierten Eisens (FeII) als diagnostisches Werkzeug zur Klärung dieser Problemstellung in M-Typ Miras (Elementenhäufigkeiten  $C/O < 1$ ) entwickelt. Diese Emissionslinien treten während des Minimums der visuellen Helligkeit auf. Es kann somit abgeschätzt werden, daß sie aus Bereichen von etwa  $r = 1.5 - 3 R_{*}$  emittiert werden, d.h. sie stammen etwa aus den äußeren Atmosphärenschichten, die für die Staub- und Windbildung dieser Objekte von entscheidender Bedeutung sind. Die in dieser Arbeit durchgeführten phasenabhängigen, hochaufgelösten Beobachtungen von Linienprofilen, -breiten sowie -flüssen dieser Emissionslinien (Richter & Wood 2001) liefern hierbei wichtige Erkenntnisse und Bedingungen für die theoretische Modellierung.

Die qualitative und quantitative Interpretation des Beobachtungsmaterials wird mit Hilfe detaillierter, zeitunabhängiger NLTE Linienstrahlungstransportrechnungen durchgeführt (Richter et al. 2002a,b). Diese werden auf Momentaufnahmen verschiedener Modellatmosphären gerechnet, wie sie im Zentrum für Astronomie und Astrophysik entwickelt wurden. So konnten die phasenabhängige Emission dieser Linien und die kritischen Faktoren für die Erzeugung passender Linienflüsse eingehend untersucht werden. Mit Hilfe detaillierter Parameterstudien wurden erstmals die essenziellen Stoßwellenparameter in den inneren Zonen von M-Typ Miras bestimmt. Diese Ergebnisse liefern entscheidende Parameter für die Anpaßung hydrodynamischer Modelle an Beobachtungen.

Die vorliegende Arbeit gliedert sich in drei wesentliche Teile: eine detaillierte Darstellung der Beobachtungsdaten (Kapitel 2), darauf folgend die Grundlagen des NLTE Strahlungstransports (Kapitel 3) und schließlich die Berechnung von FeII und [FeII] Linien zur Diagnostik von M-Typ Miras (Kapitel 4). Kapitel 5 schließt diese Arbeit mit einer Zusammenfassung sowie einem Ausblick auf zukünftige Arbeiten.





# Abstract

Mira variables belong to the class of Long Period Variables (LPVs), in which stars with low or intermediate initial masses are in a late state of their evolution on the Asymptotic Giant Branch (AGB). In such pulsating AGB-objects the high mass loss rates of  $10^{-6} \text{ M}_{\odot} \text{ yr}^{-1}$  caused by massive stellar winds are explained by theoretical works (e.g. Fleischer 1992, Höfner & Dorfi 1997, Winters 2000a) via a coaction of pulsational driven shock waves and radiative pressure on the thereby formed dust. Although dust plays a central role in the mass loss mechanism of the hydrodynamical models, the details of the dust formation process induced by shock waves is still not fully understood. In particular the connection between the models and observations of Mira atmospheres is so far still missing.

In this thesis, forbidden and permitted emission lines of single ionised iron (Fe II) are developed as a diagnostic tool in order to treat this problem in M-type Miras (element abundances  $\text{C/O} < 1$ ). These emission lines occur during the visible light minimum. It can therewith be estimated that they are emitted from regions around  $r = 1.5 - 3 \text{ R}_{*}$ , i.e. they originate approximately from the outer atmospheric layers which are of crucial importance for the dust and wind formation in these objects. The carried out time-resolved, high-resolution observations of line profiles, widths and fluxes of these emission lines (Richter & Wood 2001) yield important cognitions and conditions for the theoretical modelling.

The qualitative and quantitative interpretation of the observational data is carried out with the aid of detailed, time-independent NLTE radiative line transfer calculations (Richter et al. 2002a,b). These have been performed on snapshots of several model atmospheres, as developed in the Zentrum für Astronomie und Astrophysik. Therewith, the phase-dependent emission of these lines as well as the critical factors for the generation of the suitable line fluxes have been analysed in detail. Via detailed parameter studies the essential shock wave parameters in the inner zones of M-type Miras have been determined for the first time. These results provide vital parameters for an adaption of hydrodynamical models to the observations.

The presented work is subdivided into three fundamental parts: a detailed description of the observational data (chapter 2) followed by the basics of NLTE radiative transfer (chapter 3) and finally the calculation of Fe II and [F II] lines for the diagnostics of M-type Miras. Chapter 5 summarises this thesis with the conclusions and an outlook on future work.



# Contents

<b>1. Introduction</b>	<b>1</b>
<b>2. Time-resolved high-resolution observations of M-type Miras</b>	<b>5</b>
2.1. Details of the observations . . . . .	6
2.1.1. Instruments & resolution . . . . .	6
2.1.2. Julian dates & phases . . . . .	8
2.1.3. Emission line properties . . . . .	8
2.1.4. Data reduction . . . . .	9
2.1.5. Flux measurement . . . . .	9
2.2. Emission lines in M-type Miras . . . . .	10
2.2.1. Hydrogen lines . . . . .	10
2.2.2. Silicon line . . . . .	14
2.2.3. Magnesium lines . . . . .	16
2.2.4. Neutral iron lines . . . . .	18
2.2.5. Ionised iron lines . . . . .	22
2.2.6. Manganese line . . . . .	22
2.3. Phase-dependent variation of line fluxes . . . . .	24
2.4. Phase-dependent variation of line velocities . . . . .	28
2.5. Summary & conclusions . . . . .	30
<b>3. NLTE radiative line transfer</b>	<b>31</b>
3.1. Fundamentals of NLTE radiative transfer . . . . .	32
3.1.1. Motivation of the radiative transfer equation . . . . .	32
3.1.2. Time-independent, spherical symmetric equation in co-moving frame	32
3.1.3. Opacities . . . . .	34
3.1.3.1. Scattering opacity . . . . .	35
3.1.3.2. Continuum opacity . . . . .	36
3.1.3.3. Line opacity . . . . .	36
3.1.4. Profile function . . . . .	38
3.1.5. Rate equation . . . . .	39
3.1.6. Fe II-model-atom . . . . .	41
3.2. Solution methods . . . . .	43
3.2.1. The p-z-coordinates . . . . .	43
3.2.2. Feautrier method . . . . .	44

3.2.2.1.	Boundary conditions . . . . .	44
3.2.2.2.	Initial condition . . . . .	45
3.2.3.	The accelerated lambda iteration . . . . .	46
3.3.	The code nlte-feII . . . . .	48
<b>4.</b>	<b>Fe II &amp; Fe II f emission lines as a diagnostic tool in M-type Miras</b>	<b>51</b>
4.1.	Preliminary investigations . . . . .	53
4.1.1.	Stationary wind models . . . . .	53
4.1.2.	Models with artificial temperature peaks . . . . .	53
4.2.	Correlation of dust formation and Fe II & [Fe II] emission lines . . . . .	57
4.2.1.	Studies of the CHILD-code models . . . . .	58
4.2.2.	Studies of modified CHILD-code models . . . . .	61
4.2.3.	Investigation of Fe II & [Fe II] emission lines in a pulsation cycle . . . . .	63
4.2.4.	Emission region in the shock front . . . . .	68
4.3.	Thermodynamical conditions for Fe II & [Fe II] emission lines . . . . .	70
4.3.1.	Thermodynamical gas-box models . . . . .	71
4.3.2.	Variation of $\rho_{\text{pre}}$ . . . . .	72
4.3.2.1.	The effect of $\Delta v$ on Region A . . . . .	74
4.3.2.2.	Sample models . . . . .	76
4.3.3.	Variation of $\Delta v$ . . . . .	77
4.4.	Summary . . . . .	81
<b>5.</b>	<b>Conclusions &amp; Outlook</b>	<b>83</b>
<b>A.</b>	<b>Appendix</b>	<b>87</b>
	Literature . . . . .	90
	Acknowledgment . . . . .	95
	Lebenslauf . . . . .	97

# List of Figures

2.1. Structural system of the echelle spectrograph . . . . .	7
2.2. Balmer line profiles in RR Sco . . . . .	11
2.3. Balmer line profiles in R Aql . . . . .	12
2.4. Balmer line profiles in R Car . . . . .	12
2.5. Balmer line profiles in S Scl . . . . .	13
2.6. Balmer line profiles in R Hya . . . . .	13
2.7. Si I line profiles in RR Sco, R Aql, R Car, S Scl and R Hya . . . . .	14
2.8. Si I and Mg I narrow slit spectra for R Car, S Scl, R Leo and R Hya . . . . .	15
2.9. Mg I lines in RR Sco, S Scl, R Leo and R Hya . . . . .	15
2.10. Mg I lines in R Aql . . . . .	17
2.11. Mg I lines in R Car . . . . .	17
2.12. Fe I lines in RR Sco . . . . .	19
2.13. Fe I lines in R Car . . . . .	19
2.14. Fe I lines in S Scl . . . . .	20
2.15. Fe I lines in R Hya . . . . .	20
2.16. Fe I lines in R Aql . . . . .	21
2.17. Fe I lines in R Leo . . . . .	21
2.18. Fe II & Fe IIF lines in RR Sco and R Car . . . . .	23
2.19. Mn I & Fe IIF lines in R Leo . . . . .	23
2.20. Time sequence of the observed line fluxes . . . . .	24
2.21. Absolute line fluxes plotted against phase in R Leo and R Hya . . . . .	26
2.22. Absolute line fluxes plotted against phase in S Scl . . . . .	26
2.23. Absolute line fluxes plotted against phase in RR Sco and R Aql . . . . .	27
2.24. Absolute line fluxes plotted against phase in R Car . . . . .	27
2.25. Emission line velocities as a function of phase . . . . .	29
3.1. Scheme of the 3-level-model-atom . . . . .	41
3.2. Term diagram of Fe II . . . . .	42
3.3. p-z-coordinates . . . . .	43
3.4. Flow chart of the calculations. . . . .	49
4.1. Stationary wind model and resulting Fe II line fluxes . . . . .	55
4.2. Stationary model with artificial temperature peak & Fe II line fluxes . . . . .	56
4.3. Schema of the physical interplay in a Mira atmosphere . . . . .	59
4.4. Hydrodynamical model structure from CHILD-code & Fe II line fluxes . . . . .	60

4.5. Hydrodynamical model structure resulting from a CHILD-code with heating/cooling functions . . . . .	62
4.6. Time series of modified CHILD-code models — Formation of a shock at $\phi = 0.38$ . . . . .	64
4.7. Time series of modified CHILD-code models — First appearance of Fe II emission lines at $\phi = 0.40 - 0.42$ . . . . .	65
4.8. Time series of modified CHILD-code models — Evolution of Fe II emission lines at $\phi = 0.44 - 0.46$ . . . . .	65
4.9. Time series of modified CHILD-code models — Evolution of Fe II emission lines at $\phi = 0.48 - 0.50$ . . . . .	66
4.10. Time series of modified CHILD-code models — Dust formation at $\phi = 0.52 - 0.54$ and multicomponent Fe II emission line profiles . . . . .	66
4.11. Time series of modified CHILD-code models — Dust formation at $\phi = 0.56 - 0.58$ and multicomponent Fe II emission line profiles . . . . .	67
4.12. Time series of modified CHILD-code models — Noticeable dust condensation and disappearance of Fe II emission lines at $\phi = 0.60 - 0.62$ . . . .	67
4.13. Analysis of Fe II & Fe II $\lambda$ line emission region . . . . .	69
4.14. Parameter study I: fixed pairs of radial distance of the shock from the centre of the star $R$ and shock amplitude $\Delta v$ , varied pre-shock density $\rho_{\text{pre}}$ . . . . .	73
4.15. Variation of the shock velocity amplitude in parameter study I . . . . .	74
4.16. Exemplary models from parameter study I . . . . .	75
4.17. Parameter study II: fixed pairs of pre-shock density $\rho_{\text{pre}}$ and radial distance of shock from the centre of the star $R$ , varied shock amplitude $\Delta v$ . . . . .	79
4.18. Exemplary models from parameter study II . . . . .	80

# List of Tables

2.1. The M-type Mira sample . . . . .	5
2.2. Julian dates and phases of observation . . . . .	7
2.3. Metal emission line properties . . . . .	8
A.1. Mg I Line Fluxes . . . . .	87
A.2. H and Si I Line Fluxes . . . . .	88
A.3. Fe II and Fe IIF Line Fluxes . . . . .	88
A.4. Fe I Line Fluxes . . . . .	89
A.5. Fe I Line Fluxes continued . . . . .	90





# 1. Introduction

Long Period Variable Stars (LPVs) and Mira variables are essential stages in the late development of stars with low and intermediate mass on the asymptotic giant branch (AGB). About 95% – 98% of all stars (Habing 1996) — also our sun — will evolve into such pulsating AGB-stars, where via stellar winds a substantial fraction of their mass is given back to the interstellar medium (ISM). Therefore, these stellar winds are by far the most important sources for the enrichment of the ISM with processed material, out of which finally new stars are build. Miras and LPVs are therewith a significant stage in the cosmic circuit of matter.

According to the element abundance Miras and LPVs are divided into three groups: C-type stars which are carbon-rich ( $C/O > 1$ ), oxygen-rich M-type stars ( $C/O < 1$ ) and S-type stars ( $C/O \sim 1$ ), which are a transition stage between carbon-rich and oxygen-rich types. This thesis focuses on oxygen-rich M-type Mira stars. Their effective temperature is about  $T_{\text{eff}} \sim 2000 - 3000$  K (van Belle et al. 1997, Wallerstein & Knapp 1998) and they have high luminosities of  $L \sim 3 \cdot 10^3 - 8 \cdot 10^3 L_{\odot}$  (Habing 1996). The stellar radii of Mira stars are of about  $R \sim 150 - 600 R_{\odot}$  (Willson 1982, van Belle et al. 1997). Their light curves show regularly variations with periods of 300 – 500 d (Wallerstein & Knapp 1998, Habing 1996), where the amplitudes of the visual magnitudes are 2.5 – 7 mag (Wallerstein & Knapp 1998, Habing 1996).

Observations have shown that especially the pulsating objects have substantial dust envelopes: a strong correlation between infrared excess (indicating dust formation) and a considerable variation of the light curve (indicating pulsation) has been found for many late star types (Jura 1986). Hence, from an observational point of view the pulsation of the stars favours dust formation. Due to the oxygen-rich chemistry in the extended, cool circumstellar envelopes of the M-type Mira stars the dust mainly consists of silicate. Due to the radiative pressure on these dust particles the envelope gets accelerated and blown into the ISM, leading to very high mass loss rates bigger than  $10^{-6} M_{\odot} \text{ yr}^{-1}$  for M-type Miras (Habing 1996).

From a theoretical point of view the high mass loss can be explained being triggered by shocks, which are induced by the pulsation of the star (Wood 1979, Bowen 1988, Fleischer et al. 1992, Feuchtinger et al. 1993, Höfner & Dorfi 1997 and Winters et al. 2000a), namely the pulsation of the star generates shock waves which propagate through the atmosphere thereby increasing the mass density in the outer parts of the atmosphere. The passage of a shock leads to a sudden increase of the pressure, density and temperature of the gas. Behind the shock the gas cools via the emission of radiation,

which leads to conditions that are favourable for dust formation. As a consequence, the shocks in the outer parts of the atmosphere trigger the formation of dust. Radiation pressure acting on these dust grains finally drives the wind of these stars with high mass loss rates.

But although dust plays a central role in understanding the dynamics of Mira variables and moreover in driving mass loss in the hydrodynamical models, the details of the dust formation process as caused by shock waves is still not fully understood. Also it is still not proved whether the hydrodynamical models are consistent with the reality of Mira stars. A combination of detailed observations and theory is required to determine the thermodynamical conditions in the inner dust forming zones of M-type Mira stars and therewith shed some light on the dust formation in these variables.

For such a challenging task in particular forbidden emission lines of iron are very promising to be used as a diagnostic tool as it shall be motivated from a theoretical as well as from an observational view in the following.

In general radiative transfer modelling of emission lines reveals information about the temperature of the emitting region via its intensity and flux, but also gives information of the velocity of the emitting gas element via its Doppler shift. The density in the emitting volume can only roughly be confined by modelling the line profiles, since the width of the line corresponds to the pressure in the emitting volume, but is also influenced by other mechanisms (e.g. Doppler broadening). However, in particular forbidden emission lines give an additional density information of the emitting region. They are “forbidden” according to the selection rules of quantum mechanics hence their transition probabilities are very small. The forbidden transitions occur between metastable levels closely above the ground state and the ground state. The emission of forbidden lines is always connected to low densities, because otherwise collisions will de-populate the metastable level before a radiative forbidden transition can take place. Modelling a forbidden line will therewith offer the possibility to determine the full set of thermodynamical parameters which lead to their formation.

In particular the Fe II and [Fe II] emission lines are very enigmatic and conspicuous lines in the optical spectra of M-type Mira stars. Due to their detection around minimum light, they must be emitted in the shocked regions close to the photosphere of these stars. This is approximately the same region where dust is formed in the atmospheres of these stars. Additionally the erratic appearance of these particular emission lines in stars which had just had a bright light maximum suggests, that they require an exceptionally bright maximum for excitation (Richter & Wood 2001). Presumably, these are associated with stronger shock waves caused by the stellar pulsation. Since more than 60 years these highly interesting forbidden lines in M-type Miras are known (e.g. observed by Merrill 1940), but they have never been modelled in order to reveal the astrophysical insights they might imply.

The particular aim of this thesis is to combine high resolution observations of M-type Miras with detailed NLTE radiative transfer calculations performed on self-consistent thermodynamical models in order to reveal the information given by these emission lines and furthermore to examine their connection to the dust formation in the atmospheres.

This thesis therewith aims to approach the long outstanding questions:

- Do the FeII and [Fe II] emission lines get excited by shocks in M-type Miras?
- If so, in which part of the shock do they get excited (post-shock, pre-shock)?
- Is there a connection between dust formation and the appearance of those lines in M-type Mira variables?
- Where do these lines form in the atmosphere of M-type Miras?
- Which specific thermodynamical parameters lead to the formation of these erratic lines?

The work presented in this thesis is structured into four main parts.

**Chapter 2** presents the time-resolved, high-resolution observations of a M-type Mira sample carried out in 1999 at Mount Stromlo Observatory, Canberra, Australia. The technical details of the used instruments and their resolution are outlined. Furthermore, the Julian dates of the observations and corresponding phases of the Mira variables are given, as well as the emission line properties are tabulated. A brief overview on the used data reduction technique and the carried out flux measurement is also presented.

Following, detailed line profiles, widths, fluxes and velocities of Balmer lines as well as various metal emission lines are given for all stars of the sample, where a special focus is put on the FeII and [Fe II] emission lines. The phase-dependent variation of all line fluxes as well as line velocities are analysed in detail.

A summary highlighting the first basic results of the FeII and [Fe II] emission lines closes this chapter.

**Chapter 3** outlines the fundamentals of the NLTE radiative transfer theory. In particular the time-independent, spherical symmetric radiative transfer equation in the co-moving frame is highlighted. It is also motivated why this description is appropriate to use for the calculations of FeII and [Fe II] emission lines in Mira atmospheres. A brief characterisation of the opacities and profile function is given, followed by a presentation of the used rate equation. Next, the FeII-model-atom utilised in the NLTE radiative transfer calculations is described.

Following, the p-z-coordinates which are convenient for the numerical treatment of the spherical symmetric atmosphere are introduced. The Feautrier method and the according boundary and initial conditions are presented in greater detail. The basic ideas of the accelerated lambda iteration, which is necessary to solve the NLTE radiative transfer with included scattering terms, are outlined.

Finally the utilised NLTE radiative transfer code `nlte-feII` which is based on the presented theory and assumptions is described.

**Chapter 4** presents a detailed theoretical modelling of the Fe II and [Fe II] emission lines in order to prove that they can be used as a diagnostic tool. The application of those lines to probe the M-type Mira atmospheres is then explicitly described. Preliminary investigations of stationary models as well as models with an artificially inserted high temperature peak are presented, which point out that shocks must be present in the atmosphere in order to produce these emission lines.

Consequently, next detailed hydrodynamical models with self-consistently treated formation and destruction of dust are analysed. A time series of such models allows to analyse the potential correlation between dust formation and the appearance of Fe II and [Fe II] emission lines.

For a determination of the exact thermodynamical conditions leading to the emission of Fe II and [Fe II] lines detailed thermodynamical models of periodical shock waves for a dust-free, oxygen-rich gas composition are utilised. The two carried out extended parameter studies are described in greater detail, which finally lead to the determination of appropriate shock parameters in the inner dust-forming regions of M-type Mira variables.

A summary of the achieved results of each investigation ends this chapter.

**Chapter 5** summaries this thesis by giving the conclusions of this work and outlining possible future work.

## 2. Time-resolved high-resolution observations of M-type Miras

The time-resolved high-resolution observations of cool, shock penetrated, expanding atmospheres of M-type Mira stars were carried out in a collaboration with Dr. P. R. Wood at Mount Stromlo Observatory, Canberra, Australia in 1999. The star sample consisted of the M-type Miras: RR Sco, R Aql, R Car, R Leo, S Scl and R Hya, which range in period from 281 days to 389 days. Additional data concerning the sample, e.g. spectral types and heliocentric stellar centre-of-mass velocities, are given in Tab. 2.1<sup>1</sup>. Quantitative data on the shapes, widths and fluxes of metallic emission lines of Fe I, Mg I, Mn I and Si I — in particular of Fe II and [Fe II] — as well as hydrogen emission lines H $\gamma$ , H $\delta$ , H $\zeta$ , H $\eta$  were observed. The observations presented here have already been published in Richter & Wood (2001).

Table 2.1.: The M-type Mira sample

Star	P [days]	Sp.	$v_*$ [km/s]
RR Sco	281	M6e-M9e	-37 <sup>a</sup>
R Aql	284	M5e-M9e	29 <sup>b</sup>
R Car	309	M4e-M8e	20 <sup>c</sup>
R Leo	310	M6e-M9.5e	6 <sup>b</sup>
S Scl	363	M3e-M9e(Tc)	(12)
R Hya	389	M6e-M9eS(Tc)	-11 <sup>b</sup>

<sup>a</sup>  $V_*$  from the midpoint of the CO J=3–2 transition (Young 1995)

<sup>b</sup>  $V_*$  from the midpoint of the CO J=2–1 transition (Cernicharo et al. 1997)

<sup>c</sup>  $V_*$  from the midpoint of the SiO J=3–2,  $v=0$  transition (Groenewegen et al. 1999)

The aim of our observations has been to study in particular the various metal emission lines, which appear from visible light maximum to minimum. According to the phase of their appearance one gets information about the thermodynamical parameters in the according atmospheric layers that the shock is passing. In particular the observed Fe II

---

<sup>1</sup>Periods and spectral types taken from the index to variable stars of the Variable Star Network (VSNET), Nogami et al. (1997). Heliocentric stellar centre-of-mass velocity  $v_* \pm 2 \text{ km s}^{-1}$  determined from the midpoint of the circumstellar molecular emission of CO or SiO from papers cited below the table.

and [Fe II] emission lines (multiplets M 38, 6F, 7F and 21F; see Tab. 2.3) are outstanding, because deduced from their phase of appearance around minimum visible light, they must be emitted in the shocked regions close to the photosphere of these stars. This is approximately the same region where dust is formed. Hence, these emission lines are the most promising candidates to be developed as a diagnostic tool to study the dust-forming regions close to the photosphere of M-type Mira atmospheres. Additionally, it has been noted in the observations that these emission lines do not appear in every pulsational cycle, but that their emission is rather connected to particular strong shocks (see this chapter for details). This on the one hand made the collection of data more difficult, but on the other hand offers the big advantage to use their subsequent detailed modelling to derive upper limits for the thermodynamical conditions in the dust forming layers.

These Fe II and [Fe II] emission lines have already been observed by Joy (1954) in the M Mira  $\alpha$  Ceti as well as by Merrill (1940; 1947b) in the M-type Miras U Ori, R Leo, R Hya and the S-type Mira  $\chi$  Cyg. However, existing spectral observations have mostly concentrated on the mean radial velocities of these lines. There is very little published quantitative data on the shapes, widths and fluxes of metal emission lines. Consequently the aim of this part of the presented work has been to provide this essential data for the subsequent detailed modelling.

In the following the observational instruments and techniques are briefly outlined in Sec. 2.1. Then Sec. 2.2 demonstrates the variety of the observed emission lines in the M-type Mira sample. Details of the phase-dependent appearance of all emission lines in the pulsation cycle are specified and the line profiles of all observed emission lines are given, where a special focus is put on the Fe II and [Fe II] emission lines. Furthermore an overview on the variation of observed line fluxes is presented in Sec. 2.3. Next the time evolution of measured line velocities with phase is presented in details in Sec. 2.4. A summary of the observational results ends this chapter.

## 2.1. Details of the observations

### 2.1.1. Instruments & resolution

The observed high-resolution line spectra of the M-type Mira sample were obtained with the coudé echelle spectrograph and an 81 cm camera of the Mount Stromlo Observatory 74-inch telescope. Fig. 2.1 depicts the structural system of the echelle spectrograph. The spectral resolution of such a spectrograph is about  $A = n N \leq 10^5$  (n: order, N: grating groove), where the echelle grating is working in high orders up to  $n \sim 10 - 1000$ . The overlapping orders will then be separated across the dispersion direction by the second grating of low spectral resolution namely the cross-disperser. Effectively the spectrum is cut into dozens of small pieces (also called orders). The big advantage of an echelle spectrograph is that a wide wavelength coverage with high-resolution is achieved in one exposure. As a detector a Site  $2 \times 4k$  CCD was used, allowing coverage of the spectral region 3600–5700 Å in each exposure: the corresponding spectral range in each echelle

order was 70–60 Å. The echelle grating gave a dispersion of  $0.0204 \text{ Å pixel}^{-1}$  at  $4000 \text{ Å}$ , equivalent to  $1.53 \text{ km s}^{-1} \text{ pixel}^{-1}$ .

Maximum resolution observations were done with a  $300 \text{ μm}$  (1.2 arcsec) slit, giving a 3-pixel resolution of  $4.6 \text{ km s}^{-1}$ . For spectrophotometric observations, a  $1500 \text{ μm}$  (6 arcsec) slit was used, giving a resolution of  $15.3 \text{ km s}^{-1}$ . Because of the high slit losses experienced with the  $300 \text{ μm}$  slit, and the fact that the emission lines are mostly considerably broader than  $15.3 \text{ km s}^{-1}$ , a large fraction of all observations were in fact done using the wide slit.

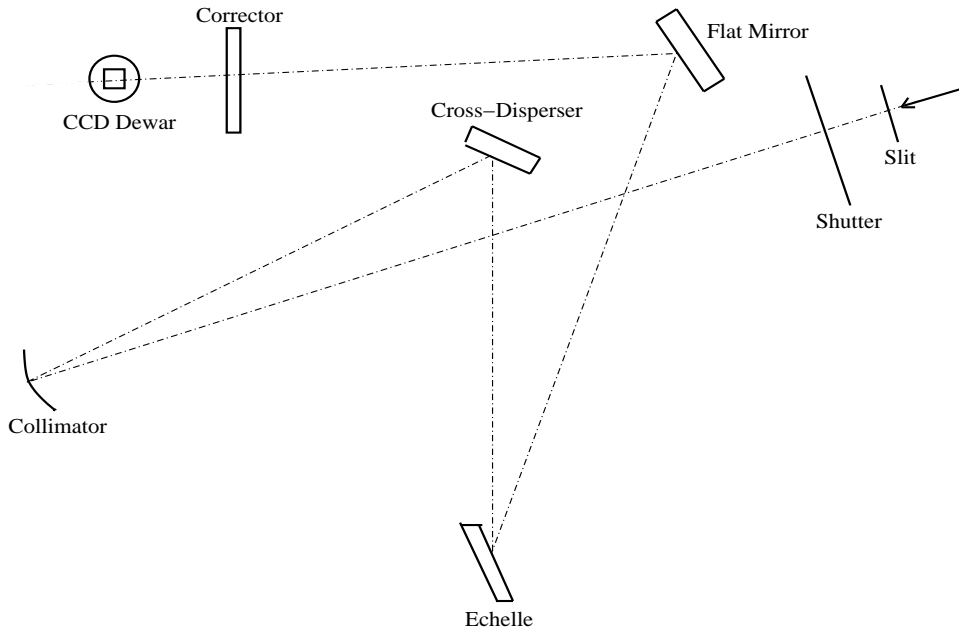


Figure 2.1.: The echelle spectrograph (grating  $31.6 \text{ g mm}^{-1}$ ) which is mounted in the coudé focus of the 74-inch telescope at Mount Stromlo Observatory.

Table 2.2.: Julian dates and phases of observation

JD <sup>a</sup>	Phase					
	RR Sco	R Aql	R Car	R Leo	S Scl	R Hya
1153	-	-	-0.16	-	-	-
1169	-	-	-	-	0.02	-
1206	-	-	-0.09	0.43	-	-
1268	-	0.01	0.11	0.63	-	-
1357	0.29	0.32	0.39	-	0.52	0.08
1375	-	0.39	0.45	-	0.58	0.12
1412	0.48	0.50	0.57	-	0.67	0.21
1440	0.58	-	0.66	-	0.75	-
1464	-	0.69	-	-	-	-
1542	-	-	-	1.49	-	0.53

<sup>a</sup> Julian date - 2450000.

### 2.1.2. Julian dates & phases

Table 2.2 lists the Julian dates and the corresponding phases for the variables observed. The phases for each observation of every Mira variable of the sample were determined from the AAVSO<sup>2</sup> (Mattei et al. 1980) maxima: phase zero corresponds to visible maximum. The Mira sample has been observed at multiple phases of the pulsation cycle, so that half a pulsation cycle from maximum visible light to minimum visible light was covered, which offers the possibility to trace the shock front on its way through the Mira atmospheres.

### 2.1.3. Emission line properties

Balmer lines  $H\gamma$  (4340.46 Å),  $H\delta$  (4101.73 Å),  $H\zeta$  (3889.05 Å) and  $H\eta$  (3835.38 Å) were observed near maximum visible light in order to get the shock velocity deep in the atmosphere. Between maximum and minimum light a search was carried out for emission lines of the metals Mg I, Si I, Mn I, Fe I and especially Fe II. Table 2.3 lists the multiplet number M, wavelength  $\lambda$ , upper and lower energy levels of the transition  $E_u$  and  $E_l$ , and the Einstein-coefficients  $A_{ul}$  for the metal emission lines observed. This data was obtained from the NIST database<sup>3</sup> (Fuhr et al. 1988). Note that the detected lines include the forbidden lines of the multiplets [Fe II] 6F, [Fe II] 7F and [Fe II] 21F.

Table 2.3.: Metal emission line properties

Ion	M	$\lambda[\text{\AA}]$	$E_u[\text{cm}^{-1}]$	$E_l[\text{cm}^{-1}]$	$A_{ul}[\text{s}^{-1}]$
Si I	2	4102.95	39760	15394	9.6+4
Mn I	2	4030.75	24802	0	1.7+7
Mg I	1	4571.10	21870	0	2.2+2
	3	3829.32	47957	21850	8.9+7
	3	3832.35	47957	21870	6.7+7
	3	3838.29	47957	21911	4.5+6
	3	3838.29	47957	21911	4.5+6
Fe I	2	4461.65	23111	704	2.9+4
	2	4375.93	22846	0	2.9+4
	3	4216.18	23711	0	1.8+4
	42	4307.90	35768	12560	3.4+7
	42	4202.03	35768	11976	8.2+6
	73	3852.57	32499	17550	2.9+6
	828	4427.30	22997	416	3.4+4
	38	4583.84	44449	22637	3.8+5
	38	4583.84	44449	22637	3.8+5
Fe II	6F	4457.95	22810	385	2.9-1
	7F	4359.33	23318	385	1.1+0
	7F	4287.39	23318	0	1.5+0
	21F	4276.83	25805	2430	6.5-1
	21F	4243.97	25429	1872	9.0-1

<sup>2</sup><http://www.aavso.org/adata/curvegenerator.shtml>

<sup>3</sup>[http://physics.nist.gov/cgi-bin/AtData/main\\_asd](http://physics.nist.gov/cgi-bin/AtData/main_asd)



#### 2.1.4. Data reduction

For data reduction, the Image Reduction and Analysis Facility (IRAF) of the National Optical Astronomy Observatories was used, a standard tool for data reduction, which can be obtained from the internet<sup>4</sup> including various tutorials for introduction. In IRAF the tool `doecslit` was used to reduce the echelle data.

For the wavelength calibration of the high-resolution spectra a reference spectrum is needed, which was obtained from thorium-argon arcs taken during each run. Similarly reference standard star spectra are needed for the calibration of the spectra to absolute fluxes. Here observations on photometric nights of each run of the the standard stars HR 718, HR 3454 or HR 7596 were used. The calibrated fluxes from multiple observations of standard stars during each night were compared to estimate the errors in the fluxes: these comparisons indicate that the flux errors should be less than 5%. This error is much less than the typical variation of flux throughout the pulsation cycle.

#### 2.1.5. Flux measurement

In the case of non-photometric nights, the absolute fluxes have been estimated from the spectra by assuming that the flux in the V band at 5100 Å (a quasi-continuum point) varies in the same way as the light curves of the American Association Of Variable Star Observers (AAVSO). With this method the continuum flux has been estimated at 5100 Å by scaling the non-photometric flux relative to the calibrated flux from a photometric night. The flux then has been calibrated at other wavelengths using the relative spectral response of the spectrograph. The line fluxes obtained in this way are marked with a colon in the flux tables in appendix A.

In order to derive the emission line fluxes, it is necessary to have an estimate of the continuum level. This was estimated by eye: initially, the whole order containing the line was examined to get an idea of the overall continuum shape, then a wavelength interval on either side of the line approximately equal to the line width was used for the final estimate. In the case of P-Cygni line profiles, the associated absorption was ignored in the continuum estimate. For strong emission lines (ex. Balmer lines), the continuum level is not a significant contributor to line flux errors, but in the case of weak emission lines in these stars which exhibit many absorption lines, the continuum level can be a major contributor to the flux error. In the worst cases, the flux could be wrong by a factor of 2.

---

<sup>4</sup><http://iraf.noao.edu/iraf-homepage.html>

## 2.2. Emission lines in M-type Miras

In the following all observed emission lines of the M-type Mira sample are presented in the order of their appearance in phase with the according total line fluxes  $F_{\text{tot}}$  ( $\text{erg cm}^{-2} \text{s}^{-1}$ ) and peak flux  $F_{\text{peak}}$  ( $\text{erg cm}^{-2} \text{s}^{-1} \text{\AA}^{-1}$ ) given in tables in appendix A. Note that the peak flux can be used in conjunction with the plotted profiles (except for the narrow slit observations) to get intensities through the line profiles.

The presented line profiles are plotted against velocity rather than wavelength, because the atmospheric kinematics associated with pulsation shall be analysed. The spectra have been positioned horizontally so that line emission in the rest frame of the star will appear at zero velocity (stellar centre-of-mass velocities from Table 2.1 have been adopted). A positive velocity indicates a motion outward from the centre of the star, and visa versa. Most of the observations in the plots were taken with a wide slit (left panels), additionally selected observations taken with a narrow slit with higher velocity resolution are presented in the right panels to give a comparison.

### 2.2.1. Hydrogen lines

The observed line profiles of the Balmer lines  $\text{H}\gamma$ ,  $\text{H}\delta$ ,  $\text{H}\zeta$  and  $\text{H}\eta$  are presented in Figs. 2.2–2.6 for RR Sco, R Aql, R Car, S Scl and R Hya. Unfortunately because of its position in the sky and the phase of its light curve, R Leo was not observable near maximum when the Balmer lines were in emission, but we did observe it during two different minima.

Since the Balmer lines have intrinsic full widths of  $\sim 80 \text{ km s}^{-1}$ , clearly the instrumental broadening of the wide slit ( $15.3 \text{ km s}^{-1}$ ) does not influence the line profiles significantly. As presented in the spectra, the main result is the change in the overall line shape with phase. The full base width (hereinafter FBW) of the hydrogen lines is around  $80 \text{ km s}^{-1}$  when they first appear. Then with increasing phase, the hydrogen lines become weaker and more narrow ( $\text{FBW} \sim 60\text{--}70 \text{ km s}^{-1}$ ). Generally the emission lines are centred around an outward velocity of  $\sim 10 \text{ km s}^{-1}$ . Previous studies of the hydrogen lines in Miras (e.g. Fox et al. 1984) have shown similar results.

It is also noticeable that the strengths of the overlying absorption features decreases with advancing phase. Joy (1947) identified absorption lines of TiO in  $\text{H}\gamma$ , of Fe I and VI in  $\text{H}\delta$  and of Ti I in  $\text{H}\zeta$ . A decrease in absorption with increasing phase is just as expected in a model where the shock producing the emission lines moves above more of the atmosphere as time progresses. Additionally the strength of the absorption features seems to vary from star to star; for instance, superimposed absorption in  $\text{H}\gamma$  is stronger in R Aql than in S Scl at comparable phases (compare Fig. 2.3  $\phi=0.01$  and Fig. 2.5  $\phi=0.02$ ). Fox et al. (1984) noted a comparable variation of overlying absorption line strength from star to star and suggested that this could be due to a cycle-to-cycle variation in shock strength: at fainter maxima weaker shocks are formed and they are not able to propagate out through as much overlying absorbing material, leading to stronger absorption.

A remarkable result in RR Sco is the appearance of faint Balmer lines at the very

early phase  $\phi=0.58$  (Fig. 2.2). These emission lines are strongly dominated by overlying absorption, as expected. Maybe they are also evidence for an unusually strong shock emerging from the star in the particular observed pulsation cycle.

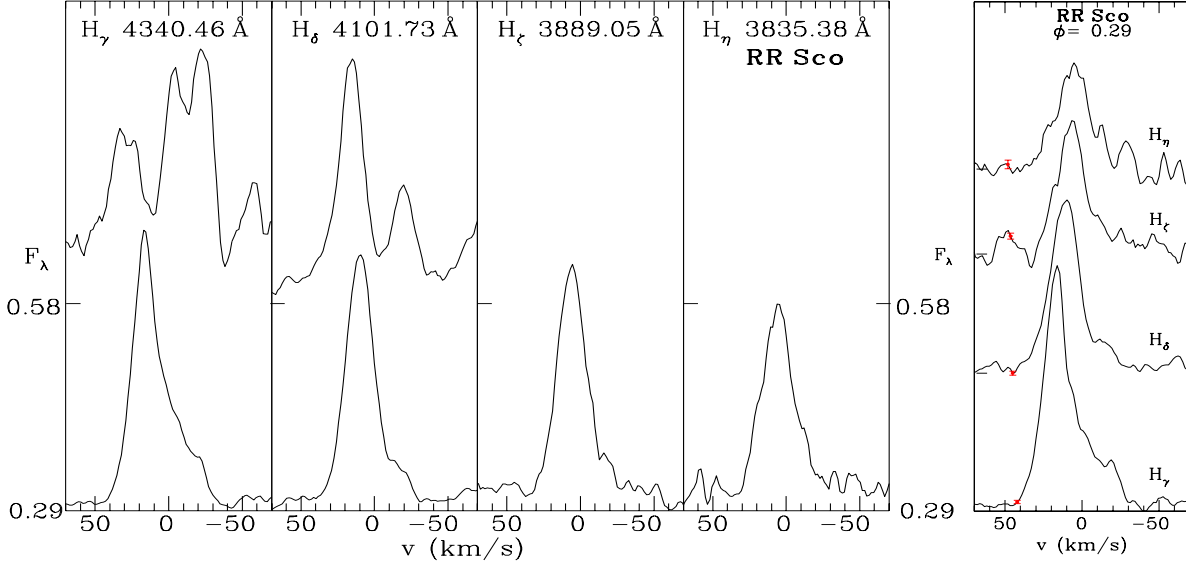


Figure 2.2.: *Left:* Line profiles of H $\gamma$ , H $\delta$ , H $\zeta$ , H $\eta$  as a function of phase in RR Sco. The observations were made with a wide (1500  $\mu\text{m}$ ) slit.  $F_\lambda$  is plotted vertically, with the zero flux level for each spectrum being indicated by a tick mark on the vertical axis. The phase of the observation is indicated next to each tick mark. Note that the height of the profiles is arbitrary as we scaled them with different factors. Table A.2 in appendix A lists the maximum flux level in each line. The horizontal axis corresponds to wavelength  $\lambda$  (i.e. velocity). The spectra have been positioned horizontally so that line emission in the rest frame of the star will appear at zero velocity (stellar centre-of-mass velocities from Table 2.1 have been adopted). Positive velocities correspond to motion outward from the centre-of-mass (i.e.  $\lambda$  increases to the right). *Right:* The Balmer line profiles observed with a narrow (300  $\mu\text{m}$ ) slit at phase  $\phi = 0.29$ , shown for comparison with the wide slit observations ( $\sigma$ -error bars are indicated).

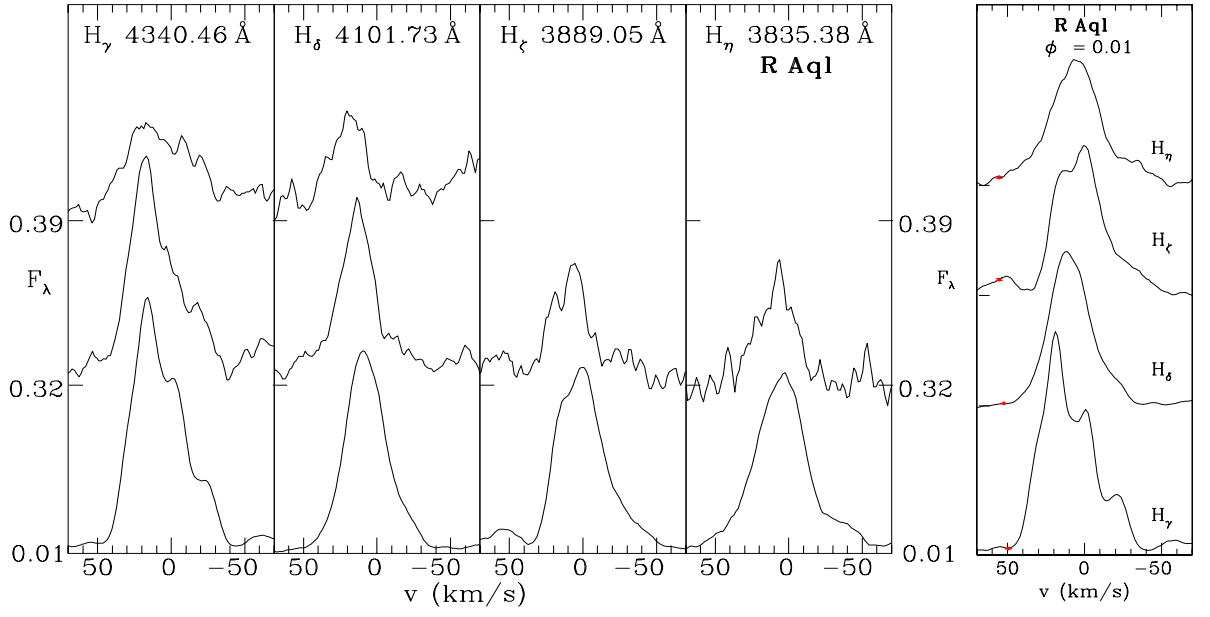


Figure 2.3.: *Left*: Line profiles of  $H\gamma$ ,  $H\delta$ ,  $H\zeta$ ,  $H\eta$  as a function of phase in R Aql (see Fig. 2.2 for details). *Right*: The Balmer line profiles observed with a narrow ( $300\ \mu\text{m}$ ) slit at phase  $\phi = 0.01$ .

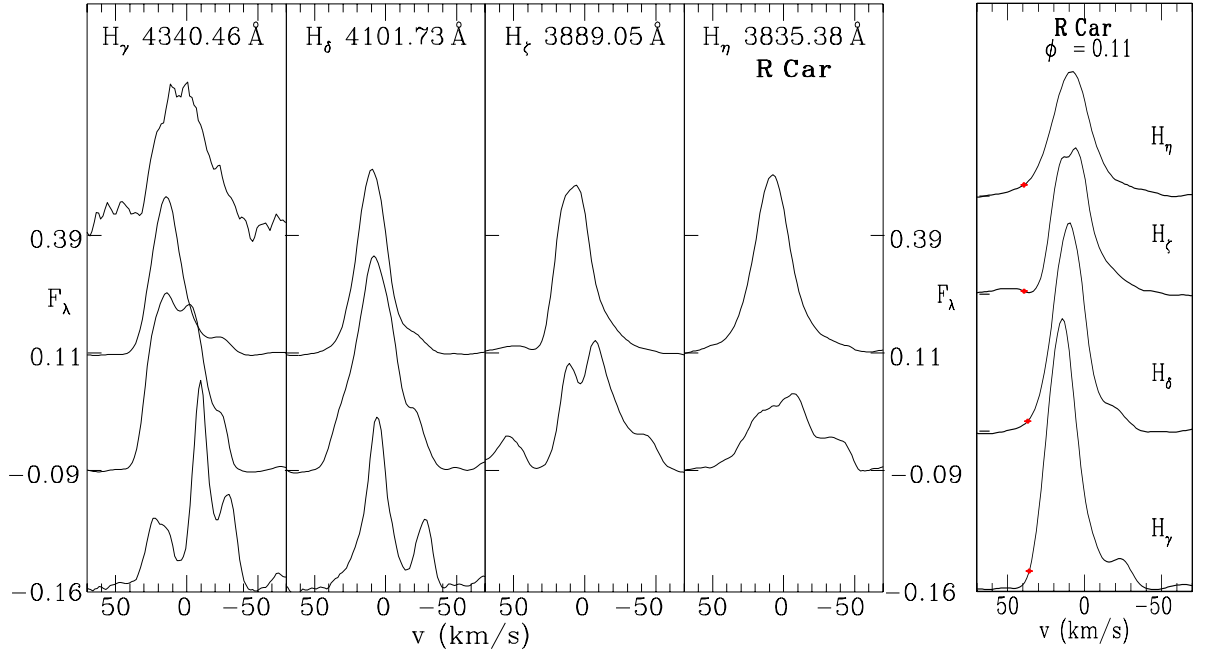


Figure 2.4.: *Left*: Line profiles of  $H\gamma$ ,  $H\delta$ ,  $H\zeta$ ,  $H\eta$  as a function of phase in R Car (see Fig. 2.2 for details). *Right*: The Balmer line profiles observed with a narrow ( $300\ \mu\text{m}$ ) slit at phase  $\phi = 0.11$ .

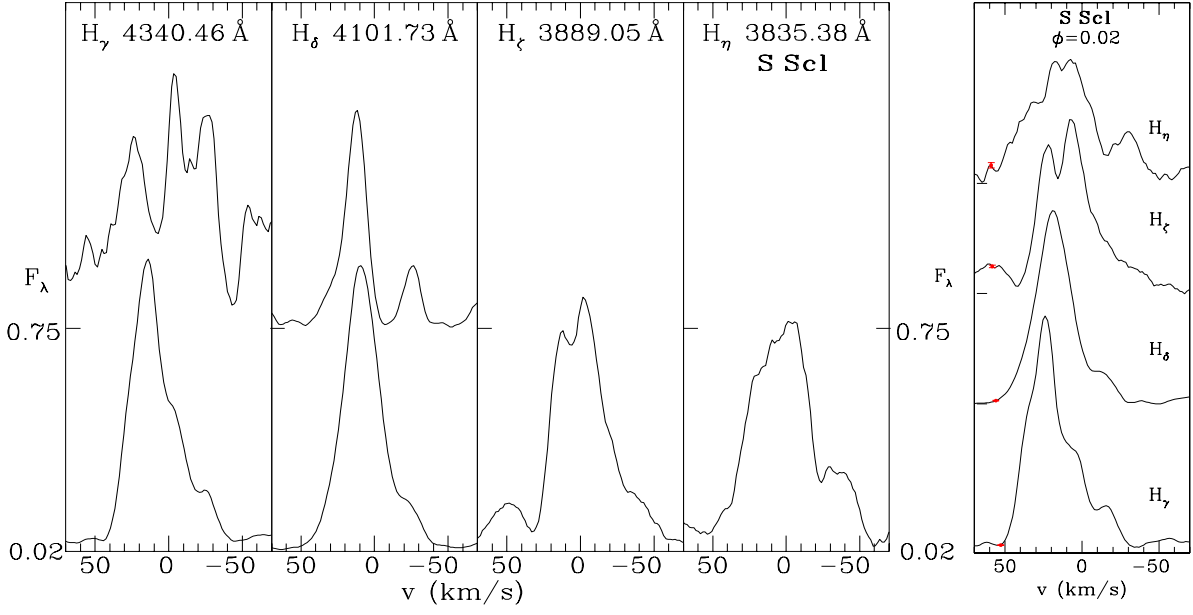


Figure 2.5.: *Left*: Line profiles of  $H\gamma$ ,  $H\delta$ ,  $H\zeta$ ,  $H\eta$  as a function of phase in S Scl (see Fig. 2.2 for details). *Right*: The Balmer line profiles observed with a narrow ( $300\mu\text{m}$ ) slit at phase  $\phi = 0.02$ .

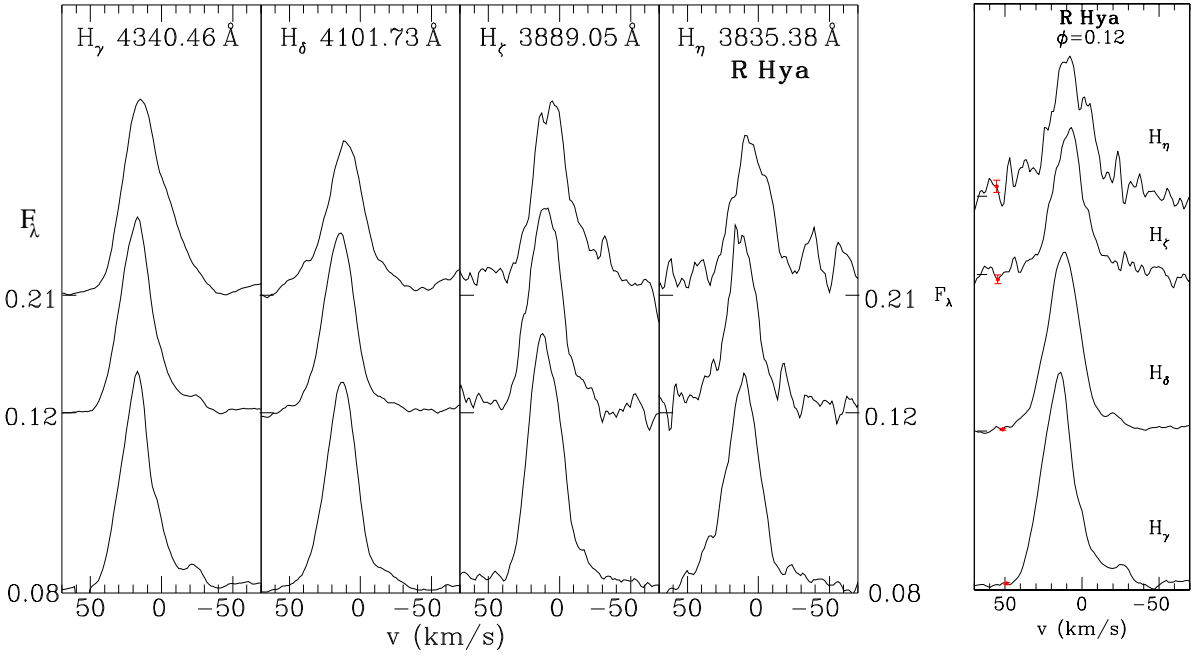


Figure 2.6.: *Left*: Line profiles of  $H\gamma$ ,  $H\delta$ ,  $H\zeta$ ,  $H\eta$  as a function of phase in R Hya (see Fig. 2.2 for details). *Right*: The Balmer line profiles observed with a narrow ( $300\mu\text{m}$ ) slit at phase  $\phi = 0.12$ .

### 2.2.2. Silicon line

The Si I line of the multiplet 2 at 4102.94 Å appears at the same phases as the hydrogen lines, namely around maximum light, and varies in strength similarly to the Balmer lines. The variation in appearance with phase is presented in Fig. 2.7 for RR Sco, R Aql, R Car, S Scl and R Hya. For comparison additional observations taken with a narrow slit are shown in Fig. 2.8 for one phase in each of R Car and S Scl. We measured a FBW of the silicon line of around 60 km s<sup>-1</sup> when the line first appears, somewhat less than the FBW of the Balmer lines. Like the Balmer emission lines, the Si I emission line can be seen at the remarkably early phase  $\phi=0.58$  in RR Sco (Fig. 2.7, left panel).

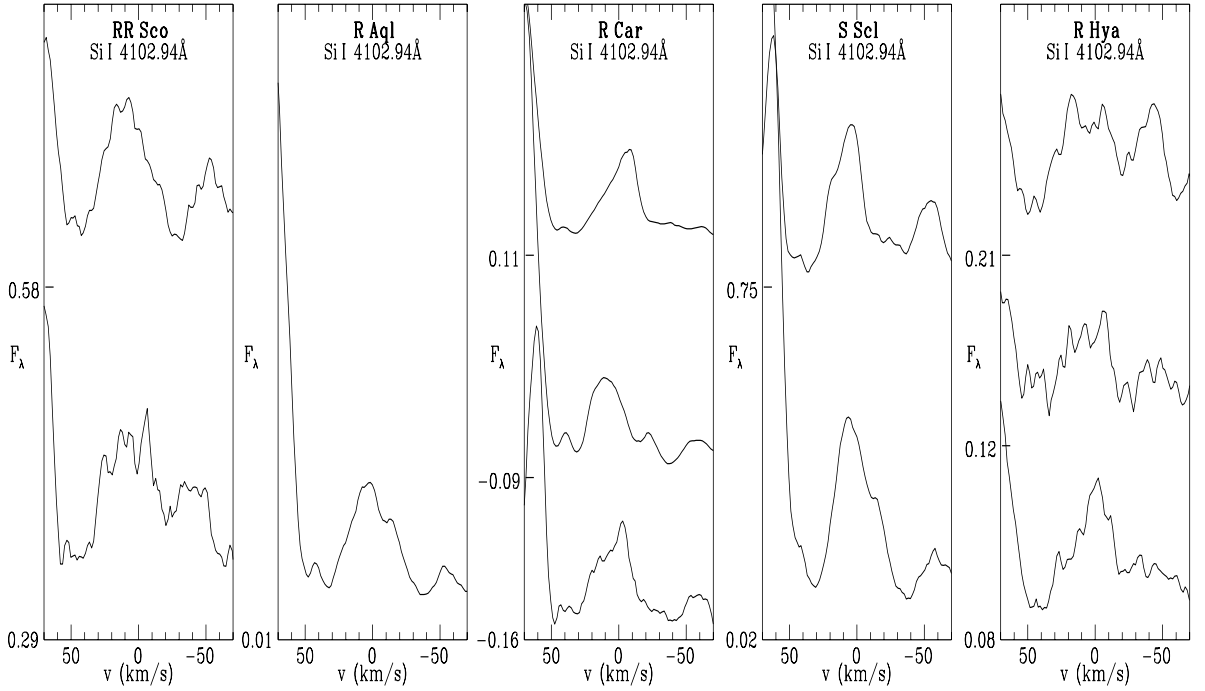


Figure 2.7.: *From left to right:* Line profiles of Si I 4102.94 Å (M 2) as a function of phase in RR Sco, R Aql, R Car, S Scl and R Hya (plotted as in the left panel of Fig. 2.2). The feature on the left of each plot is the edge of the nearby H $\delta$  emission line. Table A.2 lists the maximum flux level in each Si I line.

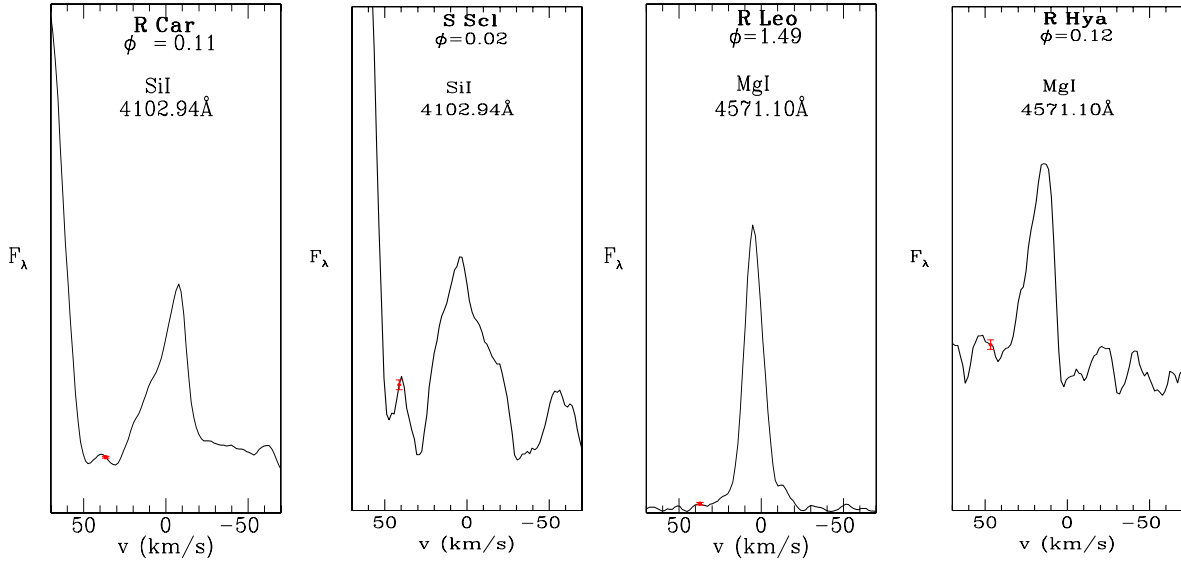


Figure 2.8.: *From left to right:* Narrow ( $300\,\mu\text{m}$ ) slit spectra for the Si I  $4102.94\,\text{\AA}$  line at phase  $\phi = 0.11$  in R Car and  $\phi = 0.02$  in S Scl, and the Mg I  $4571.10\,\text{\AA}$  line at phase  $\phi = 1.49$  in R Leo and  $\phi = 0.12$  in R Hya. These plots are shown for comparison with the wide ( $1500\,\mu\text{m}$ ) slit observations in Fig. 2.7 and Fig. 2.9.

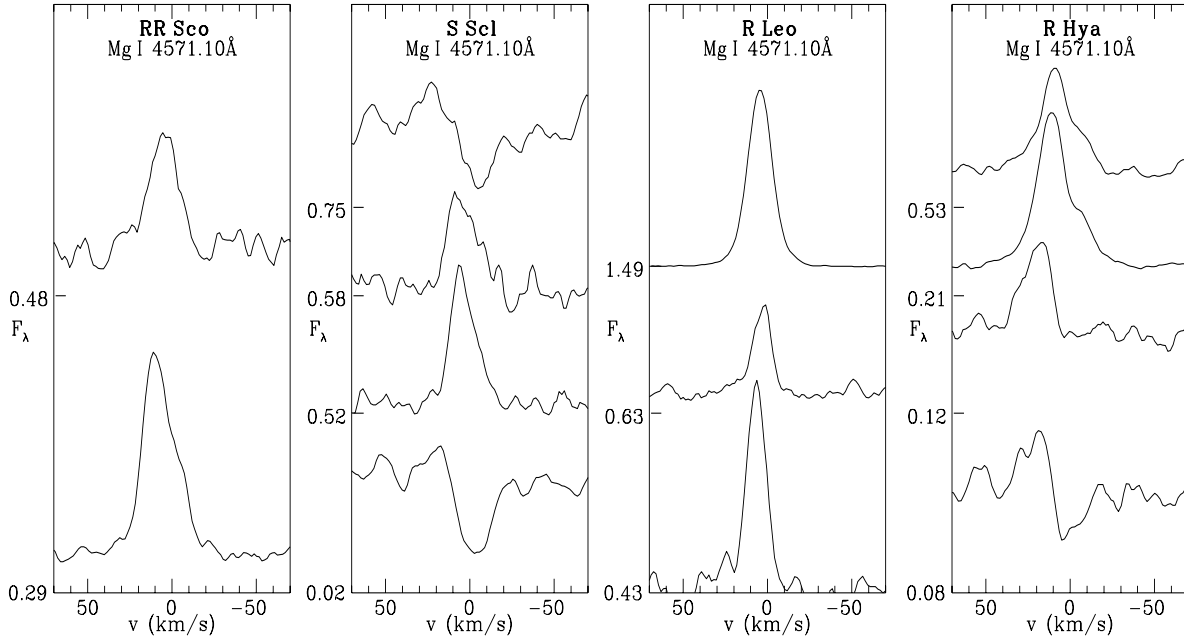


Figure 2.9.: *From left to right:* Line profiles of Mg I  $4571.10\,\text{\AA}$  (M 1) as a function of phase in RR Sco, S Scl, R Leo and R Hya (plotted as in the left panel of Fig. 2.2). Table A.1 in Sect. 2.3 lists the maximum flux level in each line.

### 2.2.3. Magnesium lines

All observed Mg I emission lines (M 1: 4571.10 Å; M 3: 3829.32 Å, 3832.35 Å and 3838.29 Å) are presented in Figs. 2.9–2.11. Additional narrow slit observations are shown in the same figures for the multiplet 3 lines, and in Fig. 2.8 for the 4571.10 Å line.

The lines of the Mg I multiplet 3 at 3829.32 Å, 3832.35 Å and 3838.29 Å appear around the phase of maximum when the hydrogen lines are also dominant. These lines are high excitation lines (lower state excitation potential 2.7 eV) and the Einstein-coefficient is rather large (see Table 2.3). The emission lines were detected in R Aql and R Car (Figs. 2.10 and 2.11) where the early post-maximum phases was observed in detail. The FBW is  $\sim 30\text{--}40\text{ km s}^{-1}$  and these lines are always blueshifted. For phase  $\phi=0.01$  in R Aql (Fig. 2.10) the emission lines show equal velocity shifts of  $\sim +10\text{ km s}^{-1}$ , as it can also be seen in the panel of the narrow slit observation in Fig. 2.10 (all emission line velocities quoted in this work are measured at half maximum height). For R Car (Fig. 2.11), the velocity shift of the lines at 3829.32 Å and 3832.35 Å is about  $+20\text{ km s}^{-1}$  when they first appear ( $\phi=-0.09$ ): the weak 3838.29 Å line appears to be strongly affected by overlying absorption causing it to show a smaller velocity shift of only  $\sim +10\text{ km s}^{-1}$ . At phase  $\phi=0.11$ , all multiplet 3 lines are equally blueshifted by  $\sim +10\text{ km s}^{-1}$ .

At later phases, the lines of the multiplet 3 disappear and the Mg I 4571.10 Å (M 1) emission line appears. The lower level of this emission line is the ground state and the Einstein-coefficient is rather low (see Table 2.3). As a ground state line, it is prominent in absorption as well as emission. Before and around maximum light, two absorption components appear, especially in R Car (Fig. 2.11,  $\phi=-0.16\text{--}0.11$ ), which presumably correspond to material behind and in front of the emerging shock front. The majority of the observed Mg I 4571.10 Å emission lines are affected by obvious overlying absorption on the negative velocity side, although this absorption decreases as the phase advances.

The FBW of the Mg I 4571.10 Å emission line is generally around  $40\text{--}50\text{ km s}^{-1}$  when it first appears and it is blueshifted by  $\sim +10\text{ km s}^{-1}$  with respect to the centre-of-mass velocity. There is a general decrease in the blueshift towards minimum light; this is probably due to a combination of a real slowing of the shock and a decrease in overlying absorption on the red edge. For R Aql (Fig. 2.10), the velocity shift around the minimum phase ( $\phi=0.50$ ) seems to increase again, possibly due to some asymmetry in the upper atmosphere being transversed by the shock.

In R Leo there are two minima observed which appear rather different. Around the first minimum, the Mg I 4571 Å line was very faint and narrow ( $\text{FBW} \sim 30\text{ km s}^{-1}$ ) with the velocity shift decreasing from  $+5\text{ km s}^{-1}$  to  $+2\text{ km s}^{-1}$  for the phases  $\phi=0.43$  to  $\phi=0.63$ . At the next minimum, the emission line was bright and showed a FBW of  $\sim 40\text{ km s}^{-1}$  and the line was centred at a velocity shift of  $\sim +3\text{ km s}^{-1}$ . The AAVSO light curve shows that the light maximum preceding the first minimum was much fainter than the maximum preceding the second minimum. A bright preceding maximum obviously leads to a much wider and stronger Mg I 4571.10 Å emission line. This is consistent with the hypothesis that a stronger (visually brighter) maximum is associated with a stronger shock.



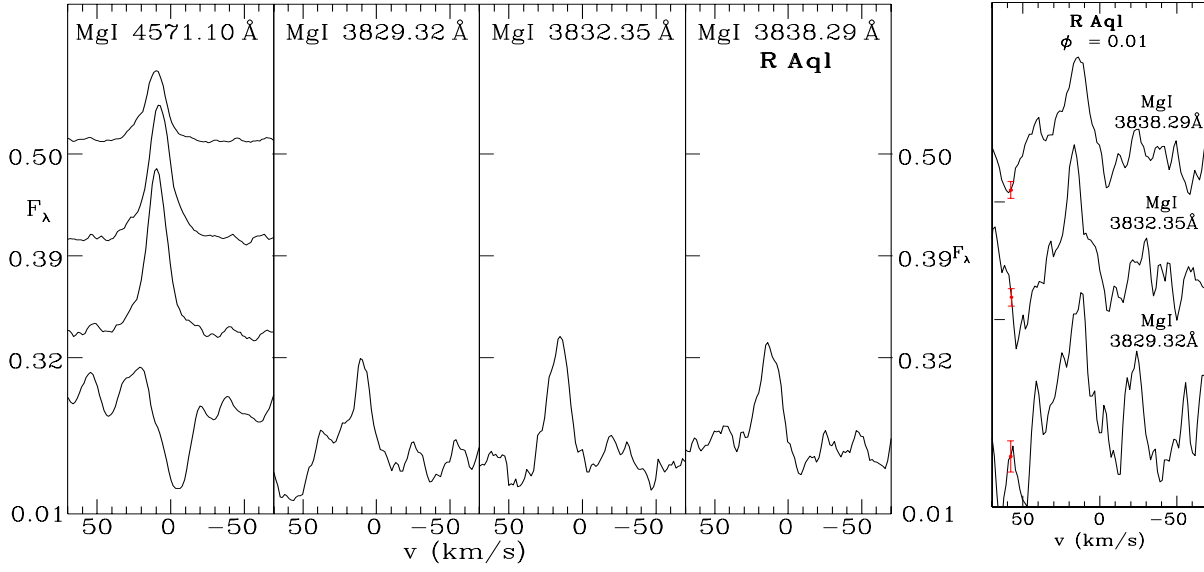


Figure 2.10.: *Left*: Line profiles of MgI 4571.10 Å (M 1) and MgI 3829.32 Å, 3832.35 Å and 3838.29 Å (all M 3) as a function of phase in R Aql (plotted as in the left panel of Fig. 2.2). Table A.1 lists the maximum flux level in each line. *Right*: Profiles of the MgI multiplet 3 lines observed with a narrow slit (300  $\mu\text{m}$ ) at a single phase, shown for comparison with the wide slit (1500  $\mu\text{m}$ ) observations.  $F_\lambda$  is plotted vertically, with the zero flux level for each spectrum being indicated by a tick mark on the vertical axis.

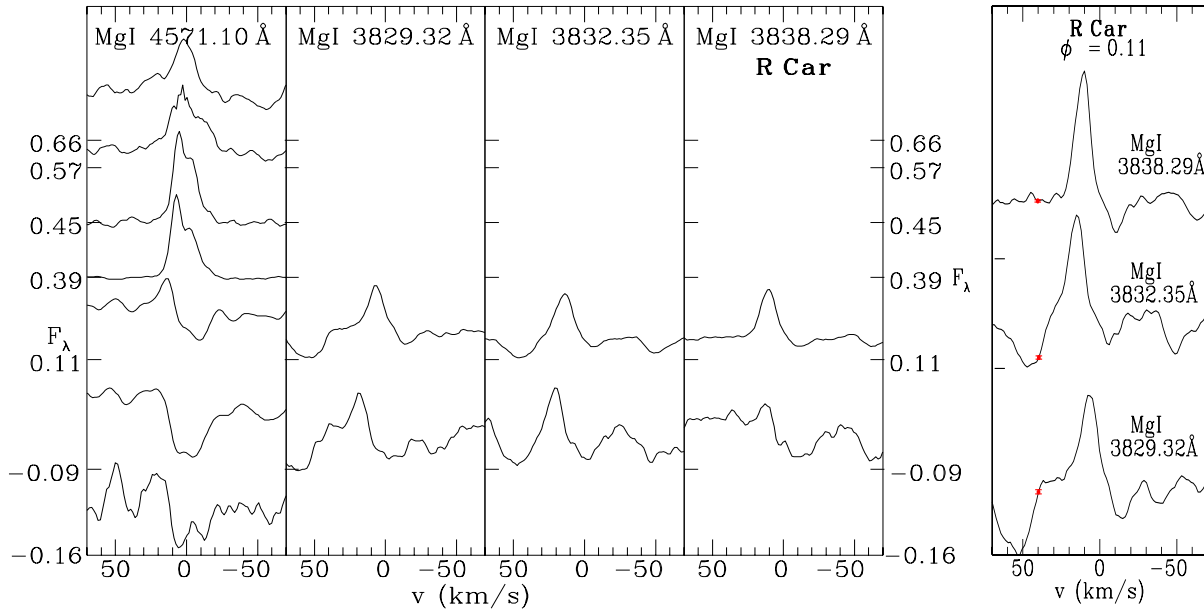


Figure 2.11.: Same as Fig. 2.10 but for R Car.

#### 2.2.4. Neutral iron lines

Out of the variety of neutral iron emission lines in Mira variables, we studied the following: (M 2) 4461.65 Å and 4375.93 Å, (M 3) 4216.18 Å, (M 42) 4307.90 Å and 4202.03 Å, (M 73) 3852.57 Å and (M 828) 4427.30 Å. Figs. 2.12–2.17 show the observed Fe I lines for all stars of our sample. For S Scl, R Hya and R Aql we present narrow slit as well as broad slit observations for some of the neutral iron lines.

It is obvious that several of the Fe I emission lines, namely Fe I 4307.90 Å, 4202.03 Å and 3852.57 Å, appear brightly during the post-maximum phase of every star of our sample. Table 2.3 shows that these are all high excitation lines (lower level excitation potential 1.5–2.2 eV) with large Einstein-coefficients. It has been suggested that the great strength of all three lines is the result of fluorescence, the lines being pumped by the Mg II 2795, 2802 Å lines (Thackeray 1937; Willson 1976).

The 3852.57 Å line appears around maximum visible light with a very narrow FBW of  $\sim 25$ – $30$  km s $^{-1}$ . At later phases it widens up to a FBW of  $\sim 40$ – $60$  km s $^{-1}$ . It appears that this is due to overlying absorption at early phases removing the negative velocity side of the line (see R Car, R Hya and R Aql in Figs. 2.13, 2.15 and 2.16).

The 4202.03 Å line also appears near maximum light (see R Car, S Scl and R Aql in Figs. 2.13, 2.14 and 2.16). At early phases, it shows an obvious inverted P-Cygni profile caused by overlying absorption of infalling material.

The 4307.90 Å line does not appear as prominently as the previous line for phases  $\leq 0.2$  even though both lines have identical upper states (see Table 2.3). This is almost certainly due to more overlying absorption affecting this line: around maximum light in R Car, S Scl and R Aql (Figs. 2.13, 2.14 and 2.16), the line is totally in absorption while the 4202.03 Å line shows distinct emission. Multiple absorption components are clearly visible cutting into the emission line except at the latest phases. This may be partly self-absorption by pre- and post-shock material as the 4307.90 Å has the largest Einstein-coefficient of the two lines. The large Einstein-coefficient may also explain the fact that the 4307.90 Å line persists the longest and has the largest flux (see Table A.4) of the two lines.

All other Fe I emission lines observed are low excitation lines (see Table 2.3). The 4375.93 Å line of the multiplet 2 appears around the phase of maximum light (see RR Sco, R Car and R Leo in Figs. 2.12, 2.13, 2.17), which is an exceptional early appearance for a low excitation line. The line shows an obvious inverted P Cygni profile with a steep red wing: the absorption component decreases towards later phases. The 4461.65 Å line was only detected in emission in R Car at the phase  $\phi=0.39$  and in R Leo at  $\phi=1.49$  (Figs. 2.13 and 2.17). Although it belongs to the same multiplet (2) as the 4375.93 Å line, it is not as prominent at early phases as the latter.

The remainder of the observed Fe I low excitation lines only appear in some stars and no regularity can be seen. The Fe I 4427 Å emission line was observed in RR Sco and R Leo at just one phase each (see Figs. 2.12 and 2.17). Finally, the low excitation line at 4216.18 Å was observed in R Leo at the phase  $\phi=1.49$ .

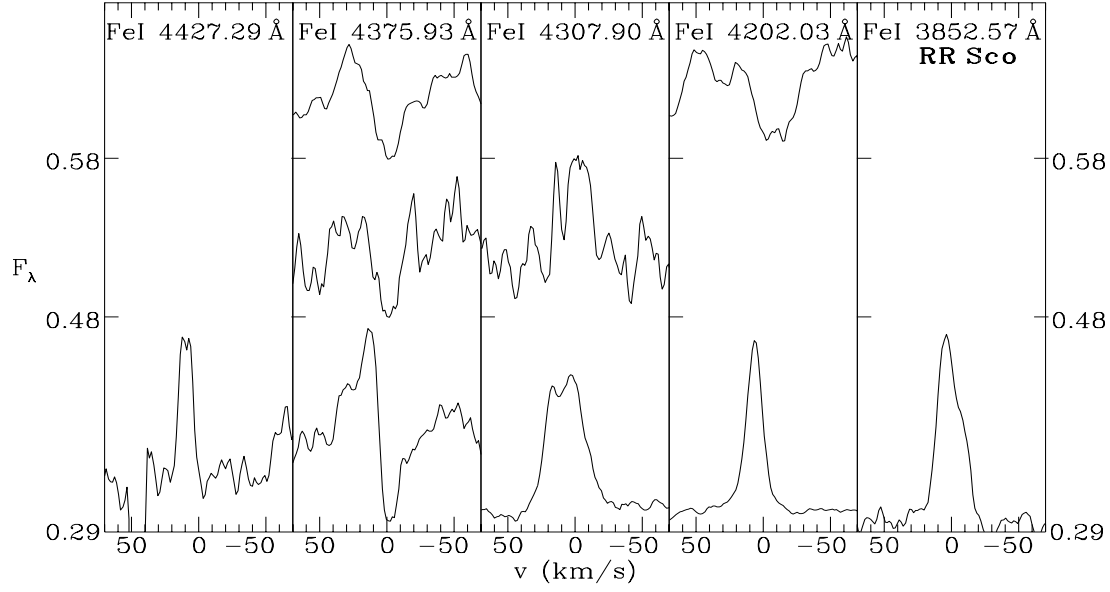


Figure 2.12.: Line profiles of FeI 4427.30 Å (M 828), 4375.93 Å (M 2), 4307.90 Å, 4202.03 Å (both M 42) and 3852.57 Å (M 73) as a function of phase in RR Sco (plotted as in the left panel of Fig. 2.2). Tables A.4 and A.5 in Sect. 2.3 list the maximum flux level in each line.

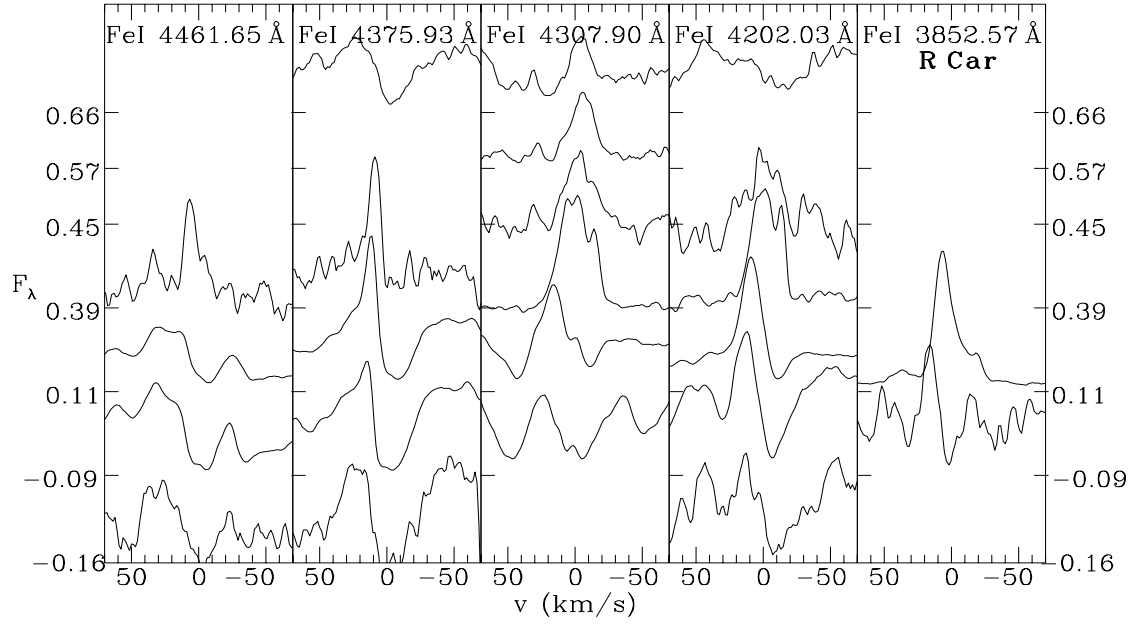


Figure 2.13.: Same as Fig. 2.12 but for R Car, and with FeI 4461.65 Å (M 2) replacing FeI 4427.30 Å (M 828) in the left panel.

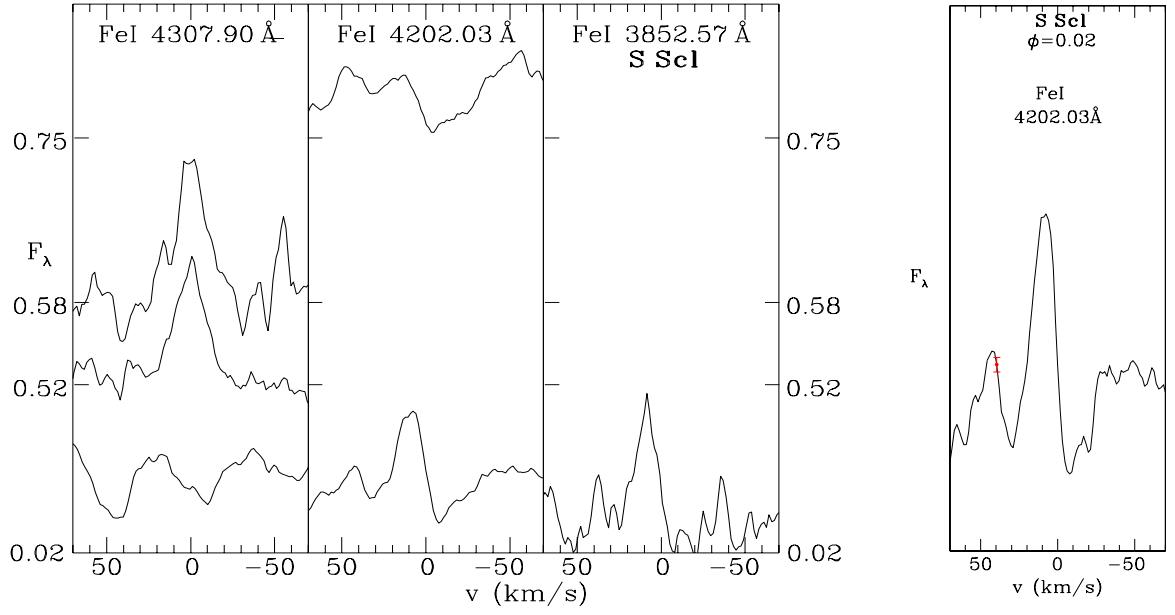


Figure 2.14.: *Left*: Line profiles of FeI 4307.90 Å, 4202.03 Å (both M 42) and 3852.57 Å (M 73) as a function of phase in S Scl (plotted as in the left panel of Fig. 2.2). Tables A.4 and A.5 list the maximum flux level in each line. *Right*: The FeI 4202.03 Å line profile observed with a narrow (300  $\mu\text{m}$ ) slit at phase  $\phi = 0.02$ , shown for comparison with the wide slit (1500  $\mu\text{m}$ ) observations.

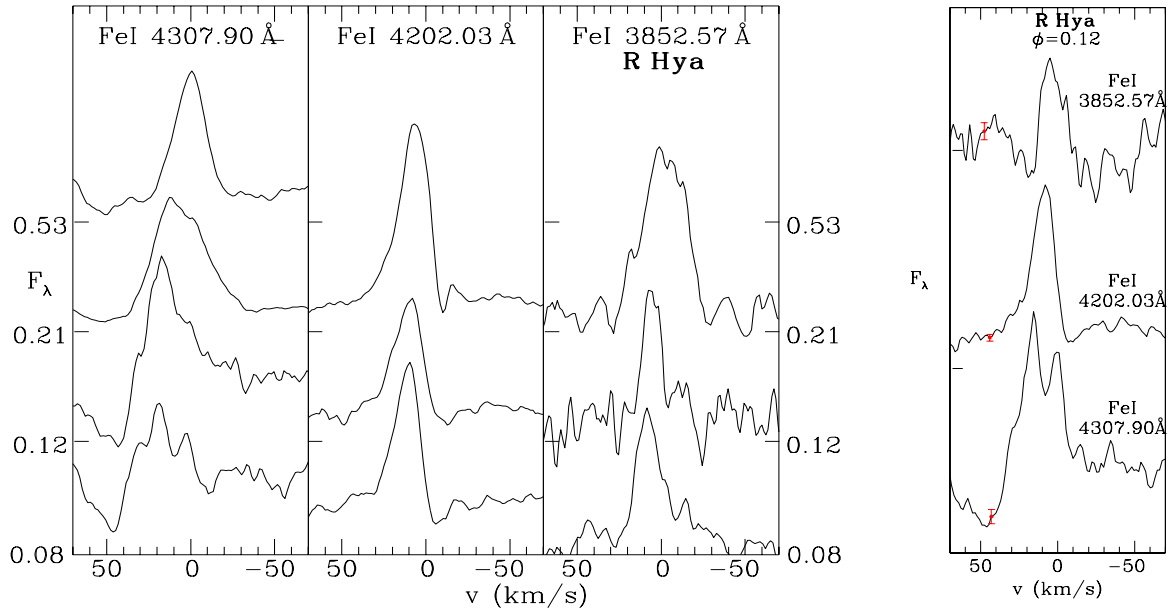


Figure 2.15.: *Left*: Same as Fig. 2.14 but for R Hya, and including FeI 4307.90 Å (M 42) and 3852.57 Å (M 73) in the right panel.

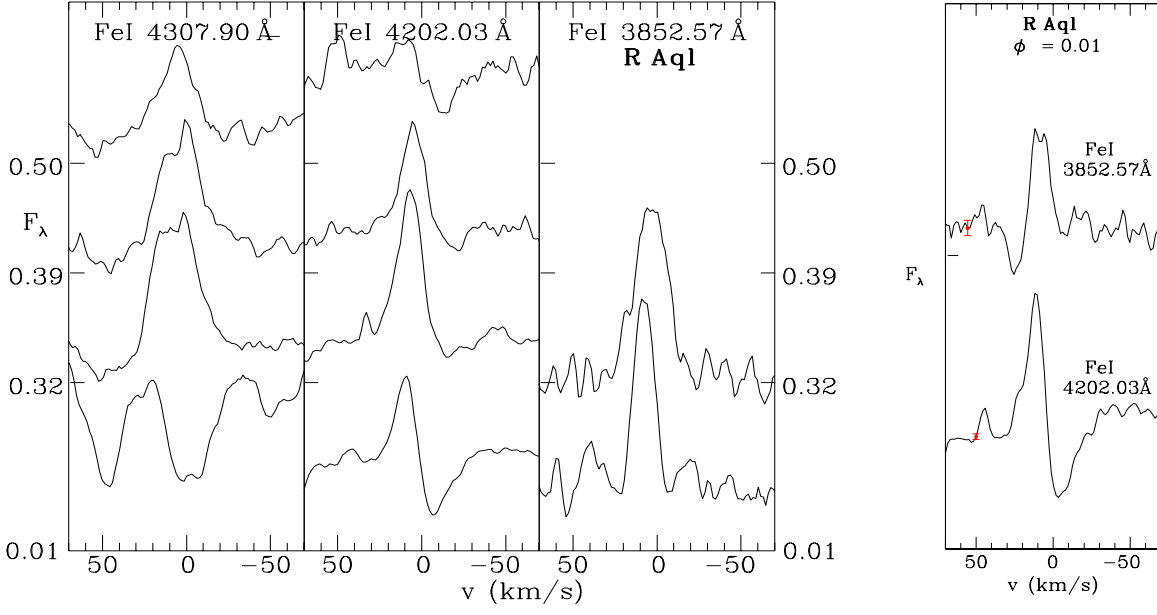


Figure 2.16.: *Left*: Same as Fig. 2.14 but for R Aql, and including FeI 3852.57 Å (M 73) in the right panel.

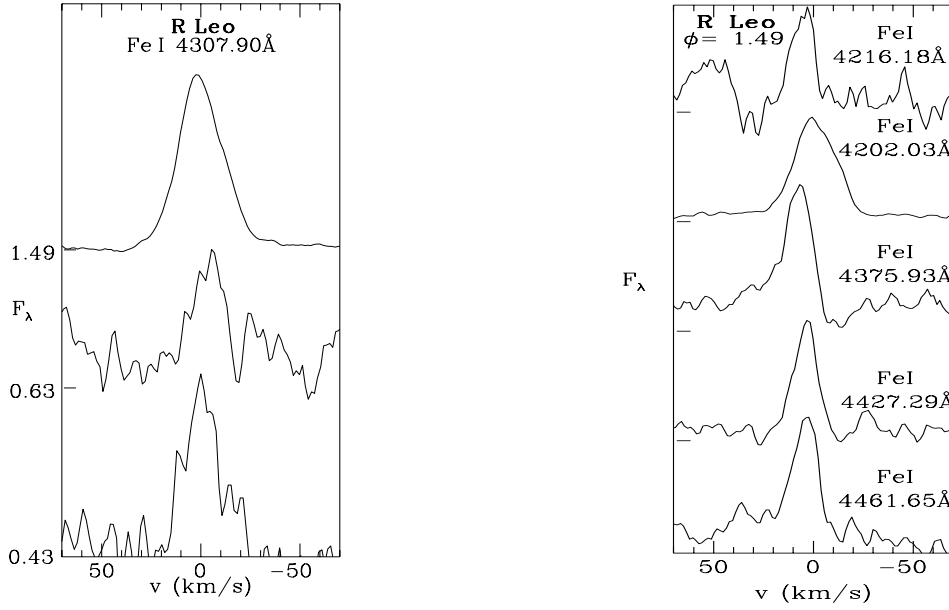


Figure 2.17.: *Left*: Line profiles of FeI 4307.90 Å (M 42) as a function of phase in R Leo. *Right*: Line profiles of FeI 4461.65 Å, 4375.93 Å (both M 2), 4427.30 Å (M 828), 4202.03 Å (M 42) and 4216.18 Å (M 3) at phase  $\phi=1.49$  in R Leo. Both panels are plotted as in the left panel of Fig. 2.2. Tables A.4 and A.5 list the maximum flux level in each line.

### 2.2.5. Ionised iron lines

To recall: the emission lines of ionised iron are the centre of the investigations in this thesis, because they are presumably good candidates to be developed as a diagnostic tool for the dust-forming zones of M-type Mira variables. They have only been observed in a few stars of the M-type Mira sample.

The permitted Fe II 4583.84 Å emission line was observed in three of the stars of our sample, namely RR Sco, R Car and R Leo (Figs. 2.18 and 2.19). This is a high excitation line (lower level excitation potential 2.8 eV) which appears towards the minimum light of the star, at phase  $\phi=0.29$  in RR Sco,  $\phi=0.39$  in R Car and  $\phi=1.49$  in R Leo. The FBW varies from  $\sim 35 \text{ km s}^{-1}$  in RR Sco and R Car to  $\sim 45 \text{ km s}^{-1}$  in R Leo. The velocity shifts of the Fe II line are around  $+2 \text{ km s}^{-1}$  in these stars.

In R Leo and R Car, forbidden [Fe II] lines can be clearly seen at the same phase as the permitted Fe II line at 4583.84 Å (Figs. 2.18 and 2.19). In R Leo at phase  $\phi=1.49$ , following the bright maximum, we found the transitions [Fe II] 6F (4457.95 Å), [Fe II] 21F (4276.83 Å and 4243.97 Å) and [Fe II] 7F (4359.33 Å and 4287.39 Å). No forbidden lines could be seen in the previous cycle following a fainter maximum.

In R Car at phase  $\phi=0.39$ , we identified only the two [Fe II] 7F emission lines at 4359.33 Å and 4287.39 Å. Unfortunately, the observation for R Car at phase  $\phi=0.39$  was taken with a narrow slit in poor weather conditions, so the signal to noise of these faint lines is low. Other forbidden lines were probably present but undetectable. In RR Sco we could not identify any of the forbidden lines, although we could clearly detect the permitted Fe II line (Figs. 2.18).

The FBW of the [Fe II] 7F emission lines in R Car is  $\sim 21 - 26 \text{ km s}^{-1}$ . The velocity shift was measured at  $0-2 \text{ km s}^{-1}$ , which is the same as for the permitted Fe II 4583.84 Å emission. In R Leo, all the [Fe II] emission lines have a FBW of  $\sim 40 \text{ km s}^{-1}$ . The velocity shifts are approximately  $0-2 \text{ km s}^{-1}$  for the 7F and the 21F emission lines, similar to the velocity shift of permitted Fe II 4583.84 Å line.

Evidence has been presented in the previous sections that R Car and R Leo show particular strong shocks in the cycles where Fe II and [Fe II] emission lines appear. In R Leo, the second minimum observed showed much stronger metal emission lines than the first, and the second minimum followed a brighter maximum than the first. Forbidden [Fe II] lines were only observed during the second minimum of R Leo. Also R Car was observed after a relatively bright maximum. This suggests that the erratic appearance of these emission lines may be because they require an exceptionally bright maximum for production, which is presumably connected to stronger-than-normal shocks.

### 2.2.6. Manganese line

The manganese line at 4030.75 Å was observed in only one star, namely R Leo, at phase  $\phi=1.49$  (Fig. 2.19). The peak flux is  $F_{\text{peak}} = 8.8 \cdot 10^{-13} \text{ erg cm}^{-2} \text{ s}^{-1} \text{ Å}^{-1}$  and the total flux  $F_{\text{tot}} = 2.6 \cdot 10^{-13} \text{ erg cm}^{-2} \text{ s}^{-1}$ . The Mn I emission line shows a FBW of  $\sim 28 \text{ km s}^{-1}$  and has a large velocity shift of  $10 \text{ km s}^{-1}$ , unlike the Fe II and [Fe II] lines at the same phase. As with the neutral Fe lines of low excitation (e.g. Fe I 4375.93 Å), the sharper red edge of the line indicates absorption by infalling, neutral Mn atoms in the layers above the shock.

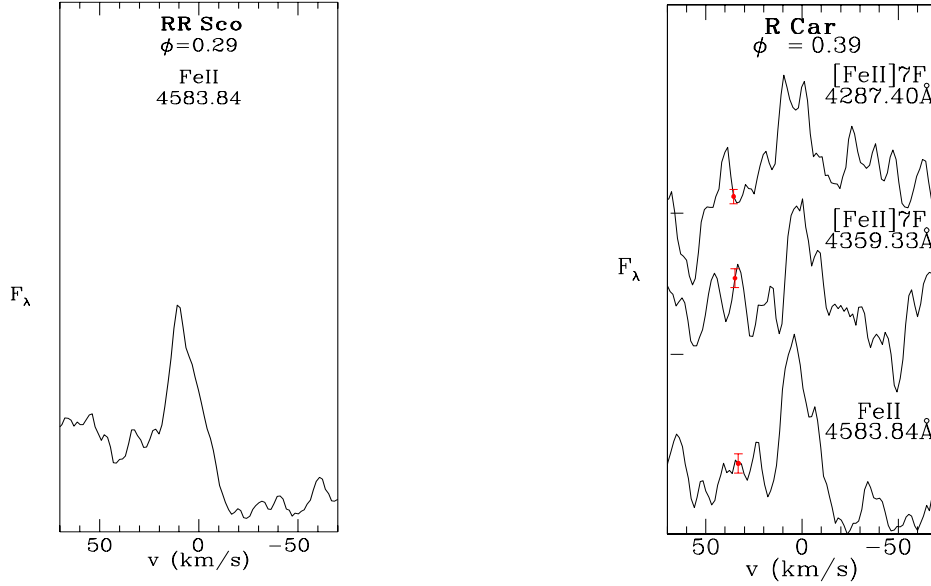


Figure 2.18.: *Left*: Line profile of FeII 4583.84 Å (M 38) at phase  $\phi=0.29$  in RR Sco (1500  $\mu\text{m}$ ). Table A.3 lists the maximum flux level in the line. *Right*: Line profiles of FeII 4583.84 Å (M 38) and of the forbidden transitions [FeII] 7F (4359.33 Å and 4287.40 Å) at phase  $\phi=0.39$  in R Car.  $F_\lambda$  is plotted vertically, with the zero flux level for each spectrum being indicated by a tick mark on the vertical axis. Table A.3 lists the maximum flux level in each line.

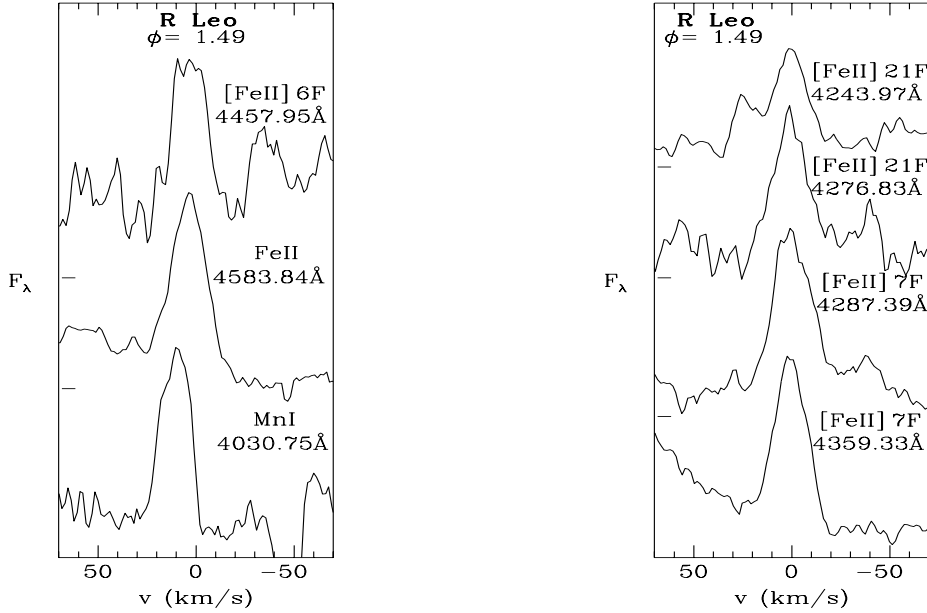


Figure 2.19.: *Left*: Line profiles of MnI 4030.75 Å (M 2), FeII 4583.84 Å (M 38) and [FeII] 6F 4457.95 Å at phase  $\phi=1.49$  in R Leo.  $F_\lambda$  is plotted vertically, with the zero flux level for each spectrum being indicated by a tick mark on the vertical axis. Table A.3 lists the maximum flux level in each line (flux for MnI see Sec. 2.2.6). *Right*: Line profiles of the forbidden transitions [FeII] 7F (4359.33 Å and 4287.40 Å) and [FeII] 21F (4276.83 Å and 4243.97 Å) at phase  $\phi=1.49$  in R Leo. Table A.3 lists the maximum flux level in each line.

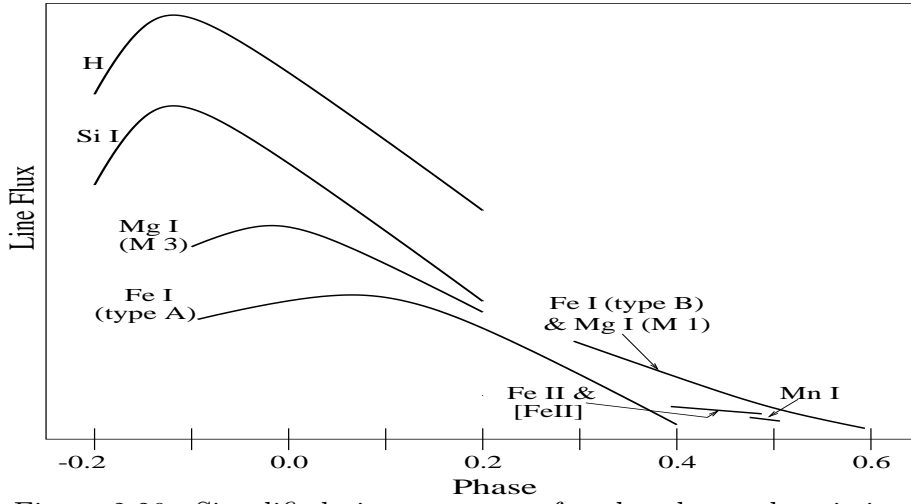


Figure 2.20.: Simplified time sequence for the observed emission lines and their total fluxes (in arbitrary units).

### 2.3. Phase-dependent variation of line fluxes

To summarise the observed line fluxes a simplified time sequence of the total fluxes is depicted in Fig. 2.20. This scheme already clarifies that the potential diagnostic tool — the emission lines Fe II and [Fe II] — are among the metal lines which appear late around minimum light. They are especially outstanding because they are the only *ionised* metal lines in this phase. Also one can note that these lines belong to the faintest lines observed. To get the complete picture of the emission line fluxes in M-type Miras and to analyse the conditions which lead to the emission of the Fe II and [Fe II] emission lines in some stars but not in others, this section presents the time sequences of all the measured fluxes in stars of the M-type Mira sample (Figs. 2.21–2.24). For further analyses additional Balmer line fluxes by Fox et al. (1984) for the M-type Miras S Scl, RR Scl, R Aql and R Car are plotted in the according figures.

- **Balmer line fluxes:** The typical variation with phase of the Balmer line fluxes can be seen best in R Car (Fig. 2.24) due to the dense observational coverage of this star. The Balmer lines  $H\gamma$  and  $H\delta$  appear first, roughly between phases -0.4 and -0.2, as it can also be seen in Figs. 2.21 and 2.23 in S Scl, RR Scl and R Aql. The lines then strengthen rapidly, reaching maximum flux around phase -0.1. At this phase, the other Balmer lines are observed as well, which reach maximum flux around phase +0.1 when the overlying absorption is reduced. The Balmer lines finally vanish about phase  $\phi=0.4$ .

Fox et al. (1984) noted that the Balmer line fluxes can vary enormously from cycle to cycle (see *o Ceti* in their data), where brighter maxima yield brighter Balmer lines. A comparison of their fluxes to our data for R Car also shows this effect (Fig. 2.24, right panel): the Balmer lines observed in R Car are roughly ten times brighter than the lines observed by Fox et al. At the same time, the AAVSO light curves show that the visual maximum during our observations ( $V \sim 3.8$ ) was about one magnitude brighter than the maximum ( $V \sim 4.8$ ) during which Fox et al. made their observations.

- **Silicon line fluxes:** The Si I 4102 Å (M2) high excitation line appears in all stars near maximum light (R Hya, S Scl, RR Scl, R Aql, R Car see Figs. 2.21–2.24). The line flux is always less than in the nearby Balmer line  $H\delta$ . In general, the variation with



phase and the phase of the peak flux is similar to that of the hydrogen lines, although the peak flux is a factor of  $\sim 10$  less than in the hydrogen lines.

- **Magnesium line fluxes:** The high excitation lines of the multiplet 3 of Mg I (3829.32 Å, 3832.35 Å and 3838.29 Å) appear near maximum light and were observed in R Aql and R Car (Fig. 2.23 right panel, and Fig. 2.24 left panel). The flux in these lines is about a factor of 30 less than in the Balmer lines. The lines disappear at phase  $\phi \sim 0.2$ – $0.3$  when they are replaced by the low excitation line of Mg I (M 1) at 4571.10 Å. The latter was observed in every star of our sample, and is observable up to the late phase of  $\phi \sim 0.6$ . It appears exceptionally early ( $\phi=0.12$ ) in R Hya.

- **Neutral iron line fluxes:** The Fe I lines show a rather complex variation with phase as already shown in Sec. 2.2.4. In general, one can divide them into two groups: type A, those which appear early in the cycle ( $\sim$  maximum); and type B, those which appear around  $\phi \sim 0.3$  –  $0.4$ . The first group consists of 4202.03 Å (M 42), 3852.57 Å (M 73) (both high excitation lines) and the 4375.93 Å (M 2) (a low excitation line). Variation of flux with phase in R Hya, R Aql and R Car can be seen in Fig. 2.21 right panel, Fig. 2.23 right panel, and Fig. 2.24 left panel. These lines vary less rapidly than the Balmer or Si I lines and reach their maximum at the later phase of  $\phi \sim 0.1$ .

The type B Fe I emission lines 4427.29 Å (M 828), 4461.65 Å (M 2), 4216.18 Å (M 3) and 4307.90 Å (M 42) appear around  $\phi \sim 0.3$ – $0.4$  and are usually fainter than Fe I emission lines discussed above. Apart from the 4307.90 Å line, these emission lines are all of low excitation. As noted in Sec. 2.2.4, the 4307.90 Å line has the same upper level as the 4202.03 Å line of the same multiplet and its late appearance and low flux relative to the latter line is almost certainly due to overlying absorption. However, the flux in the 4307.90 Å line at late phases is usually greater than in other late emission lines of Fe I 4427.29 Å, 4461.65 Å and 4216.18 Å. Its flux and variation with phase is quite similar to the Mg I 4571.10 Å line.

- **Ionised iron line fluxes:** Fe II lines were observed at late phases in a number of stars. Line fluxes of the permitted Fe II 4583.84 Å (M 38) emission line are shown for RR Sco, R Car and R Leo in Figs. 2.23, 2.24 and 2.21 (left panels). This high excitation line appears around  $\phi \sim 0.3$ – $0.5$ . Fluxes for the forbidden lines [Fe II] 7F at 4359.33 Å and 4287.40 Å are plotted in Fig. 2.24 (left panel) for R Car at phase  $\phi=0.39$  and in Fig. 2.21 (left panel) for R Leo at  $\phi=1.49$ . The line flux in R Car is similar to that of the permitted Fe II emission line at 4583.84 Å. In R Leo, however, the forbidden line flux is  $\sim 3$  times higher than the permitted line flux, at least for  $\phi=1.49$  where the forbidden lines were observed. At phase  $\phi=1.49$  in R Leo, we also measured the line fluxes of the [Fe II] 6F and [Fe II] 21F emission lines. These lines are weaker than the [Fe II] 7F lines: their flux is comparable to the faint, late-appearing Fe I lines.

The analyses of the total fluxes seems to confirm the suggestion noted in Sec. 2.2: Forbidden lines only appear in stars which are perturbed by stronger-than-normal shocks. In R Car the comparison to the Fox et al. data showed that the Balmer line flux is much stronger in our observations, which is an indication for a stronger shock emerging from the photosphere. In R Leo one can note the much higher metal emission line fluxes during the second observed minimum, e.g. Mg I 4571.10 Å stronger by a factor of  $\sim 3$  and Fe I 4307.90 Å stronger by a factor of almost 10, which also indicates a stronger shock.

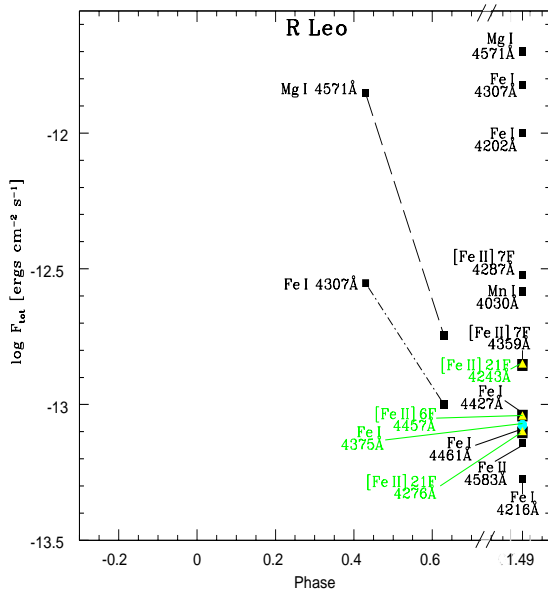


Figure 2.21.: *Left:* Absolute line fluxes plotted against phase in R Leo. Note the change in scale of the phase for we plotted the fluxes of the minimum of the next cycle in the same panel. Note also that several line fluxes are coincident at phase  $\phi=1.49$  ([Fe II] 7F 4359 Å and [Fe II] 21F 4243 Å; Fe I 4427 Å and [Fe II] 6F 4457 Å; Fe I 4461 Å, Fe I 4375 Å and [Fe II] 21F 4276 Å). *Right:* Absolute line fluxes plotted against phase in R Hya. Note the coincident line fluxes at phases  $\phi=0.08$  (Si I and Fe I 3852 Å) as well as  $\phi=0.12$  (Si I and Fe I 4202 Å).

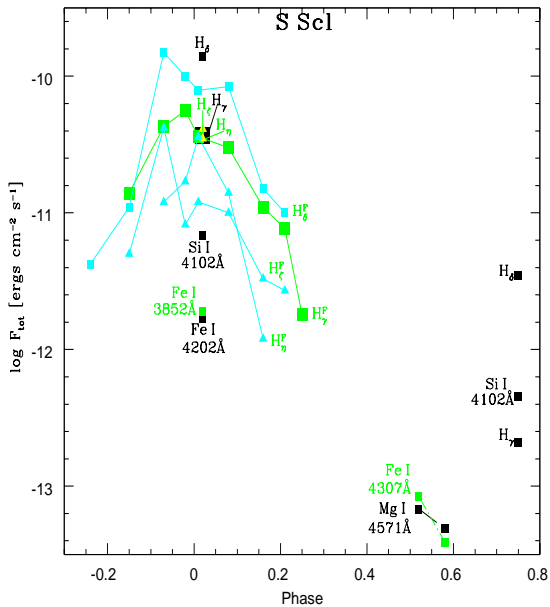


Figure 2.22.: Absolute line fluxes plotted against phase in S Scl. Note the nearly equal fluxes for  $H_\zeta$ ,  $H_\gamma$  and  $H_\eta$  at phase  $\phi=0.02$ . At phase  $\phi=0.75$  the fluxes of newly appearing emission lines are shown. The Balmer line fluxes  $H_\gamma^F$ ,  $H_\delta^F$ ,  $H_\zeta^F$  and  $H_\eta^F$  from Fox et al. (1984) are plotted in grey. At  $\phi=-0.07$   $H_\gamma^F$  and  $H_\zeta^F$  are coincident while  $H_\gamma^F$  and  $H_\eta^F$  are equal at  $\phi=0.0$  and also nearly coincide with  $H_\eta$ .

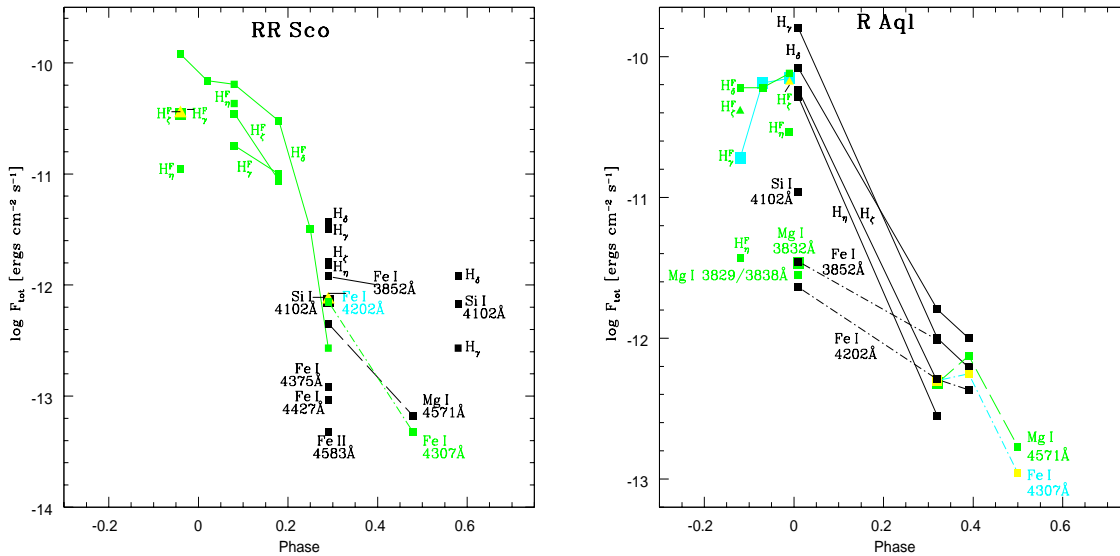


Figure 2.23.: *Left*: Absolute line fluxes plotted against phase in RR Sco. Note the nearly equal fluxes of Si I 4102 Å, Fe I 4202 Å and Fe I 4307 Å at  $\phi=0.29$ . At  $\phi=0.58$  newly appearing emission line fluxes are shown. Fox et al. (1984) fluxes are plotted in grey and marked with <sup>F</sup> (fluxes for H<sub>γ</sub><sup>F</sup> and H<sub>ζ</sub><sup>F</sup> are coincident at  $\phi=-0.04$ ). *Right*: Absolute line fluxes plotted against phase in R Aql. Note coinciding points at  $\phi=0.01$  (Mg I 3832 Å and Fe I 3852 Å) and  $\phi=0.32$  (H<sub>ζ</sub>, Fe I 4307 Å and Mg I Å). Fox et al. fluxes are plotted in grey (fluxes for H<sub>γ</sub><sup>F</sup>, H<sub>δ</sub><sup>F</sup>, H<sub>ζ</sub><sup>F</sup> are nearly equal at  $\phi=-0.01$ ).

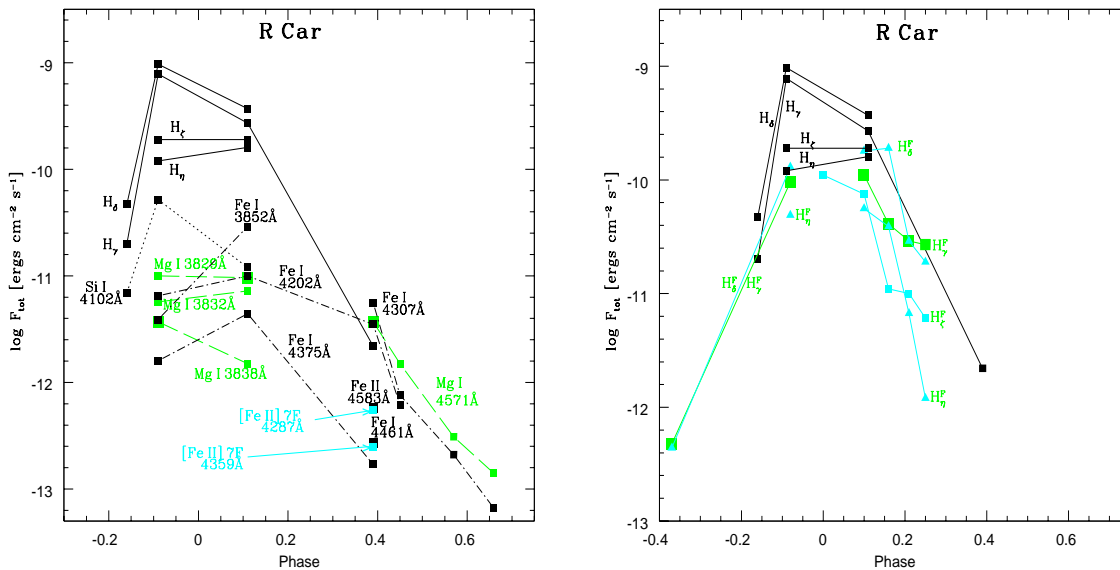


Figure 2.24.: *Left:* Absolute line fluxes plotted against phase in R Car. Note coincident points for the phases  $\phi=-0.09$  (Mg I 3838 Å and Fe I 3852 Å),  $\phi=0.11$  (Mg I 3829 Å and Fe I 4202 Å) and  $\phi=0.39$  (Fe I 4202 Å and Mg I 4571 Å; Fe II 4583 Å and [Fe II] 7F 4287 Å; Fe I 4461 Å and [Fe II] 7F 4359 Å. *Right:* Balmer line fluxes compared to Fox et al. (1984), plotted in grey and marked with <sup>F</sup> (coincident fluxes:  $\phi=-0.37$  H<sub>γ</sub><sup>F</sup> and H<sub>δ</sub><sup>F</sup>,  $\phi=0.16$  H<sub>γ</sub><sup>F</sup> and H<sub>η</sub><sup>F</sup> and  $\phi=0.21$  H<sub>γ</sub><sup>F</sup> and H<sub>δ</sub><sup>F</sup>).

## 2.4. Phase-dependent variation of line velocities

The line velocity of the emission line spectra should represent the velocity of the emission region associated with the shock wave passing through the Mira atmosphere. Actually there are two velocities superimposed in the atmosphere, namely the underlying velocity field (e.g. stellar wind) and the shock velocity. Nevertheless, if one chooses different emission lines which appear at different phases of the pulsation cycle, it is possible to determine the general trend of the shock velocity while the shock is passing through the atmosphere of the star.

In Fig. 2.25, the velocity (relative the stellar centre-of-mass) of representative emission lines is plotted against the phase of the pulsation cycle. The velocities are defined at half-height of the line profiles and are obtained from all stars in the sample. When overlying absorption is dominant (for example, at early phases of the  $H\delta$  line), no velocity measurement was made. The plot clearly shows that when the shock emerges from deep in the photosphere, the post-shock emission region has a measured outward velocity of  $\sim 10\text{--}12\text{ km s}^{-1}$ . This result is in good agreement with the velocity measured in the infrared (Hinkle 1978; Hinkle et al. 1982, 1984) for deep pulsating layers when converted to centre-of-mass velocities (Wood 1987). As phase advances, the emission line velocity decreases until it becomes essentially zero around minimum light. Note that the material whose velocity is measured by the emission lines is associated with the near-shock zone: this is quite different from the deeper, infall zone whose velocity is measured near minimum light by the infrared spectra.

At first sight, it is surprising that in the average Mira the apparent velocity of the emission lines approaches zero half a cycle after the shock emerges from the deep photosphere. Because the lines are still in emission, the shock must still be propagating outward so the post-shock material, from which the line emission presumably originates, should show a positive outward velocity. Even if the pulsation in the outer layers would be quite irregular (e.g. Bessell et al. 1996) and the shock is stalled or even reversed by infalling material from a previous cycle on average shocks must progress outward. By the time of minimum light, the shock is far above the photosphere (defined to be at optical depth one). For example, in a typical fundamental mode Mira model (e.g. see the models of Bessell et al. 1996 or Hofmann et al. 1998), the photosphere is at  $\sim 240 R_{\odot}$  while the shock is at  $\sim 420 R_{\odot}$ . In a simple geometric model for emission from such a system, neglecting absorption above the photosphere, the emission lines would have square profiles going from  $+v_{\text{shock}}$  to  $-0.82 \times v_{\text{shock}}$ , where  $v_{\text{shock}}$  would be  $\sim 5\text{ km s}^{-1}$ : only the emission with the most negative velocity is hidden behind the star. We would therefore expect the line emission to be centred close to velocity zero, as observed.

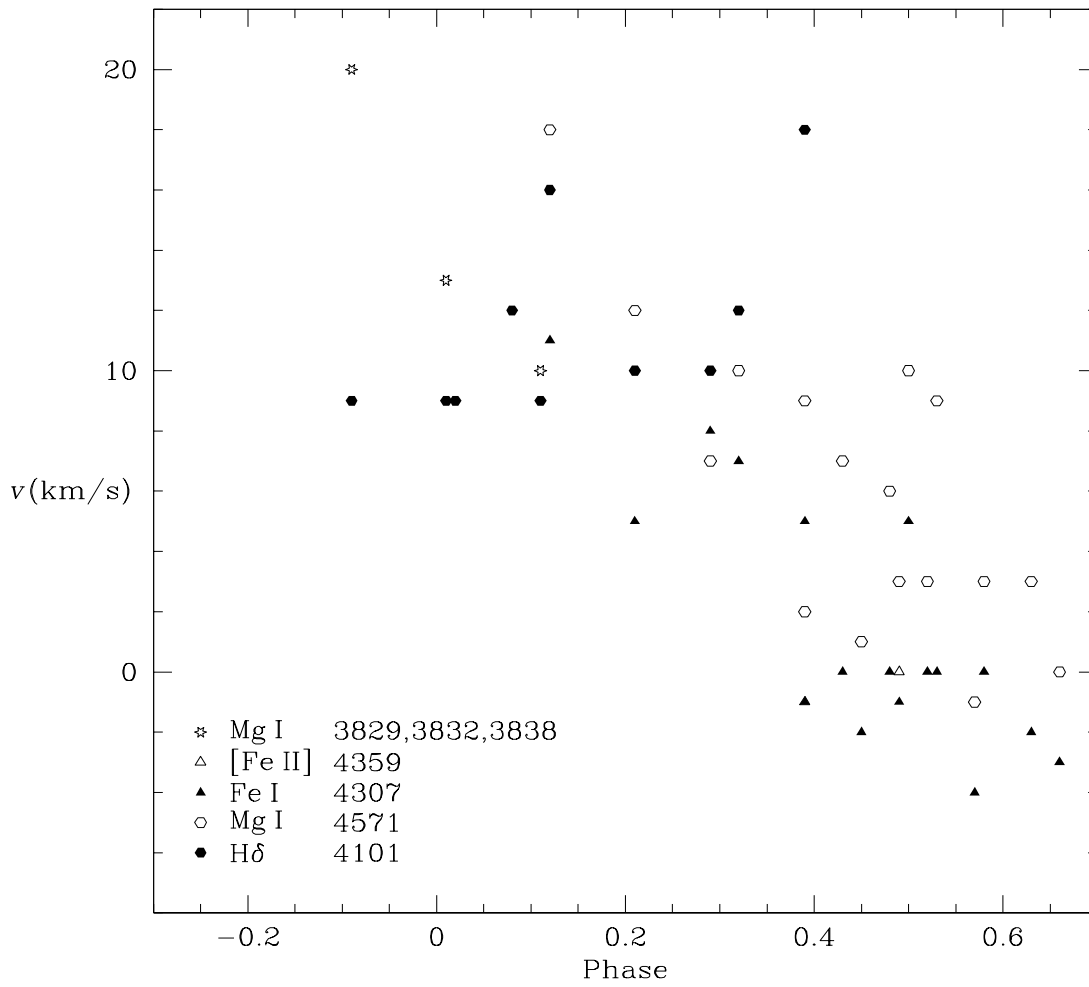


Figure 2.25.: The velocities of representative emission lines plotted against the phase of the pulsation cycle.

## 2.5. Summary & conclusions

The phase-dependent variation of emission line shapes, velocities and fluxes of observed Balmer lines and various metal emission lines obtained from the M-type Miras of our sample have been presented in order to outline the history of shock waves propagating outwards in the cool, expanding atmospheres of these variables. Apart from Balmer lines and emission lines from Si I (M 2: 4102.94 Å), Mg I (M 1: 4571.10 Å), Mg I (M 3: 3829.32 Å, 3832.35 Å and 3838.29 Å), Fe I (M 2: 4461.65 Å and 4375.93 Å), Fe I (M 3: 4216.18 Å), Fe I (M 42: 4307.90 Å and 4202.03 Å), Fe I (M 73: 3852.57 Å), Fe I (M 828: 4427.30 Å) and Mn I (M 2: 4030.75 Å) in particular the Fe II (M 38: 4583.84 Å) as well as forbidden lines [Fe II] 6F (4457.95 Å), [Fe II] 7F (4359.33 Å and 4287.39 Å) and [Fe II] 21F (4276.83 Å and 4243.97 Å) have been presented.

Concerning the permitted Fe II line and the forbidden lines [Fe II] 6F, [Fe II] 7F, and [Fe II] 21F it was investigated that they belong to the faintest emission lines observed. The emission line profiles of the lines are roughly gauss-like, respectively square-like for the forbidden lines, and are centred around zero velocity. The Fe II and [Fe II] lines were observed at late phases around minimum visible light  $\phi \sim 0.3\text{--}0.5$  in stars which have just had a bright light maximum. This suggests that their erratic appearance may be because they require an exceptionally bright maximum for production. Evidence was presented that brighter maxima are associated with stronger shock waves.

These observations have confirmed the basic idea that in particular the Fe II and [Fe II] emission lines are a good diagnostic tool to reveal the thermodynamical conditions which lead to dust formation in M-type Miras, because (i) due to the phase of their appearance they must approximately be emitted in the inner dust-forming regions and (ii) because of the erratic appearance of these lines it will be possible to give an upper boundary for the thermodynamical conditions in these zones. The observations therewith give the foundation of further theoretical studies of M-type Mira atmospheres presented in Sec. 4 in this work.

### 3. NLTE radiative line transfer

The whole spectrum of a star contains an enormous amount of information, as one could already see in the previous chapter. Radiative transfer theory provides the basis to recover this information; it is essential to understand observations of stellar atmospheres, to analyse their spectra and in particular to decrypt the information given by spectral lines.

According to the considered type of stellar object one analyses, different methods or simplifications of the otherwise very demanding radiative transfer description can be made. For example, the assumption of LTE (local thermodynamical equilibrium) will only be justified in compact atmospheres, where the collision rates will dominate over the radiation rates, e.g. in the innermost atmospheric layers. Likewise an easy planar geometry can just be assumed if an unextended atmosphere is given. Such situations clearly do *not* exist in the cool, extended, shock perturbed atmospheres of Mira variables, which makes the treatment of such atmospheres more sophisticated. One definitely needs a NLTE treatment and must handle the extreme thermodynamical changes (shocks) in those extended and moving atmospheres.

In the following the general radiative transfer theory as well as the assumptions leading to an adaption suitable for Mira variables are presented. The fundamental radiative transfer equation is motivated from the Boltzmann equation (Sec. 3.1.1) and in the following the time-independent, spherical symmetric equation in the co-moving frame (Sec. 3.1.2) is introduced. Sec. 3.1.3 then gives a brief overview on opacities followed by a specification of the used profile function in Sec. 3.1.4. Next the rate equation is characterised in Sec. 3.1.5 and the according FeII-model-atom utilised for the studies is specified in Sec. 3.1.6. In the next subsection the solution methods are described. The convenient p-z-coordinates are introduced in Sec. 3.2.1 and the Feautrier method as well as the adequate boundary and initial conditions are presented in Sec. 3.2.2. The basics of the accelerated lambda iteration method are outlined in Sec. 3.2.3. Finally, the utilised NLTE radiative transfer code `ntle-feII` is generally described and a flow chart of the calculations is given in Sec. 3.3.

## 3.1. Fundamentals of NLTE radiative transfer

### 3.1.1. Motivation of the radiative transfer equation

As a matter of fact the radiative transfer equation is nothing else than a balance equation for photons. Hence, the according equation can be derived from statistical theory via the Boltzmann equation<sup>1</sup>

$$\frac{\partial f}{\partial t} + \mathbf{v} \frac{\partial f}{\partial \mathbf{x}} + \mathbf{F} \frac{\partial f}{\partial \mathbf{p}} = \left( \frac{Df}{Dt} \right)_{col}, \quad (3.1)$$

where  $f = f(\mathbf{x}, \mathbf{p}, t)$  characterises the distribution function depending on position  $\mathbf{x}$ , momentum  $\mathbf{p}$  and time  $t$ . The equation reads as: the change with time of the distribution function plus the flux in the position space plus the flux in momentum space, as caused by external forces  $\mathbf{F}$ , equals the collision rate which lead into and out of the phase-space volume.

The energy flux of the photon field is  $I_\nu = c h \nu f$ , where  $I_\nu \equiv I_\nu(\mathbf{x}, \mathbf{n}, t)$  is the intensity in the frequency interval  $(\nu, \nu + d\nu)$ ,  $E = h\nu$  is the energy of the photons and  $c$  the speed of light. Consequently, the distribution function for photons is given by  $f = I_\nu / (c h \nu)$ . The velocity in the second term in Eq. 3.1 clearly is the speed of light in direction of its propagation  $\mathbf{v} = c \mathbf{n}$ . If relativistic effects are neglected, the third term in the Boltzmann equation is redundant, because no external forces are present. The collision rate in case of photons has to be described by the interaction of radiation and matter, so the according term in Eq. 3.1 has to contain the difference of emitted and absorbed energy per time and per photon energy. Taking all of this into account the radiative transfer equation is obtained as

$$\begin{aligned} \frac{1}{c h \nu} \left[ \frac{\partial I_\nu}{\partial t} + c \mathbf{n} \frac{\partial I_\nu}{\partial \mathbf{x}} \right] &= \frac{\eta_\nu - \chi_\nu I_\nu}{h \nu} \\ \Rightarrow \boxed{\frac{1}{c} \frac{\partial I_\nu}{\partial t} + \mathbf{n} \frac{\partial I_\nu}{\partial \mathbf{x}}} &= \eta_\nu - \chi_\nu I_\nu, \end{aligned} \quad (3.2)$$

with total emissivity  $\eta_\nu$  and total absorption coefficient  $\chi_\nu$ .

### 3.1.2. Time-independent, spherical symmetric equation in co-moving frame

In this work the radiative line transfer equation is used in the time-independent form (first term in Eq. 3.2 vanishes) for the calculations of the shocked atmospheres of Mira variables. That means that only *snapshots* of hydrodynamical shock wave structures will be calculated. A brief explanation should clarify why this method is appropriate.

In *LTE* the diffusion time for photons at large optical depth  $t_{\text{diff}} = l/c$  is much smaller than the hydrodynamical time scale  $t_{\text{hydro}} = L/a$ , because  $L \gg l$  and  $a \ll c$  ( $L$ : scale

---

<sup>1</sup>Bold symbols indicate vectors.



height of the atmosphere,  $l$ : mean free path of photons,  $a$ : sound speed and  $c$ : speed of light). *Here the assumption of a time independent treatment is well justified.* However, in the shocked regions of Mira atmospheres presumably NLTE (non local thermodynamical equilibrium) is the appropriate description. Here the situation changes: the thermalisation parameter  $\epsilon$  (roughly the relation of collision rates to spontaneous emission) enters the consideration and then  $t_{\text{diff}}/t_{\text{hydro}} \sim \frac{(la)/(Lc)}{\epsilon^2}$ . The thermalisation parameter becomes much smaller than 1 in regions of line formation, hence  $t_{\text{diff}}/t_{\text{hydro}} \gg 1$ , so a time independent treatment would *not* be justified. However, the extreme velocity gradient in the shock sets an upper limit to the optical depth a photon must penetrate before it can escape freely. For shocks the interaction region becomes very small and hence, the radiation is only coupled to the local conditions again. *The assumption a time-independent equation is therewith justified in this case, too* (private communication with D. Mihalas). We hence set the time-independent radiative transfer equation

$$\frac{dI_\nu}{ds} = \eta_\nu - \chi_\nu I_\nu, \quad (3.3)$$

with the path element  $ds = \mathbf{n} d\mathbf{x}$ .

To study the *extended* circumstellar envelopes of Mira variables the appropriate geometry to be chosen is the spherical symmetry. This also yields a general tool for regions close to the photosphere ( $\sim$  planar) as aspired to examine in this work, because as a limiting case the planar geometry is maintained. The path element in spherical symmetry is given by

$$\frac{d}{ds} = \frac{dr}{ds} \frac{\partial}{\partial r} + \frac{d\theta}{ds} \frac{\partial}{\partial \theta} = \mu \frac{\partial}{\partial r} + \frac{1}{r} (1 - \mu^2) \frac{\partial}{\partial \mu}; \quad (3.4)$$

with  $\mu = \cos \theta$ , where  $\theta$  is the angle between the line of sight outwards directed normal. Constituting this into Eq. 3.3 one obtains the spherically symmetric, time-independent equation:

$$\left( \mu \frac{\partial}{\partial r} + \frac{1 - \mu^2}{r} \frac{\partial}{\partial \mu} \right) I_\nu = \eta_\nu - \chi_\nu I_\nu; \text{ here } I_\nu = I(r, \mu, \nu). \quad (3.5)$$

To account for an *arbitrary velocity field* the co-moving frame formalism (CMF) (Mihalas et al. 1975) is utilised. Here, in contrast to the Sobolev approximation (see Mihalas 1978), monotonic but also non-monotonic velocity gradients can be handled. Another advantage is that the opacities in the CMF are isotropic, which cannot be achieved in the observer's frame (see also Mihalas 1978). For the intensity calculations only a small frequency interval that covers the full line profile width around the transition frequency  $\nu_0$  needs to be considered, which is a big computational advantage.

To develop the according CMF equation the path element  $ds$  at the fixed observer's frequency must be transformed into the co-moving frame in the following way

$$\left( \frac{\partial}{\partial s} \right)_\nu \mapsto \left( \frac{\partial}{\partial s} \right)_{\nu'} + \left( \frac{\partial \nu'}{\partial s} \right)_\nu \left( \frac{\partial}{\partial \nu'} \right)_s, \quad (3.6)$$

here the values denoted with a prime are in the CMF. The derivation  $(\partial\nu'/\partial s)_\nu$  appears because for each diminutive change  $\Delta s$  along the path the frequency in the CMF  $\nu'$  is changing due to the velocity gradient in the moved atmosphere. Utilising the Doppler shift  $\nu' = \nu - \nu_0 \mu (v/c)$ , where  $\nu_0$  is the laboratory frequency of the line centre, and only allowing for radial velocity fields  $v(r)$  the derivation in spherical symmetry is then given by

$$\begin{aligned} \left(\frac{d\nu'}{ds}\right)_\nu &= -\frac{\nu_0 v(r)}{c} \frac{d\mu}{ds} - \frac{\nu_0 \mu}{c} \frac{dv(r)}{ds} \\ &= -\frac{\nu_0 v(r)}{c} \left( \mu \frac{\partial \mu}{\partial r} + \frac{1-\mu^2}{r} \frac{\partial \mu}{\partial \mu} \right) - \frac{\nu_0 \mu}{c} \left( \mu \frac{\partial v(r)}{\partial r} + \frac{1-\mu^2}{r} \frac{\partial v(r)}{\partial \mu} \right) \\ &= -\frac{\nu_0 v(r)}{c} \frac{1-\mu^2}{r} - \frac{\nu_0 \mu^2}{c} \frac{dv(r)}{dr}. \end{aligned} \quad (3.7)$$

The time-independent, spherical symmetric radiative transfer equation in the CMF is hence given by

$$\boxed{\mu \frac{\partial I_\nu}{\partial r} + \frac{1-\mu^2}{r} \frac{\partial I_\nu}{\partial \mu} - \frac{\nu_0 v(r)}{c r} \left( \mu^2 \frac{d \ln v(r)}{d \ln r} + 1 - \mu^2 \right) \frac{\partial I_\nu}{\partial \nu} = \eta_\nu - \chi_\nu I_\nu}, \quad (3.8)$$

with the abbreviation  $\nu = \nu'$  for the frequency in the CMF.

However, the calculation of the radiative transfer in the CMF is somewhat more complicated, because instead of an ordinary differential equation a partial differential equation has to be solved along each ray. Also the results need to be transferred back into the observer's frame, before one can compare them with observations.

### 3.1.3. Opacities

The opacities — namely the total emissivity  $\eta_\nu$  and the total absorption coefficient  $\chi_\nu$  — are the particular parts of the radiative transfer equation (Eq. 3.8) which describe the coupling between the radiation field and the atmospheric matter. The atmosphere generally consists of free electrons, a multitude of ions, atoms and molecules, and in case of Miras in particular also of dust particles. Various processes between the photons and these constituents like bound-bound, bound-free and free-free transitions but also scattering interactions can take place.

In a *bound-bound* transition a line photon is absorbed respectively emitted by an atom, ion or molecule causing a transition of an electron from a bound state to another. In these interactions either a line photon is produced or destroyed in the line of sight or if both the absorption and emission process cause a line photon to escape with slightly changed energy in a direction different to the incident photon then this is to be viewed as a scattering process.

The *bound-free* transitions describe processes where the photon is absorbed by an atom, ion or molecule causing an ionisation, where a bound electron escapes with finite energy, respectively a free electron recombines by emitting a photon.

An unbound electron moving in the electro-magnetic field of an ion interacts in a *free-free* process where it absorbs a photon which transfers its kinetic energy to the electron. The reverse process is leading to the emission of a photon (Bremsstrahlung).

Additionally, *scattering* interactions of photons with all constituents of the atmosphere can occur, which add to the continuum.

All these contributions to the total emissivity and absorption coefficient have to be taken into account, which are divided into the line (l), the continuum (c) and the scattering (sca) contribution:

$$\eta_\nu = \eta_l \phi_\nu + \eta_c + \eta_{sca}, \quad (3.9)$$

$$\chi_\nu = \chi_l \phi_\nu + \chi_c + \chi_{sca}. \quad (3.10)$$

Here  $\phi_\nu$  is the profile function, which has been taken to be the same for emission and absorption; this assumption will be further explained in Sec. 3.1.4.

The following sections outline all parts of the opacities and adjustments made for this work in greater detail.

### 3.1.3.1. Scattering opacity

In the extended atmosphere of Mira variables different scattering partners of the photons will be present. For instance, in the cool circumstellar envelopes molecules are expected to play the major role, so Rayleigh scattering will be important especially in these parts.

With the simplifying consideration that in the relatively hot regions close to the stellar photosphere mainly non-relativistic electrons contribute to the scattering term, only *Thomson scattering* is considered in the studies presented here. Thomson scattering has the advantage of being coherent in the frame in which the electron is at rest before the photon collision takes place, that is, the frequency of the outgoing photon is equal to that of the incoming one. Also the scattering is assumed to be isotropic, meaning that the scattered radiation is emitted equally into all solid angles. The Thomson scattering opacities are therewith given as

$$\chi_{sca} = \sigma_e n_e \quad (3.11)$$

$$\eta_{sca} = \chi_{sca} J_\nu = \sigma_e n_e J_\nu. \quad (3.12)$$

Here  $n_e$  is the particle density of the electrons and  $\sigma_e = 8\pi e^4/(3m_e^2 c^4)$  the corresponding cross section, which has been verified by quantum mechanical calculations for the limit of low photon energies ( $h\nu \ll mc^2$ ). Since this work analyses the visible light ( $\nu \sim 10^{14} \text{ s}^{-1}$ ) in Miras, this is well justified. However, for higher photon energies (e.g. X-rays) the proper quantum mechanical cross sections have to be applied.

Note that  $\eta_{sca}$  depends on the mean intensity  $J_\nu$ , which is the zero-order moment of the intensity. As a consequence, the right hand side of the radiative transfer equation (Eq. 3.8) incorporates the solution of the left hand side of the equation. This type of equation is an integro-differential equation, which must be solved via an iteration procedure (see Sec. 3.2.3).

### 3.1.3.2. Continuum opacity

For a detailed analysis of spectral lines, e.g. if an accurate line profile modelling is aspired, the contributions of the atmospheric matter to the background intensity need to be known precisely. There exist different methods of calculating mean opacities for several millions of spectral lines and different element abundances including dust. For instance, the method of opacity sampling calculating the mean gas opacities by Planck or Rosseland means can be utilised.

However, for the work presented here, which aims rather for a qualitative modelling of total normalised line flux ranges (cf. Sec. 4), it is appropriate to use a somewhat simpler approach. Due to the fact that the number of emitting and absorbing atoms is proportional to the radial gas density  $\rho(r)$ , the continuum opacity is described in the following way

$$\chi_c(r) = 2 \cdot 10^{-4} \cdot \rho(r). \quad (3.13)$$

This approach is chosen according to Bowen (1988) and assumes that the opacity variation in the considered temperature-density region is small. The constant factor is chosen arbitrarily, but is adapted to properly calculated values from Alexander et al. (1983). This simplified consideration has developed to be a standard approach, if one does not use the results of the opacity sampling.

### 3.1.3.3. Line opacity

The absorption/emission of a line photon from/to the line of sight by an atom, ion or molecule are determined by the three bound-bound processes: spontaneous and induced emission and the counterpart of the latter the absorption. In order to obtain the line absorption coefficient and the line emissivity these processes are outlined in the following.

Consider a number of atoms  $n_i$  being in state  $i$  which are capable to absorb a photon with energy  $h\nu_{ij}$  causing an excitation of the atom from level  $i$  to  $j > i$ . The rate at which energy is absorbed from the line of sight is then given by

$$\alpha_\nu I_\nu = n_i h\nu_{ij} \frac{B_{ij}}{4\pi} \phi_\nu I_\nu. \quad (3.14)$$

Here  $\alpha_\nu$  denotes the so far uncorrected absorption coefficient per unit volume, the profile function is given by  $\phi_\nu$  (see Sec. 3.1.4) and  $B_{ij}$  is the Einstein coefficient for absorption, describing the number of absorptions per time. Note that  $B_{ij} = f_{ij} \pi e^2 / (m_e h \nu_{ij})$ , so one can recover the classical description of the absorption coefficient with the oscillator strength  $f_{ij}$ . However, it is much more convenient regarding the later coding to describe these processes via the Einstein coefficients.

In case of the induced emission the radiation field stimulates the transition from level  $j > i$  to level  $i$  and a photon coherent to the initial one is emitted. Hence, the rate of the induced emission is proportional to  $I_\nu$  and the energy emitted is then given by

$$\eta_\nu^{\text{ind}} = n_j h\nu_{ij} \frac{B_{ji}}{4\pi} \phi_\nu I_\nu, \quad (3.15)$$

with the Einstein coefficient for induced emission  $B_{ji}$ .

However, the spontaneous emission is not caused by the radiation field, here an electron simply changes from level  $j > i$  to level  $i$  and emits a photon. The energy emitted via spontaneous emission is

$$\eta_{\nu}^{\text{sp}} = n_j h \nu_{ij} \frac{A_{ji}}{4\pi} \phi_{\nu}, \quad (3.16)$$

where  $A_{ji}$  is the Einstein coefficient for spontaneous emission.

It should be noted, that if one Einstein coefficient is known then the others can be determined with the aid of the Einstein relations

$$B_{ji} = \frac{g_i}{g_j} B_{ij} \quad (3.17)$$

$$A_{ji} = \frac{2h\nu_{ij}^3}{c^2} B_{ji} \quad (3.18)$$

with the statistical weights of the quantum states  $g_i, g_j$ .

Now the line absorption coefficient and line emissivity can be finally determined. Since both  $\alpha_{\nu}$  and  $\eta_{\nu}^{\text{ind}}$  depend linearly on the radiation field, they can be summarised to an effective absorption, viewing the induced emission as a “negative” absorption. Hence,  $\alpha_{\nu}$  (Eq. 3.14) must be corrected for induced emission, obtaining the line absorption coefficient

$$\chi_l = \frac{h \nu_{ij}}{4\pi} \phi_{\nu} (n_i B_{ij} - n_j B_{ji}). \quad (3.19)$$

The line emissivity is then determined by the spontaneous emission

$$\eta_l = \frac{h \nu_{ij}}{4\pi} \phi_{\nu} n_j A_{ji}. \quad (3.20)$$

Note that all quantities are either given by atomic databases being atomic quantities ( $\nu_{ij}$ ,  $A_{ji}$ ,  $g_i, g_j$ ) or can be calculated ( $\phi_{\nu}$ ). Only the occupation numbers  $n_{i,j}$  have to be determined in a more sophisticated way, especially in a NLTE situation (see Sec. 3.1.5).

### 3.1.4. Profile function

There are three mechanisms preventing that a spectral line can form as a pure delta peak: Firstly, the so called *natural damping*, which even occurs in an isolated atom. Due to the fact that all energy levels (except for the ground state) have a finite life time set by their decay via the radiation process itself. So according to the principle of uncertainty  $\Delta E \Delta t \geq \hbar$ , the atomic level will show an energy uncertainty  $\Delta E$ . Secondly, if the atom is part of an ensemble, additionally *pressure broadening* via collisions with other atoms or charged particles will perturb the emitted light wave, causing a line broadening. And thirdly, the thermal motions of the atoms in the ensemble lead to different Doppler shifts of the re-emitted photons which cause a *Doppler broadening*. Hence, such a broadened spectral line needs to be described by a profile function  $\phi_\nu$ .

Generally, the profile function can be different for absorption and emission transitions, but under the assumption of complete redistribution it is taken to be the same function for both. This is strictly speaking only fulfilled if the re-emitted photons will be statistically distributed in the line profile. E.g. thermally Doppler broadened profiles satisfy this assumption well.

A purely Doppler broadened profile is given by a *Gauss profile*

$$\varphi(\Delta \nu) = \frac{1}{\sqrt{\pi} \Delta \nu_D} \exp \left\{ \frac{-(\Delta \nu)^2}{(\Delta \nu_D)^2} \right\}, \text{ with } \int_{-\infty}^{+\infty} \varphi(\Delta \nu) d(\Delta \nu) = 1. \quad (3.21)$$

Here  $\Delta \nu = (\mu v/c) \nu_0$  is the Doppler shift,  $\Delta \nu_D = (\nu_0/c) v_{th}$  the Doppler width, where  $v = v(r) + v_{th}$  is the total velocity and  $v_{th} = (2kT/m)^{1/2}$  is the thermal velocity.

If collisional broadening is also taken into account the line profile has to be described by a *Lorentz profile*

$$\psi(\Delta \nu) = \frac{\Gamma}{4\pi} \frac{1}{\pi (\Delta \nu)^2 + (\Gamma/4\pi)^2}, \quad (3.22)$$

where  $\Gamma = \Gamma_{col} + \Gamma_{rad}$  is the damping consisting of collisional and radiative damping (the latter being equivalent to the natural damping mentioned above), which are given by

$$\Gamma_{col} = 2 \sigma_{cp} N_{cp} v \quad (3.23)$$

and

$$\Gamma_{rad} = \sum_{i < j} A_{ij}. \quad (3.24)$$

Here,  $\sigma_{cp}$  is the collision cross section of the collision partner (here electrons),  $N_{cp}$  the number density of collision partners,  $A_{ij}$  the Einstein coefficients for spontaneous emission and the mean collision velocity is given by

$$v = \sqrt{\frac{8kT}{\pi} \left( \frac{1}{m_{atom}} + \frac{1}{m_{cp}} \right)}. \quad (3.25)$$

For a realistic line profile Doppler broadening as well as collisional broadening of the line profiles must be accounted for. To achieve this, a folding of the Gauss and Lorentz profile has to be carried out obtaining the *Voigt profile*, which is applied in the calculations of this work:

$$\phi(a, v) = \frac{1}{\sqrt{\pi} \Delta \nu_D} H(a, v) = \frac{1}{\sqrt{\pi} \Delta \nu_D} \frac{a}{\pi} \int_{-\infty}^{+\infty} \frac{\exp\{-y^2\}}{(v - y)^2 + a^2} dy , \quad (3.26)$$

with the normalised Voigt function

$$\int_{-\infty}^{+\infty} H(a, v) dv = \sqrt{\pi} \quad (3.27)$$

and the following parameters:

$$y \equiv \frac{\Delta \nu}{\Delta \nu_D} , \quad v \equiv \frac{\nu - \nu_0}{\Delta \nu_D} , \quad a \equiv \frac{\Gamma}{4\pi \Delta \nu_D} . \quad (3.28)$$

### 3.1.5. Rate equation

The occupation numbers  $n_i$  of all atomic levels  $i$  have to be determined in order to calculate the line opacities (Eqs. 3.19 and 3.20) and are therewith essential to solve the radiative transfer equation (Eq. 3.8). In case of a local thermodynamical equilibrium (LTE), where the influence of the collisions on the atmospheric material is locally dominating over the radiative rates, the material becomes thermalised and the occupation numbers can hence be described by a simple Boltzmann law

$$\frac{n_i}{n_j} = \frac{g_i}{g_j} \exp \left\{ \frac{h \nu_{ij}}{k T} \right\} , \quad (3.29)$$

which only depends on the statistical weights of the levels  $g_{i,j}$ , the excitation energy  $h \nu_{ij}$  and the gas temperature  $T$ . Assuming LTE is always a simplification, which can only be appropriate in the innermost parts of a Mira atmosphere.

In the extended Mira atmosphere NLTE has to be assumed. In such a non-local situation the state of the atmospheric material is strongly dominated by the radiation field. That is, radiation emitted from one part of the atmosphere can influence the occupation number of the material in a different part of the atmosphere. Here, for each place in the atmosphere the occupation numbers must be calculated in order to determine the line opacities. Therefore all transition rates leading out of and into all atomic levels have to be taken into account. Basically there are two types of transition rates, namely the collisional and radiative rates, which are defined in the following.

In an ionised plasma collisions between atoms and charged particles will be the main contribution due to their Coulomb interactions. Here mainly electrons will play the most important role as collision partners, because the collision rate is proportional to

the velocity (Eq. 3.30) and their velocity is a factor of  $\sqrt{m_{\text{ion}}/m_e} = \sqrt{A m_H/m_e} \approx 43\sqrt{A}$  bigger than those of ions with atomic weight  $A$ .

The rate for collisional excitation is then given by:

$$C_{ij} = n_e \int_{v_0}^{\infty} \sigma_{ij}(v) f(v) v dv , \quad (3.30)$$

where  $n_e$  is the particle density of the electrons,  $f(v)$  the Maxwell velocity distribution and the cross section of the atoms is denoted by  $\sigma_{ij}(v)$ . The integration limit  $v_0$  is the velocity belonging to the threshold energy  $E_{ij} = \frac{1}{2} m_e v_0^2$ .

In case of equilibrium the collisional excitation and de-excitation are in detailed balance, so the de-excitation rate can be calculated as

$$n_i C_{ij} = n_j C_{ji} \Rightarrow C_{ij} = C_{ji} \frac{g_i}{g_j} \exp \left\{ \frac{h\nu_{ij}}{kT} \right\} , \quad (3.31)$$

using the Boltzmann distribution (Eq. 3.29) for the ratio of the equilibrium occupation numbers.

The radiative rate coefficients are defined via the Einstein coefficients (see also Sec. 3.1.3.3). The absorption rate depends on the radiation field and is given by

$$R_{ij} = \int B_{ij} \phi_\nu J_\nu d\nu = B_{ij} \bar{J} , \text{ for } j > i , \quad (3.32)$$

with the mean frequency integrated intensity  $\bar{J} \equiv \int \phi_\nu J_\nu d\nu$ .

Likewise, the rate for all radiative transitions leading to a lower energetic level is determined by the induced emission and the spontaneous emission, and hence is defined as

$$R_{ji} = A_{ji} + B_{ji} \bar{J} , \text{ for } j > i . \quad (3.33)$$

To set up the rate equation again stationarity is assumed (see also discussion in Sec. 3.1.2) and hence the time derivation of the level population vanishes. With the assumption of a statistical equilibrium, all transitions leading out of the according energy level are equal to the ones leading into the level, and so the rate equation for level  $i$  is given by

$$n_i \sum_{j \neq i} (R_{ij} + C_{ij}) = \sum_{j \neq i} n_j (R_{ji} + C_{ji}) . \quad (3.34)$$

Considering for each level  $i$  all transitions from atomic levels  $j$  ( $j < i$  and  $j > i$ ) and using Eq. 3.30 – 3.33 in Eq. 3.34 one yields the corresponding rate equation

$$\boxed{\begin{aligned} \sum_{j>i} n_j (A_{ji} + B_{ji} \bar{J}) + \sum_{j<i} n_j B_{ji} \bar{J} + \sum_{j \neq i} n_j C_{ji} = \\ \sum_{j>i} n_i B_{ij} \bar{J} + \sum_{j<i} n_i (A_{ij} + B_{ij} \bar{J}) + \sum_{j \neq i} n_i C_{ij} \end{aligned}} . \quad (3.35)$$



The left hand side of Eq. 3.35 represents the gain terms for level  $i$ , whereas the right hand side represents the loss terms. Note, that because of the appearance of the frequency integrated mean intensity  $\bar{J}$ , the rate equation is coupled to the radiative transfer equation (Eq. 3.8). To solve for the needed occupation number  $n_i$  one has to apply an iteration procedure.

### 3.1.6. Fe II-model-atom

For the investigation of Fe II emission lines in this work a suitable Fe II-model-atom has to be used. In general, ionised iron is a very complex ion as can be seen in the term diagram Fig. 3.2 (note that every level in this diagram consists of various sub-levels). Here only a simplified term diagram of Fe II is shown, which is taken from Merrill (1958) and only presents the most important transitions for astrophysical spectra. Nevertheless, this scheme already shows how many energetic levels have to be included if one properly wants to model FeII-lines in astrophysical objects.

To investigate the relevant Fe II and [Fe II] emission lines in this thesis, the FeII-model-atom has therefore been treated as a 3-level-atom as depicted in Fig. 3.2, including one permitted line: M38, 4583.84 Å and one forbidden emission line: 6F, 4457.95 Å. The necessary atomic data has been taken from the CHIANTI database<sup>2</sup> (Dere et al. 1997).

As one can see in Fig. 3.2, both transitions of the 3-level-subsystem are in fact coupled, because the M38 transition ends up in the upper level of the 6F transition and the forbidden transition connects to the ground state. Other transitions like the M37 and 20F transition, which could also influence the population of the upper level of the 6F transition are neglected in the calculations. This is without doubt a simplification of the real FeII-atom but nevertheless represents a model-atom which is easy to handle. The enormous advantage is that individual radiative and collisional rates as well as level population numbers can be checked straightforwardly in the rate equation Eq. 3.35, in order to test the solution. Also since we are facing an huge amount of models which need to be calculated for the parameter studies presented in Chapter 4, it seems adequate in a first study to use a simple model-atom instead of a very detailed one which would slow down the individual model calculations tremendously.

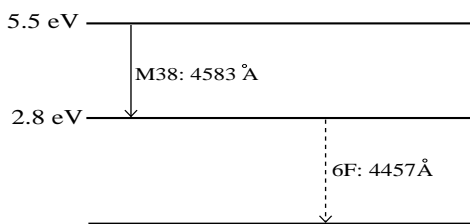


Figure 3.1.: Scheme of the 3-level-model-atom including one permitted line (M38) and one forbidden emission line (6F).

<sup>2</sup><http://www.solar.nrl.navy.mil/chianti.html>

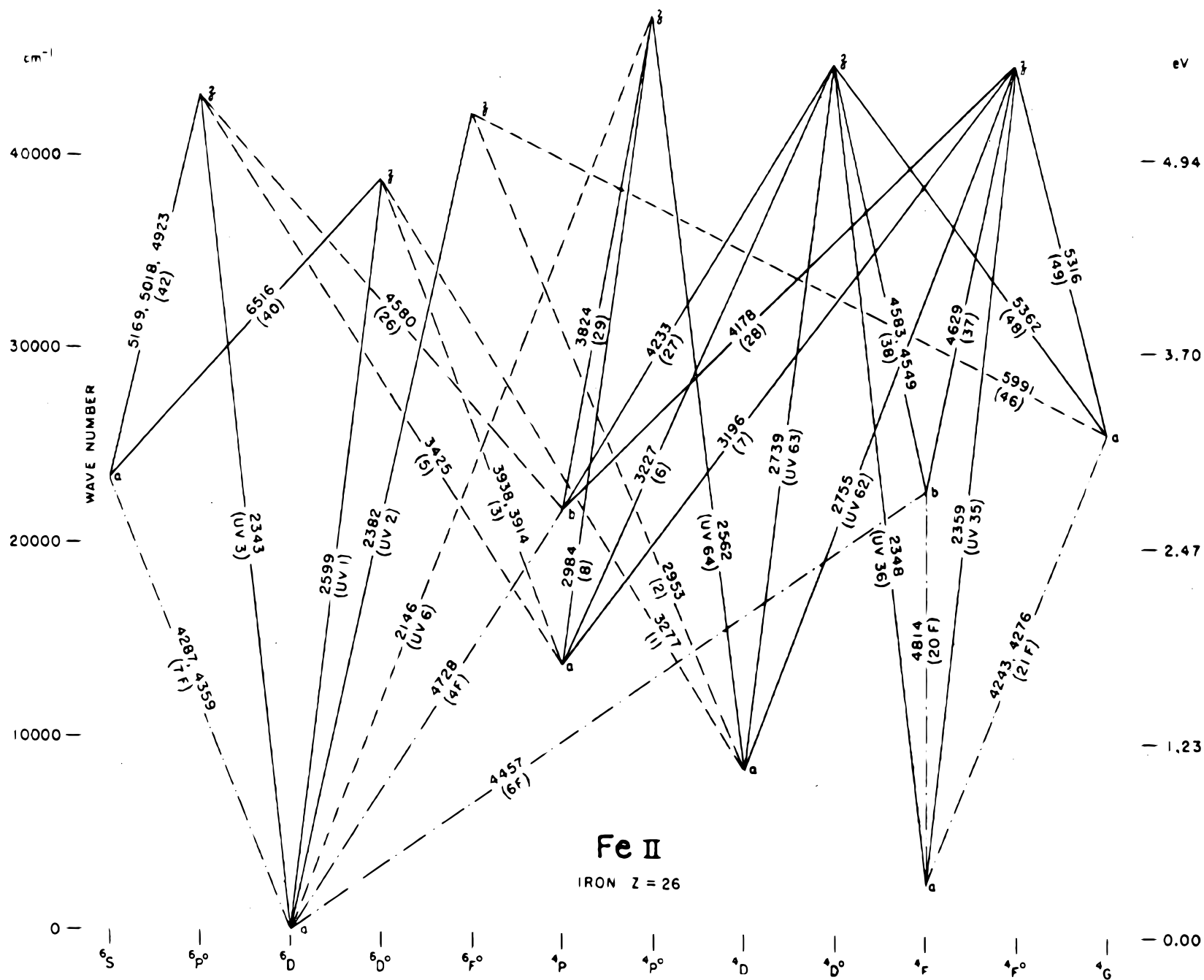


Figure 3.2.: Term diagram of Fe II taken from Merrill (1958).

## 3.2. Solution methods

### 3.2.1. The p-z-coordinates

First of all, it is convenient to introduce the p-z-coordinates for the numerical treatment of the radiative transfer. They describe the characteristics of the differential equation, which are rays perpendicular to the symmetry axis. They are chosen in such a way that they are tangential to the radial spheres as depicted in Fig. 3.3. The distance from the centre of the star to the ray is called impact parameter and denoted by  $p$ , the path along the ray is named  $z$ . For the path element one then gets

$$\left. \frac{\partial}{\partial z} \right|_p = \left. \frac{\partial r}{\partial z} \right|_p \frac{\partial}{\partial r} + \left. \frac{\partial \mu}{\partial z} \right|_p \frac{\partial}{\partial \mu} = \mu \frac{\partial}{\partial r} + \frac{1 - \mu^2}{r} \frac{\partial}{\partial \mu} \quad (3.36)$$

and the radiative transfer equation in the CMF (Eq. 3.8) can then be rewritten as

$$\frac{1}{\chi_\nu} \frac{\partial I_\nu}{\partial z} - \frac{1}{\chi_\nu} \frac{\nu_0 v(r)}{c r} \left( \mu^2 \frac{d \ln v(r)}{d \ln r} + 1 - \mu^2 \right) \frac{\partial I_\nu}{\partial \nu} = S_\nu - I_\nu, \quad (3.37)$$

where  $S_\nu = \eta_\nu / \chi_\nu$  is the source function.

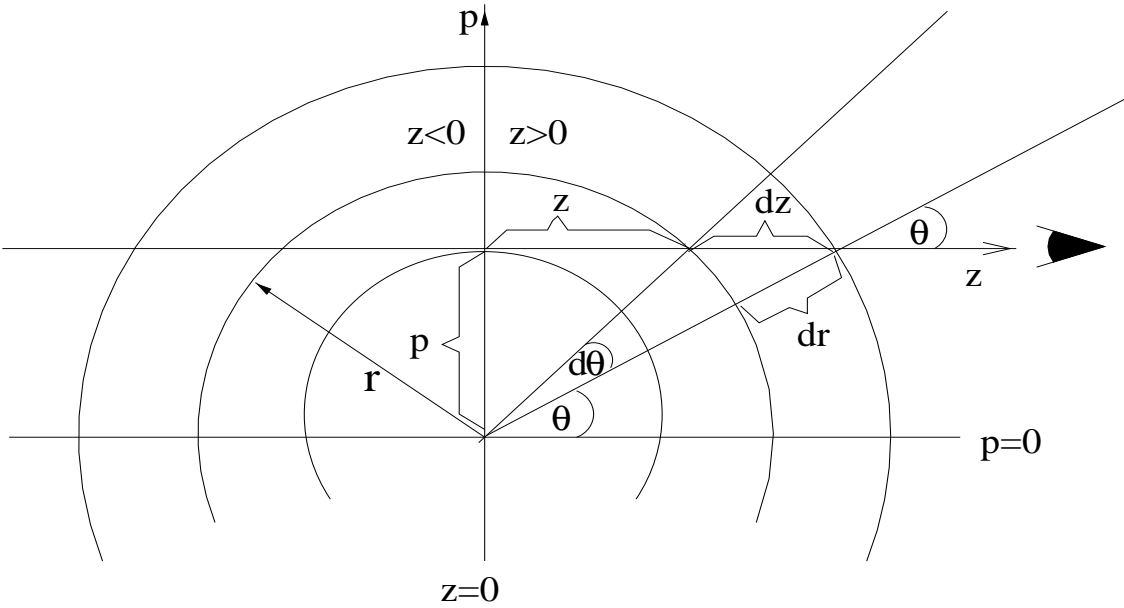


Figure 3.3.: p-z-coordinates

### 3.2.2. Feautrier method

The basic idea of the method by Feautrier is to achieve a half space splitting. The depth points can be chosen symmetrical to  $z = 0$ , so Eq. 3.37 can be rewritten for outwards directed rays with  $I^+ = I(\nu, +z, p)$  respectively inwards directed rays with  $I^- = I(\nu, -z, p)$  as

$$\pm \frac{1}{\chi_\nu} \frac{\partial I_\nu^\pm}{\partial z} - \frac{1}{\chi_\nu} \frac{\nu_0 v(r)}{c r} \left( \mu^2 \frac{d \ln v(r)}{d \ln r} + 1 - \mu^2 \right) \frac{\partial I_\nu^\pm}{\partial \nu} = S_\nu - I_\nu^\pm . \quad (3.38)$$

Introducing the intensity-like and flux-like Feautrier variables

$$u(\nu, z, p) \equiv \frac{1}{2}(I^+(\nu, z, p) + I^-(\nu, z, p)) \quad (3.39)$$

and

$$v(\nu, z, p) \equiv \frac{1}{2}(I^+(\nu, z, p) - I^-(\nu, z, p)) \quad (3.40)$$

at fixed impact parameters (so  $p$  will be neglected in the following), one gets two partial differential equations of first order when adding, respectively subtracting, the two equations in Eq. 3.38, namely

$$\frac{1}{\chi(\nu, z)} \frac{\partial}{\partial z} u(\nu, z) - \gamma(\nu, z) \frac{\partial}{\partial \nu} v(\nu, z) = -v(\nu, z) \quad (3.41)$$

and

$$\frac{1}{\chi(\nu, z)} \frac{\partial}{\partial z} v(\nu, z) - \gamma(\nu, z) \frac{\partial}{\partial \nu} u(\nu, z) = S(\nu, z) - u(\nu, z) , \quad (3.42)$$

with the abbreviation

$$\gamma(\nu, z) \equiv \frac{1}{\chi(\nu, z)} \frac{\nu_0 v(r)}{c r} \left( \mu^2 \frac{d \ln v(r)}{d \ln r} + 1 - \mu^2 \right) . \quad (3.43)$$

So the aim of the Feautrier method becomes clear: a partial differential equations of first order in  $I_\nu$  was transferred into *two* coupled partial differential equations of first order in  $u$  and  $v$ . Constituting  $v$  in Eq. 3.42 by Eq. 3.41 one gets a differential equation of second order in the intensity-like variable  $u$ . Solving this equation instead of the original one has the advantage that one can now fix *two* boundary conditions, which leads to a much more stable numerical solution.

#### 3.2.2.1. Boundary conditions

The solution of the system Eq. 3.41 and Eq. 3.42 requires spatial boundary conditions for the spherical symmetric atmosphere surrounding an opaque core with radius  $R_c$ . For the outer boundary condition of a single star treated in this work, it is assumed that no

radiation falls on the atmosphere from the outside. Hence  $I^-(\nu, z_{max}) = 0$  and Eq. 3.39 and 3.40 give  $u(\nu, z_{max}) = v(\nu, z_{max})$ . Therewith Eq. 3.41 can be written as<sup>3</sup>

$$\frac{1}{\chi(\nu, z_{max})} \frac{\partial}{\partial z} u(\nu, z_{max}) - \gamma(\nu, z_{max}) \frac{\partial}{\partial \nu} u(\nu, z_{max}) = -u(\nu, z_{max}) . \quad (3.44)$$

For the inner boundary condition one has to distinguish between the core rays, these are rays that intersect the core with an impact parameter  $p < R_c$ , and non-core rays with  $p > R_c$ . For the latter one can take advantage of the flux conservation at the symmetry axes  $z = 0$ , leading to  $I^-(\nu, z = 0) = I^+(\nu, z = 0)$  and therewith  $v(\nu, z = 0) = 0$ . Using Eq. 3.41 one then obtains

$$\frac{1}{\chi(\nu, z = 0)} \frac{\partial}{\partial z} u(\nu, z = 0) = 0 \quad \text{for } p > R_c. \quad (3.45)$$

If the core is optically thick at all frequencies then the continuum optical thickness exceeds one and the line optical thickness is larger than the thermalisation length. In this case, the core is to be treated as being opaque and a diffusion approximation needs to be applied. Close to the core the atmosphere can be treated as being approximately planar, so the diffusion approximation in the planar form yields

$$I(\nu, z_{min}) = B_\nu + \frac{\mu}{\chi(\nu, R_c)} \left| \frac{dB_\nu}{dr} \right| , \quad (3.46)$$

where  $B_\nu$  is the Planck function and  $dB_\nu/dr$  its radial gradient at  $r = R_c$ . For the inward and outward directed rays one then obtains the diffusion limit for the inner boundary of the core rays

$$v(\nu, z_{min}) = \frac{|\mu|}{\chi(\nu, R_c)} \left| \frac{dB_\nu}{dr} \right| = \frac{(R_c^2 - p^2)^{\frac{1}{2}}}{R_c \chi(\nu, R_c)} \left| \frac{dB_\nu}{dr} \right| \quad \text{for } p < R_c. \quad (3.47)$$

### 3.2.2.2. Initial condition

An initial condition is needed due to the frequency dependence of the CMF. In case of a monotone and in outward direction increasing velocity function, namely  $v(r) \geq 0$  and for all  $r$ :  $dv(r)/dr \geq 0$  it is easily obtained. In that case all line photons are always red-shifted and as a result of this the blue frequency edge of the line profile cannot retrieve any line photons and hence can just be filled by continuum photons of the fitting frequency. The initial condition is then given by  $u(\nu_{max}, z) = u_c$  and the gradient at the blue frequency end can be fixed as  $\partial u / \partial \nu = 0$ . Therewith Eq. 3.41 and 3.42 reduce to the static equations and can be solved straightforwardly.

However, for the case of shocked atmospheres the situation is somewhat more complicated, because the velocity gradient can be negative in the very narrow shock fronts and hence will change signs along a ray. Normally in such cases one would have to use a

---

<sup>3</sup>Note that a fixed ray is considered so the variable  $p$  is suppressed in all equations.

switch changing from blue wing to red wing initial conditions. However, for the studies of Fe II emission lines, where only one shock front at the time is investigated, one can take advantage of the fact that these emission lines are in fact narrow ( $< 40 \text{ km s}^{-1}$ ) so the continuum will not have changed significantly from the blue to the red wing of the line. Hence, blue wing initial conditions are assumed in case of the negative velocity gradient in the very narrow shock front region. The validity of this method has to be thoroughly checked and clearly will not hold for calculating wide lines, like e.g. Balmer lines. Nevertheless it has already successfully been applied by Bolick et al. (2002) for the calculation of various narrow rotational-vibrational CO absorption in the shocked circumstellar envelopes of LPVs. This work also shows a comparison to the results of Winters et al. 2000b, which gives an excellent agreement.

### 3.2.3. The accelerated lambda iteration

Solving the radiative transfer one is facing two difficulties: firstly the radiative transfer is an integro-differential equation due to the appearance of the mean intensity in the scattering emissivity (Sec. 3.1.3, Eq. 3.12) and secondly, in case of NLTE the according rate equation (Sec. 3.1.5, Eq. 3.35) needs to be solved, which incorporates the mean frequency integrated intensity. So the radiative transfer equation itself requires an iterative method, but also the NLTE solution of the coupled system of rate equation and radiative transfer equation needs an iterative procedure. In this work the accelerated lambda iteration is used, which is briefly outlined in the following.

The radiative transfer equation can be written as an operator equation

$$T_{\mu\nu} J_{\mu\nu} = S_{\mu\nu} , \quad (3.48)$$

where  $T_{\mu\nu}$  is the differential operator at frequency  $\nu$  along the ray with direction  $\mu$ ,  $J_{\mu\nu} = (1/4\pi) \int d\Omega I_{\mu\nu}$  is the mean intensity (the straight average over all solid angles), and  $S_{\mu\nu}$  the source function. The formal solution is then given by

$$J_{\mu\nu} = T_{\mu\nu}^{-1} [S_{\mu\nu}] . \quad (3.49)$$

The inverse of the differential operator is to be identified with the *lambda operator*, namely  $T_{\mu\nu}^{-1} = \Lambda_{\mu\nu}$ . The explicit form of the lambda operator can be very sophisticated. Also the solution of the equation is too slow using the exact operator. The main idea of the accelerated lambda iteration is to speed up the convergence of the solution by introducing an approximated operator  $\Lambda_{\mu\nu}^*$ . The exact lambda operator is then given by the identity

$$\Lambda_{\mu\nu} = \Lambda_{\mu\nu}^* + (\Lambda_{\mu\nu} - \Lambda_{\mu\nu}^*) . \quad (3.50)$$

To construct a suitable approximated lambda operator is the real challenge, especially in the case of the CMF where additional frequency-dependent terms appear in the radiative transfer equation. Basically one is applying two approximations for the construction of  $\Lambda_{\mu\nu}^*$  in the CMF: firstly all non-local contributions to the intensity-like variable  $u$  are neglected considering only the resonance zone of the line (related to the

Sobolev approach) and secondly, all additional non-diagonal elements in the operator originating from contributions of the flux-like variable  $v$  will be neglected, achieving a *pure local*, approximated operator. This will in practice be a tri-diagonal matrix. Of course, the obtained approximated lambda operator is always underestimating the exact operator, but since  $\Lambda_{\mu\nu}^*$  is only used to accelerate the solution and the according terms will cancel out in case of convergence it does not change the solution in any way. Since here only a general overview of the iteration method should be given, the interested reader is referred to the basic papers of Rybicki & Hummer (1991) and Rybicki & Hummer (1992) where details of the operator splitting are discussed and Puls (1991) for the explicit construction of the approximated lambda operator in the CMF.

Eq. 3.50 is used as the basis of the iteration technique to solve the radiative transfer (Eq. 3.49), which yields

$$\begin{aligned} J_{\mu\nu}^{n+1} &= \Lambda_{\mu\nu}^* S_{\mu\nu}^{n+1} + (\Lambda_{\mu\nu} - \Lambda_{\mu\nu}^*) [S_{\mu\nu}^n] \\ &= \Lambda_{\mu\nu}^* S_{\mu\nu}^{n+1} - \Lambda_{\mu\nu}^* S_{\mu\nu}^n + \Lambda_{\mu\nu} [S_{\mu\nu}^n] \\ &= \Lambda_{\mu\nu}^* S_{\mu\nu}^{n+1} - \Lambda_{\mu\nu}^* S_{\mu\nu}^n + J_{\mu\nu}' . \end{aligned} \quad (3.51)$$

Here  $n$  is the iteration index and  $n + 1$  denotes the new iteration step. In case of convergence  $\Lambda_{\mu\nu}^* S_{\mu\nu}^n = \Lambda_{\mu\nu}^* S_{\mu\nu}^{n+1}$  so these terms will cancel in Eq. 3.51 and  $J_{\mu\nu}^{n+1} = J_{\mu\nu}'$  will be the exact solution.

Introducing likewise the iteration scheme for the frequency integrated mean line intensity

$$\begin{aligned} \overline{J}_l^{n+1} &= \overline{\Lambda}_l^* S_l^{n+1} - \overline{\Lambda}_l^* S_l^n + \overline{J}_l' \\ &= \overline{\Lambda}_l^* S_l^{n+1} + \overline{J}_l^{\text{eff}} , \end{aligned} \quad (3.52)$$

with the *modified* and frequency integrated approximated lambda operator

$$\overline{\Lambda}_l^* = \int \Lambda_l^* r_l^n d\nu , \quad (3.53)$$

$$\text{where } r_l^n = \frac{\chi_l^n}{(\chi_l^n + \chi_{c,l} + \chi_{sca,l})} , \quad (3.54)$$

one easily obtains an iteration scheme<sup>4</sup> for the rate equation by simply inserting Eq. 3.52 into Eq. 3.35:

$$\begin{aligned} &\sum_{j>i} \left( A_{ji} (\mathbf{1} - \overline{\Lambda}_l^*) [n_j] - (n_i B_{ij} - n_j B_{ji}) \overline{J}_l^{\text{eff}} \right) \\ &- \sum_{j<i} \left( A_{ij} (\mathbf{1} - \overline{\Lambda}_l^*) [n_i] - (n_j B_{ji} - n_i B_{ij}) \overline{J}_l^{\text{eff}} \right) \\ &+ \sum_{j \neq i} (n_j C_{ji} - n_i C_{ij}) = 0 . \end{aligned} \quad (3.55)$$

---

<sup>4</sup>Here  $\mathbf{1}$  is the identity operator.

The iteration method then proceeds as follows: (i) an initial choice for the old population is made,  $S_{\mu\nu}^n$ , as well as  $\Lambda_{\mu\nu}$  and  $\Lambda_{\mu\nu}^*$  are constructed and the radiative transfer (Eq. 3.51) is solved, (ii) using the newly obtained  $\overline{J}_l^{\text{eff}}$  and  $\overline{\Lambda}_l^*$  the rate equation (Eq. 3.55) is solved to get the new population. (iii) Regarding this to be the old populations in the next cycle the iteration process is carried on until convergence is achieved and the exact solution  $J'_{\mu\nu}$  is gained.

### 3.3. The code nlte-fell

The NLTE radiative transfer code `nlte-feII` is based on the theory and solution methods presented in the previous sections Sec. 3.1 and 3.2. Here the flow chart (Fig.3.4) should clarify the different calculation steps.

- **Hydrodynamical input models:** Generally the NLTE radiative transfer code requires a radial thermodynamical structure at a fixed time, consisting of the velocity of the gas  $v(r)$ , gas density  $\rho(r)$  and gas temperature  $T_g(r)$ . This input is given by various model calculations in this work, e.g. stationary wind models, CHILD-code models (Fleischer et al. 1992), modified CHILD-code models (Schirrmacher et al. 2002) or gas-box models (Woitke et al. 1996a,b). All named models are analysed in chapter 4.

- **Equilibrium chemistry:** The radial gas temperature and density structure from the input model is passed on to the program `ggchem.f`, which has been developed by C. Dominik 1992 and later refined by Woitke 1997. This Fortran-code is linked to the NLTE radiative transfer code (a C-code) and calculates an equilibrium chemistry in order to get  $n_{\text{FeII}}(r)$  and  $n_e(r)$ . The iron ionisation is treated in statistical equilibrium, taking into account photo-ionisation, direct recombination and collisional ionisation, including excited levels, on the basis of a 200-level FeI and a 142-level FeII model atom (Woitke & Sedlmayr 1999).

- **FeII-data:** Next the according FeII-data obtained from the CHIANTI database is read in, which consists of the energies of the levels, Einstein coefficients and statistical weights for the model-atom. Also parameters to calculate the collision rates for FeII-electron collisions at the given radial temperature are read. Since the radial gas temperature structure is now known, the collision rates can hence also be calculated.

- **Grids:** Now that the required radial input structure is complete the calculation of the radial grid (in p-z-coordinates) and frequency grid in the CMF is carried out. Now it is also possible to generate some spatial and frequency dependent values such as the profile function and the LTE-opacities for the start model.

- **Solving the NLTE radiative transfer in CMF:** In the following the LTE start model is calculated, which is necessary to obtain the initial condition for the frequency integration. Then, the NLTE line radiative transfer in CMF is calculated. For the numerical treatment the differential equations are discretised according to Richtmyer and Morton (1967) giving a 2nd order (partly 1st order) discretisation (see Mihalas et al. 1975). The accelerated lambda operator is applied to solve the according integro-differential equation (scattering problem).



• **Rate equation-system:** NLTE radiative transfer requires a coupled solution of the radiative transfer equation and the rate equation, which is carried out with the accelerated lambda operator until convergence is reached. In each iteration cycle the solution of the rate equation-system itself is obtained with a standard gauss-solver and an adjusted, damped newton iteration according to Engeln-Müllges & F. Uhlig (1996).

• **Transformation into Observer's frame:** The solution of the NLTE line radiative transfer in CMF needs to be transferred back into the Observer's frame. The obtained line fluxes and profiles are then comparable to the observational results.

• **Observations:** The comparison of the calculated Fe II emission line profiles, shifts and fluxes to the observed once will then reveal the thermodynamical conditions which are essential for the emission of the Fe II and [Fe II] emission lines.

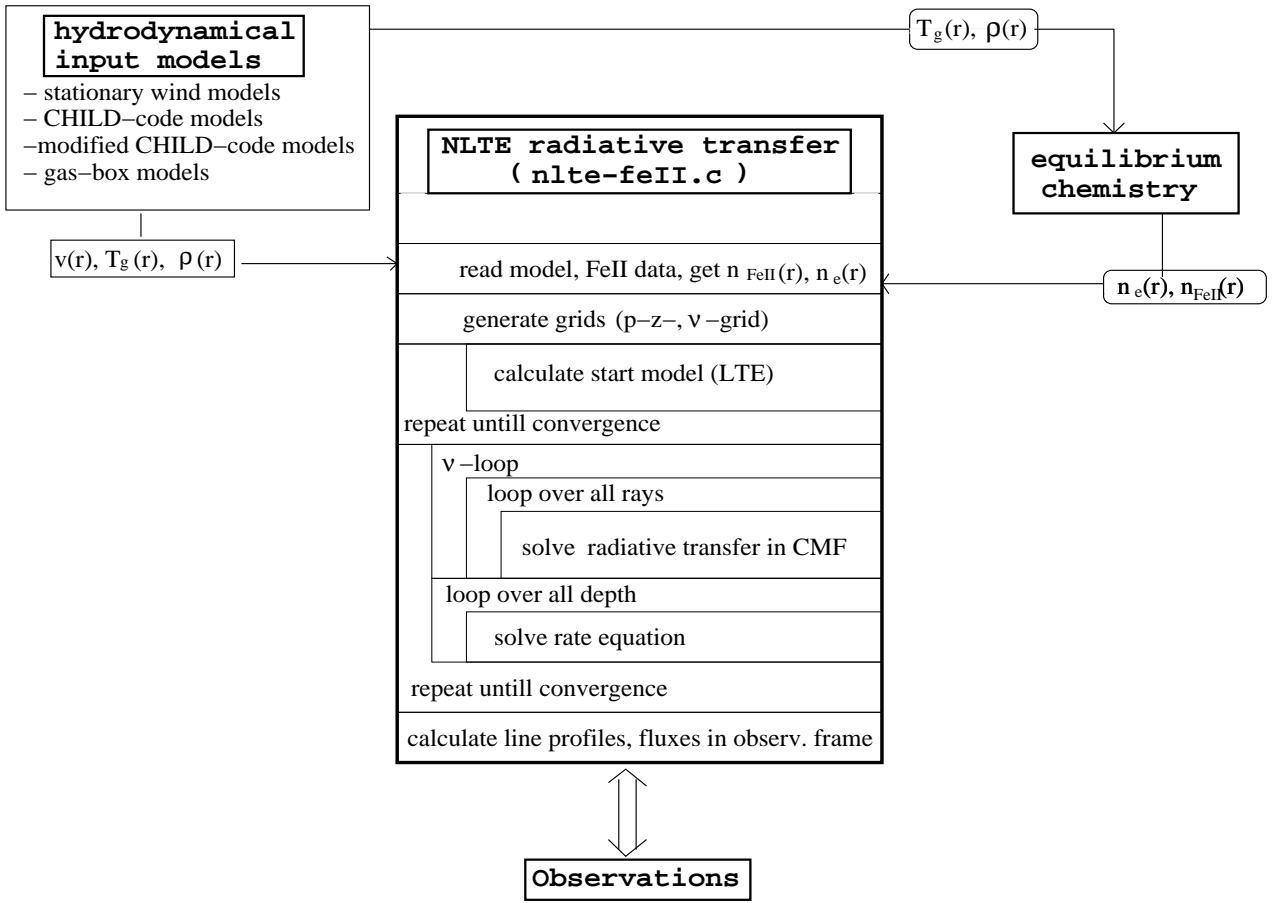


Figure 3.4.: Flow chart of the calculations.



## 4. Fe II & [Fe II] emission lines as a diagnostic tool in M-type Miras

The time-dependent high-resolution observations of the M-type Mira sample presented in chapter 2 has already shown that metal emission lines are good candidates to probe the inner atmospheric layers of these variables. In particular the Fe II and [Fe II] emission lines have turned out to be an excellent diagnostic tool to analyse the thermodynamical conditions of the inner dust-forming regions of M-type Miras. This will be well founded more detailed in the following.

It has been observed that the Fe II and [Fe II] emission lines appear around minimum visible light at phase  $\phi \sim 0.3 - 0.5$  in the M-type Mira variables. To estimate the region of their emission, a pulsation period of 1 yr and a shock wave velocity<sup>1</sup> of  $v_s = 10 - 40 \text{ km s}^{-1}$  is assumed. This leads to a distance of  $1 - 4 R_*$  that the shock front travels in one period. With the assumption that the shock emerges from the photosphere (defined to be at optical depth one) at maximum  $\phi = 0.0$ , the radial position of the shock front  $R$  around minimum ( $\phi = 0.5$ ) can be approximated as  $\sim R = 1.5 - 3 R_*$ . (This rough approximation neglects the shock deceleration on the way through the atmosphere and the underlying wind velocity profile). *Thus, the Fe II and [Fe II] emission lines are approximately emitted from the inner dust-forming zone.*

Furthermore these emission lines show an erratic appearance: they were only detected in M-type Miras which have just had a bright light maximum. This points out that only stronger-than-normal shocks lead to the excitation of these lines. With the aid of detailed modelling one can take advantage of this fact and derive *upper boundaries for the thermodynamical conditions in the emitting regions.*

The utilisation of the Fe II and [Fe II] emission lines as a diagnostic tool requires a bridging between the detailed observation (chapter 2) and theory. For this the detailed NLTE radiative line transfer modelling via the programm `nlte-feII`, presented in chapter 3, mainly concentrates on the permitted line M38, 4583.84 Å and the forbidden line

---

<sup>1</sup>Note that the observed shock velocity  $v_{\text{obs}}$  in chapter 2 is to be identified with the sum of the velocity of the shocked gas and the underlying mean wind velocity.

6F, 4457.95 Å (see Sec 3.1.6). Hence, the observational findings of these particular lines, which must be fulfilled by the radiative transfer modelling, will be briefly summarised:

- Fe II (M 38) and [Fe II] 6F emission lines show up simultaneously.
- Lines have gauss-like, resp. square-like, profiles with no systematic line shifts.
- Normalised peak fluxes  $F_n = F_{\text{line}}^{\text{peak}} / F_{\text{cont}}$  are in the limits  $1.2 < F_n < 10$ .
- Line ratios are  $F_{\text{M38}} / F_{\text{6F}} \sim 1$ .
- Lines should originate from a region  $\sim 1.5 - 3 R_*$ .

With the investigations of the Fe II and [Fe II] emission lines basically three main problems are tackled: (i) the question whether shock waves are essential to explain Fe II emission lines should be answered, (ii) the possible correlation of the appearance of Fe II and [Fe II] emission lines with dust formation will be illuminated and (iii) the precise thermodynamical parameters leading to the emission of these lines will be determined. Different input models were used to achieve these aims: for (i) one can utilise quite simple models to check whether a simple temperature peak can lead to the emission of these lines, whereas for (ii) one needs a detailed time series of hydrodynamical models with a self-consistently included dust complex, in order to compare the phase of emission of the Fe II and [Fe II] lines with the instant of the onset of dust formation. On the other hand for (iii) it is necessary to have detailed shock structures calculated by a given thermodynamical parameter combination at a fixed time in order to fit the observed line fluxes and derive the relevant thermodynamical conditions.

For that, first of all preliminary investigations were carried out in order to test if shock waves are necessary to excite Fe II emission lines. Sec. 4.1.1 outlines the according results for stationary wind models, whereas Sec. 4.1.2 presents models which have been modified by inserting an artificial temperature peak in the thermodynamical structure. These investigations strongly indicate the need for shock waves. In the following, the correlation between dust formation and Fe II & [Fe II] emission lines is investigated in details in Sec. 4.2. Fully self-consistent hydrodynamical models in two variants were used as input models, namely the so called *CHILD-code models* (see Sec. 4.2.1) and *modified CHILD-code models* with included NLTE heating/cooling functions (see Sec. 4.2.2). For a time series of the latter type of models NLTE radiative line transfer calculations were carried out, which clarify the connection of these lines to the onset of dust formation (Sec. 4.2.3). The emission region of the Fe II and [Fe II] lines in relation to the shock front is specified and discussed in Sec. 4.2.4. This sets the need for more detailed input models, so in Sec. 4.3 a multitude of so called *gas-box models* are utilised. Finally the specific thermodynamical conditions, namely the position of the shock in the atmosphere (Sec. 4.3.2), the ionised iron density (Sec. 4.3.2.1), the pre-shock density and the needed shock velocity amplitude (Sec. 4.3.3) that lead to the emission of Fe II and [Fe II] lines are specified.

## 4.1. Preliminary investigations

The basic condition for the emission of Fe II and [Fe II] lines is that ionised iron must be present in the Mira's atmosphere. For that the ionisation energy<sup>2</sup> of about  $\sim 16.2$  eV ( $\approx 2 \cdot 10^5$  K) must be reached in the stellar atmosphere. Consider for instance a stationary wind model with an effective temperature of  $T_{\text{eff}} \sim 3000$  K (e.g. R Leo, Jacob et al. 2000). Since the temperature will decrease further out in the atmosphere, the gas temperature at about  $5 R_*$  will approximately be  $T_g \leq 1000$  K. This already points out that in stationary wind models presumably no Fe II emission lines can be produced in the estimated region  $\sim 1.5 - 3 R_*$  due to the absence of Fe II. To probe these presumption, the following preliminary studies have been carried out.

### 4.1.1. Stationary wind models

As thermodynamical input simple stationary wind models (Winters 1994) were used. An example is depicted in the upper panel of Fig. 4.1. The used particle densities, as calculated from the program `ggchem.f`, are shown in the lower panel of Fig. 4.1. As one can see, the ionised iron density is around  $n_{\text{FeII}} \sim 1$  at  $1 R_*$  and decreases drastically towards the outer atmospheric layers. In fact hardly any Fe II is present in the atmosphere. Hence, the resulting line fluxes are zero. As expected, the stationary wind model will not produce any forbidden or permitted ionised iron line, because the ionised iron density is not sufficient.

### 4.1.2. Models with artificial temperature peaks

The investigations presented in Sec. 4.1.1 already confirm the necessity for high temperature zones in order to explain Fe II emission lines in M-type Mira atmospheres. To further investigate this, simple models with a high temperature peak which has been artificially inserted in the stationary wind model (Fig. 4.1) have been examined. Note, that the gas density is unchanged, which is not consistent with the perfect gas law and will presumably underestimate ionised iron densities. Nevertheless, for first test calculations this should be appropriate.

An example of such a model with a high temperature peak of  $T_{\text{peak}} \sim 8 \cdot 10^3$  at  $r = 1.5 R_*$  is depicted in Fig. 4.2, upper panel. The particle densities and the resulting normalised line fluxes are shown in the lower left, respectively right, panels of this figure. As one can see, the ionised iron density as well as the electron density increase at the high temperature peak, whereas neutral iron is destroyed as a result of the ionisation. The ionised iron density reaches the enormous amount of  $\log n_{\text{FeII}} \sim 10^8$  in the temperature peak, consequently the normalised fluxes of both the permitted M 38 and forbidden 6F emission lines are far too big compared to any observed flux value (see also appendix A). Artificially high temperature peaks at different radial positions in the estimated region  $\sim 1.5 - 3 R_*$  showed similar results.

---

<sup>2</sup>Note that the ionisation energy is measured from the ground state. A bound-free transition of electrons from higher energy levels would require less energy.

For these first simple studies probably the emitting volume has been chosen too big, leading to such high line fluxes. In reality a shock front and the resulting temperature peak are much narrower, which would presumably result in a moderate line flux. Nevertheless, these calculations already show that high temperature peaks are essential for the emission of the Fe II lines. Hence, these preliminary studies set the basis for the investigations of various shock models presented in the following.

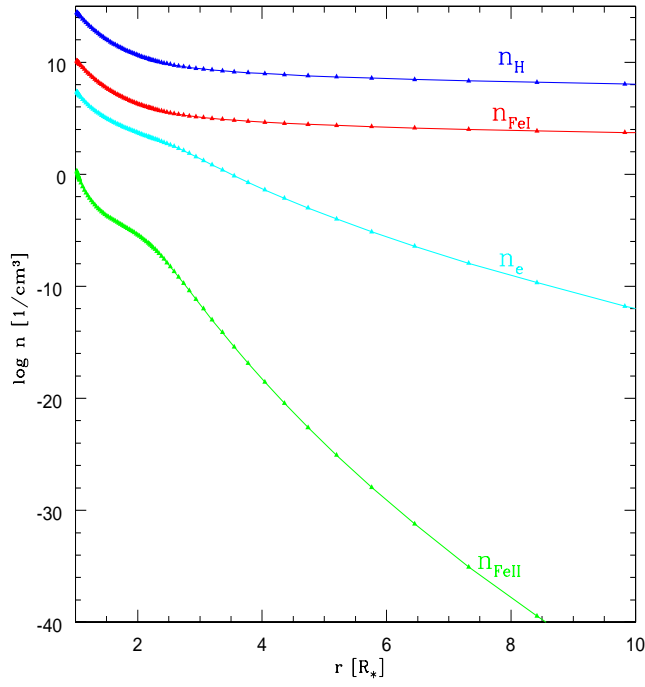
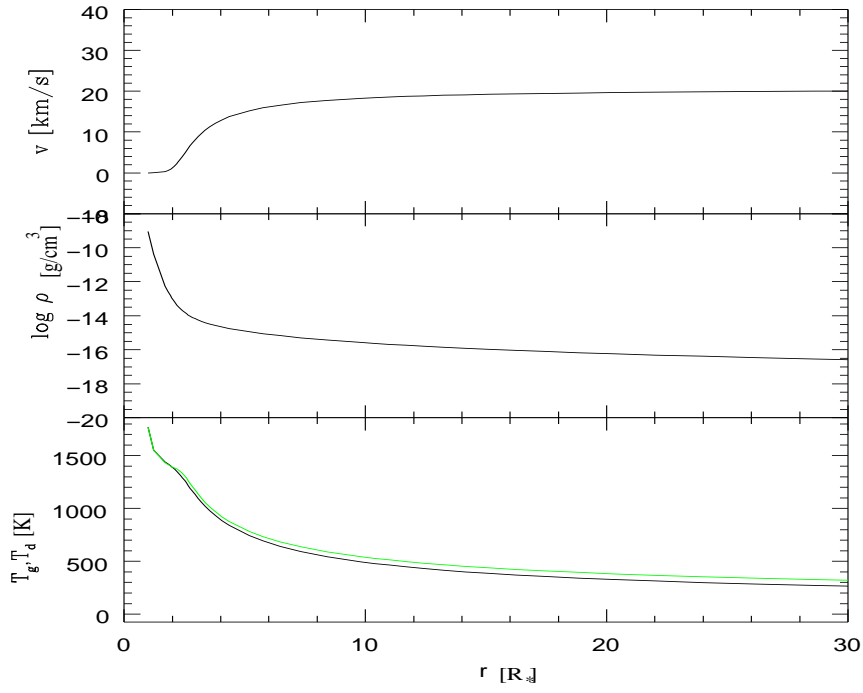


Figure 4.1.: *Upper*: Stationary wind model —  $v$ : velocity,  $\rho$ : density,  $T_g, T_d$ : gas and dust temperature (grey). *Lower*: Particle densities of H,  $e^-$ , FeI and FeII.

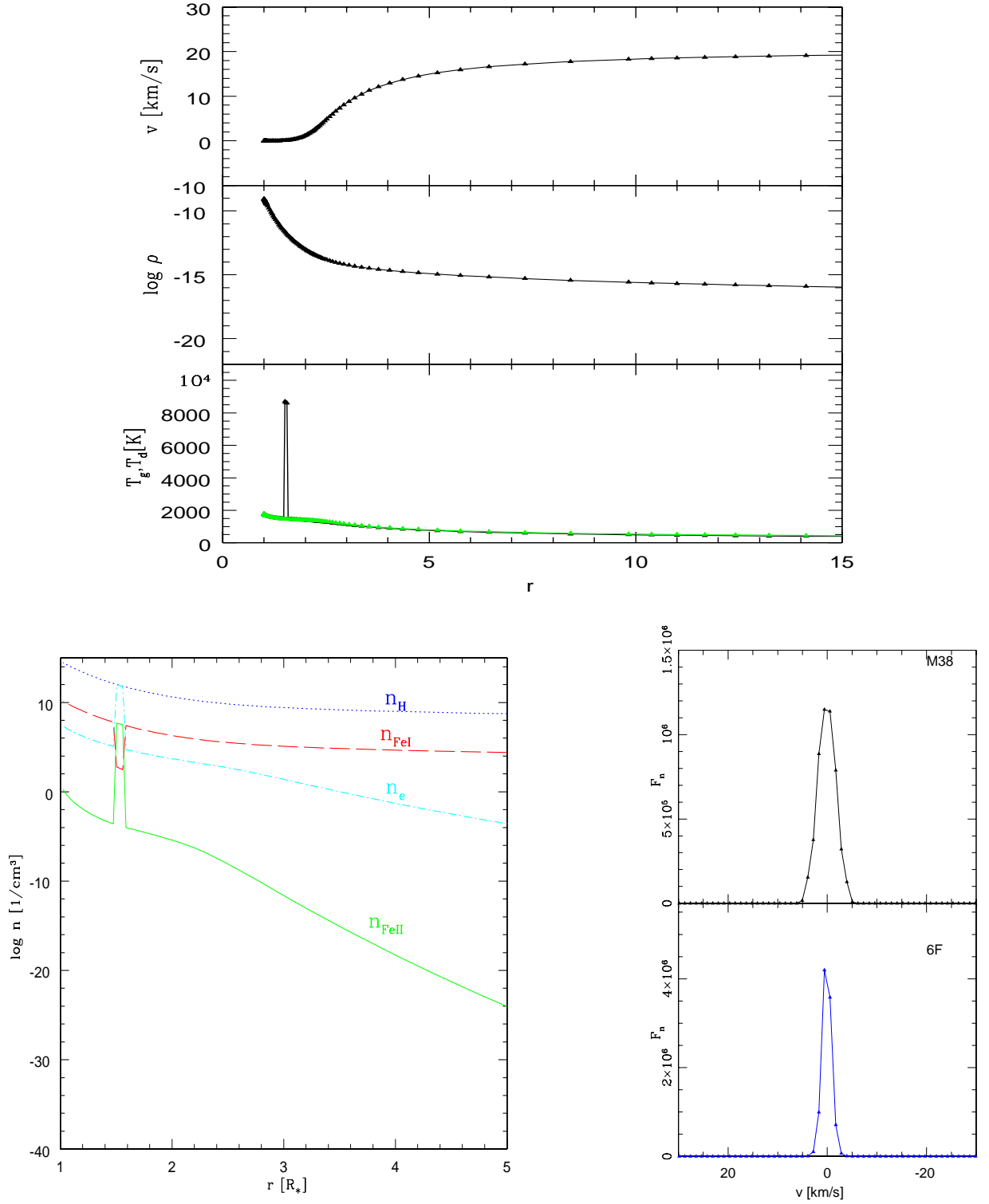


Figure 4.2.: *Left:* Similar model like Fig. 4.1, but with a artificial temperature peak at  $1.5 R_*$ . *Lower left:* Particle densities of H,  $e^-$ , FeI and FeII. *Lower right:* Resulting normalised fluxes for the lines M38 and 6F.



## 4.2. Correlation of dust formation and Fe II & [Fe II] emission lines

An important point in the exploration of the Fe II & [Fe II] emission lines is to answer the question of a possible connection between the excitation of these lines and the formation of dust in M-type Mira atmospheres. If this linkage can be proved, these particular emission lines can state as a probe to investigate the exact thermodynamical conditions shortly before and maybe also while the dust-formation process is proceeding.

The previous section has already pointed out that high temperature peaks — as produced in shock waves — are essential for the emission of Fe II & [Fe II] lines. On the other hand, theoretical models show that shock waves trigger the formation of dust (Wood 1979, Bowen 1988, Fleischer et al. 1992, Feuchtinger et al. 1993, Höfner & Dorfi 1997 and Winters et al. 2000a), namely the pulsation of the star generates shock waves which propagate through the atmosphere thereby increasing the mass density in the outer parts of the atmosphere. The passage of a shock leads to a sudden increase of the pressure, density and temperature of the gas. Behind the shock the gas cools via the emission of radiation, which leads to conditions that are favourable for dust formation. The shocks in the outer parts of the atmosphere thereby trigger the formation of dust. Radiation pressure acting on these dust grains finally drives the wind of these stars.

In order to analyse the potential correlation between the Fe II emission lines and dust formation, NLTE radiative line transfer calculations were carried out on two types of self-consistent hydrodynamical models, namely the so called *CHILD-code models* (Fleischer et al. 1992) presented in Sec. 4.2.1 and *modified CHILD-code models* (V. Schirrmacher 2002) presented in Sec. 4.2.2. Both kinds of models are carbon-rich models for C-type Mira variables, which are specified by the four fundamental stellar parameters  $M_*$ ,  $L_*$ ,  $T_{\text{eff}}$  and C/O and two additional quantities  $P$  and  $\Delta v_p$ , which describe the interior pulsation of the star (these models have a piston at the innermost grid point simulating the pulsation). The models include a consistent treatment of hydrodynamics, thermodynamics, chemistry, dust formation and growth and of the grey radiative transfer problem. Additionally, the modified models include NLTE heating- and cooling functions (Woitke et al. 1996a,b) in the thermodynamic calculations, which can result in high temperature peaks in the shocks waves up to  $\sim 10^4$  K in the inner  $1 - 5 R_*$ .

Actually, one would expect the use of oxygen-rich M-type Mira models for these investigations. Presently the only self-consistent hydrodynamical models calculating a whole circumstellar atmosphere with included dust for oxygen-rich M-type Miras are the models by Jeong (2000). These models so far do not include NLTE heating- and cooling functions, but use analytic functions instead and hence, they do not result in high temperature peaks in the shock fronts. The preliminary investigations already have shown, that high temperature peaks are essential for the emission of Fe II lines, so these models are not expected to lead to such emission lines. Consequently, these models are not used for the investigations and only the carbon-rich original CHILD-code models, which are similar in respect to the resulting low temperature peaks, are studied to give an example.

### 4.2.1. Studies of the CHILD-code models

For these investigations a CHILD-code model (Fleischer et al. 1992, Winters et al. 2000a) of a typical C-type Mira variable has been used, which is based on the following stellar input parameters: stellar mass  $M_* = 1 M_\odot$ , luminosity  $L_* = 10000 L_\odot$ , effective temperature  $T_{\text{eff}} = 2600 \text{ K}$ , carbon to oxygen ratio  $C/O = 1.3$ , pulsation period  $P = 650 \text{ d}$  and piston amplitude  $\Delta u_p = 4 \text{ km s}^{-1}$ . A schema outlining the complex interplay of all components in a Mira atmosphere is depicted in Fig. 4.3. Note however, that the cooling functions  $Q_{\text{rad}}$  are in the CHILD-code treated as simple analytic functions; *no NLTE cooling functions are included.*

A snapshot of this hydrodynamical model is presented in Fig. 4.4 in the upper panel. In the depicted inner 30 stellar radii of the atmosphere the shocks at  $r \sim 4, 11, 21$  and  $28 R_*$  can clearly be seen in the velocity, density and gas temperature structure. The formation of a new dust layer is especially apparent in the inner shock at  $r = 4 R_*$ , if one regards the degree of dust condensation  $f_c$ . In general, it is obvious that as a result of the periodic formation of dust layers in the post-shock regions of the shocks, an inhomogeneous radial dust distribution is produced. The corresponding number densities of Fe II, Fe I,  $e^-$  and H resulting from the equilibrium chemistry calculations are presented in Fig. 4.4, lower panel. Here only the inner 5 stellar radii are shown, since this is the approximated region for the emission of Fe II lines. As expected, the number density of ionised iron generally decreases further outward in the atmosphere because of decreasing temperature and density. The peak of  $\log n_{\text{FeII}}$  at  $r \sim 4.4 R_*$  is due to a shock, which leads to a temperature peak of  $T_g^{\text{peak}} \sim 1400 \text{ K}$  in this model calculation. However, this temperature peak is only resulting in an ionised iron density of  $\log n_{\text{FeII}} \sim -9$ , which is not sufficient to produce any Fe II emission lines. For the other shocks waves in this model no significant increase in temperature results and hence they produce even less ionised iron. The result of the NLTE radiative line transfer calculation is therefore not surprising: the line flux of the Fe II M 38 and [Fe II] 6F emission lines are zero.

These investigations have shown that the temperature peaks caused by shocks in the original CHILD-code models are not big enough to produce a sufficiently high ionised iron density and therewith do not lead to the emission of Fe II lines. Obviously, the analytical cooling functions of these models reproduce the hydro- and thermodynamical structure of the shock waves quite well, but systematically underestimate the shock temperature. Since this parameter is essential for the studies presented here, models which include NLTE coolings functions were used for the following studies.

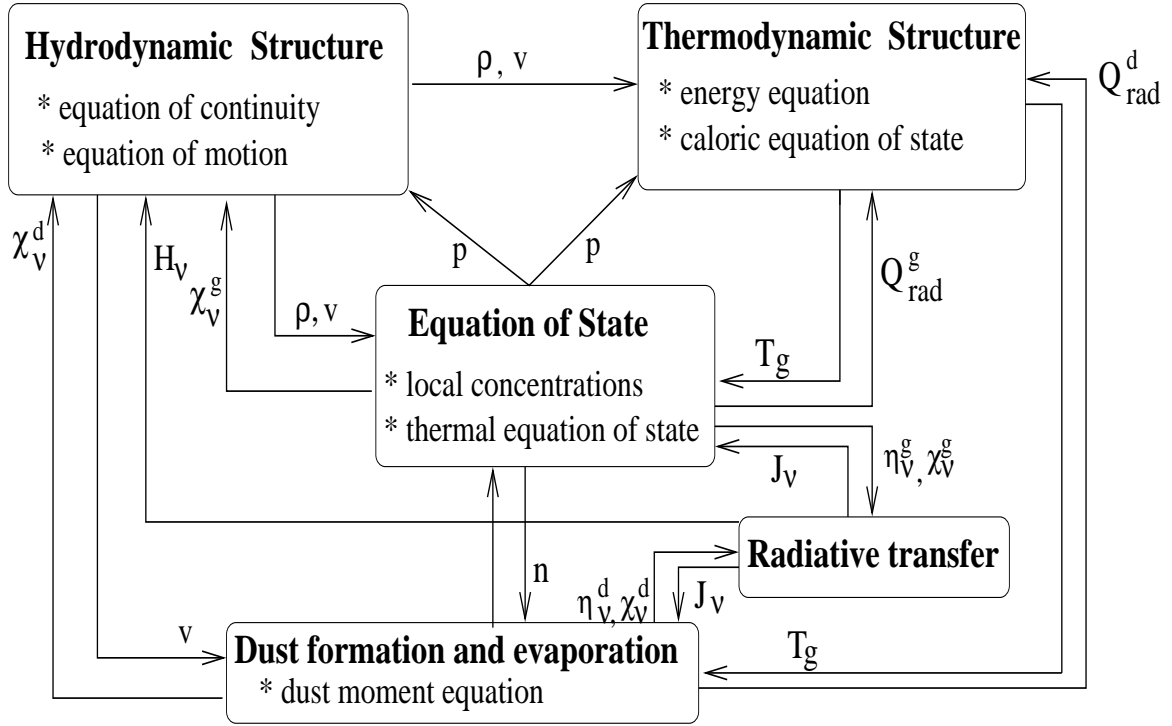


Figure 4.3.: Schema of the physical interplay in a Mira atmosphere, with  $p$ : pressure,  $v$ : velocity,  $T_g$ : gas temperature,  $\chi_v^{g,d}$ : absorption coefficient for gas/dust,  $\eta_v^{g,d}$ : emissivity for gas/dust,  $J_v$ : mean intensity,  $H_v$ : Eddington flux,  $Q_{\text{rad}}^{g,d}$ : analytic cooling functions for gas/dust and  $n$ : particle density.

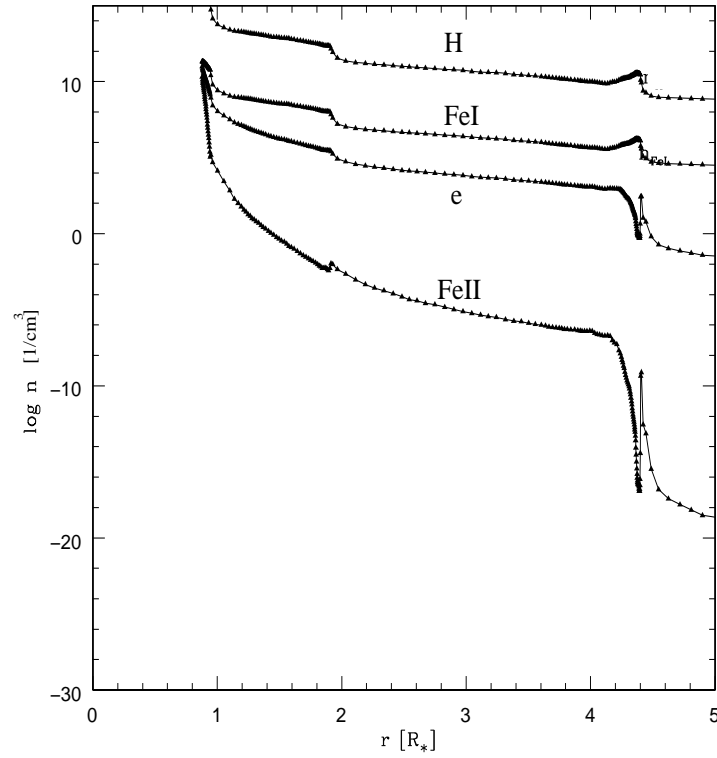
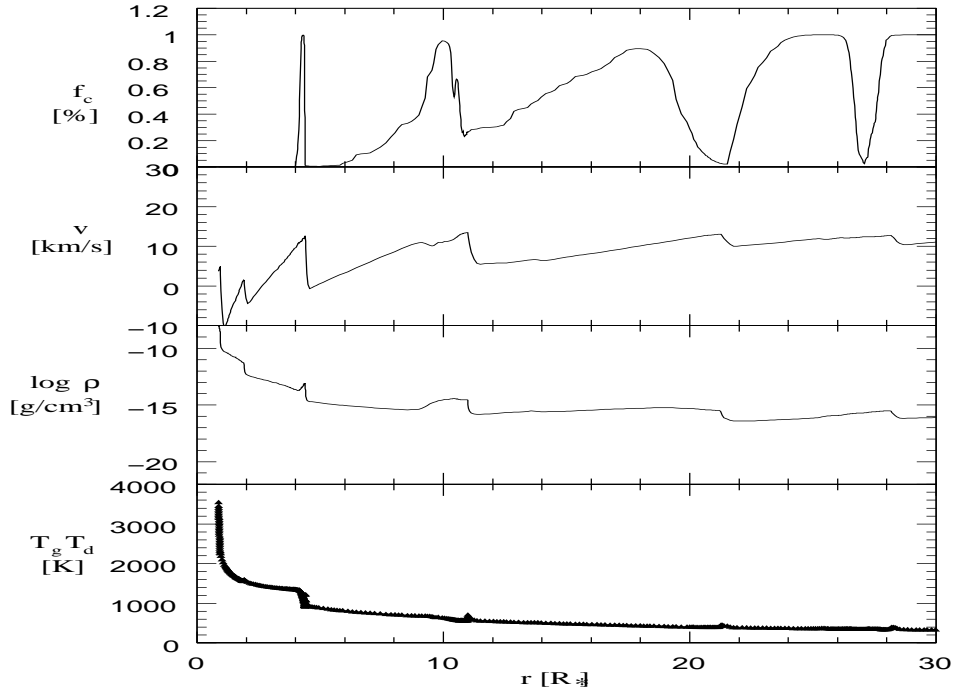


Figure 4.4.: *Upper*: Hydrodynamical model structure resulting from a CHILD-code *without* NLTE heating/cooling functions.  $f_c$ : degree of dust condensation ( $1 \equiv 100\%$ ),  $v$ : velocity,  $\rho$ : density,  $T_{g,d}$ : gas, dust temperature ( $T_d$  without peaks). *Lower*: Logarithm of number density of Fe II, Fe I,  $e^-$  and H.

### 4.2.2. Studies of modified CHILD-code models

In dynamical model calculations the thermodynamical equations of state play a major role. Local quantities like the pressure and gas temperature depend on the density and radiation field but also the latter variables are strongly determined by the pressure gradient as well as by emission and absorption of radiation, which are temperature dependent. Especially the determination of the local gas temperature via the first law of thermodynamics depends on the thermodynamical equations of state, which again depend on the utilised gas model. Here most works, including the original CHILD-code models, assume a thermal and caloric equation of state of an ideal gas and simple analytic cooling functions are used. The *modified CHILD-code models* use an improved description of the thermodynamical concept by Voitke (1996a) with NLTE heating and cooling functions, which are included in the hydrodynamical calculations of the CHILD-code. More details of this can be found in the master thesis of V. Schirrmacher (Schirrmacher 2000). The main results are, that the overall appearance of modified CHILD-code models is similar to the original CHILD-code models; however in compact models (with high mass or low luminosity) the modified models show a very distinct tendency towards high temperature peaks of the shocks in the inner stellar radii.

The upper panel of Fig. 4.5 presents a snapshot of such a hydrodynamical model, which was especially calculated using stellar input parameters suitable for the M-type Mira star R Leo (Jacob et al. 2000), but assuming a carbon-rich atmosphere (see C/O ratio): stellar mass  $M_* = 1 M_\odot$ , luminosity  $L_* = 4760 L_\odot$ , effective temperature  $T_{\text{eff}} = 3000 \text{ K}$ , carbon to oxygen ratio  $\text{C/O} = 1.8$ , pulsation period  $P = 310 \text{ d}$  and piston amplitude  $\Delta u_p = 2 \text{ km s}^{-1}$ . With the chosen parameters, the model is more compact and therewith hotter than the original CHILD-code model (Fig. 4.4). Moreover the maximum shock velocity turns out to be higher than in the original CHILD-code model and also the general density trend is lower.

At the depicted instant of time in Fig. 4.5, three shocks are apparent, which are located at  $r \sim 1.5, 7.2$  and  $12.8 R_*$ . It has been checked that the low temperature peaks in the latter two shocks do not produce a significant amount of Fe II, consequently they do not contribute to the Fe II emission line flux. So for the studies in particular the innermost shock at  $r \sim 1.5 R_*$  is of interest. Hence, the NLTE radiative transfer calculations have only been carried out for the region  $r = 1 - 5 R_*$ , neglecting the absorbing dust layers higher in the atmosphere. Since M-type Miras are less dust-enshrouded due their oxygen-rich chemistry than carbon-rich Miras (private communication with Dr. P. R. Wood), it seems appropriate to cut off the outer dust layers for the calculations in the lack of better input models.

As one can see, the inner shock at  $r \sim 1.5 R_*$  leads to a temperature peak of  $T_g^{\text{peak}} = 9 \cdot 10^3 \text{ K}$  and consequently the ionised iron density reaches  $\log n_{\text{FeII}} \sim 6$  (Fig. 4.5). The resulting normalised line fluxes for the two transitions M 38 and 6F in the calculated region are approximately in the range of observed fluxes, but tend to be slightly too high (see also appendix A).

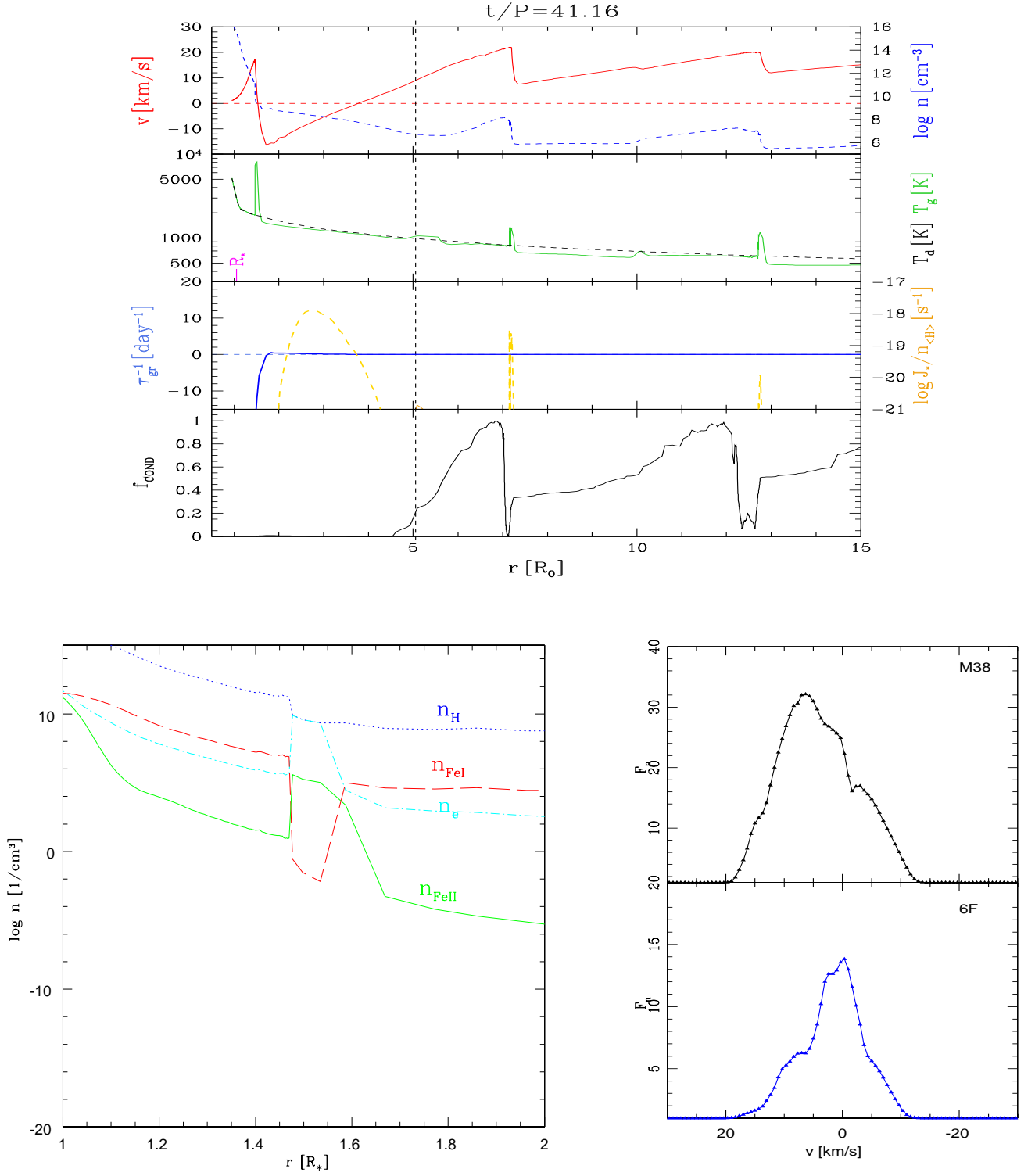


Figure 4.5.: *Upper*: Hydrodynamical model structure resulting from a CHILD-code with included heating/cooling functions:  $v$ : velocity,  $n$  (dashed): total number density,  $T_g$ : gas temperature and  $T_d$ : dust temperature resulting from the radiative temperature  $T_{rad} = T_d$ ,  $\tau_{gr}^{-1}$ : inverse time scale for dust growth,  $J_*/n_{<H>}$  (dashed): nucleation rate normed per hydrogen nuclei and  $f_c$ : degree of condensation. *Lower left*: Logarithm of number density of FeII, FeI,  $e^-$  and H. *Lower right*: Resulting normalised line fluxes for the M38 and 6F transitions.

### 4.2.3. Investigation of Fe II & [Fe II] emission lines in a pulsation cycle

The investigation of a time series of such modified CHILD-code models should now clarify: (i) if the observed phase of emission of the Fe II and [Fe II] can be obtained from the hydrodynamic models and most importantly (ii) if these are the same phases where dust-formation starts in the models.

Therefore, radiative transfer calculations have been carried out for a full pulsation cycle, starting at maximum visible light (corresponding to minimum stellar radius in the data) up to the next maximum, resulting in approximately 50 calculations. Each calculation has been extended only up to 5 stellar radii in order to zoom into the region of interest and to investigate the formation and rise of the innermost shocks (see also explanation in the previous section).

The notation is as follows: phase  $\phi = 0.0$  is at maximum visible light (minimum radius of the pulsating star). The maximum stellar radius is reached at phase  $\phi = 0.6$ , which is the minimum visible light and then  $\phi = 1.0$  is the next maximum. The parameters of the hydrodynamical models are: velocity  $v$ , total number density  $n$  (dashed), gas temperature  $T_g$ , black body temperature  $T_{bb}$  (dashed) also taken as dust temperature, inverse time scale for dust growth  $\tau_{gr}^{-1}$ , nucleation rate normalised per hydrogen nuclei  $J_*/n_{<H>}$  (dashed) and the degree of condensation  $f_{cond}$ . The respective right panels depict the corresponding normalised fluxes for the permitted M38 and forbidden 6F transition. Figs. 4.6 - 4.12 show a selection of the most outstanding time steps of the calculation which are described in greater details in the following:

- **Maximum until phase  $\phi = 0.38$ :** The calculations show that from maximum visible light up to phase  $\phi = 0.38$  (Fig. 4.6) the shock builds up in the inner  $1 R_*$  and slowly rises through the lowest layers of the atmosphere. No distinct temperature peaks are resulting for these time steps, and as a consequence no Fe II or [Fe II] emission lines are excited.

- **Phase  $\phi = 0.40$  — first emission of Fe II & [Fe II] lines:** As soon as the shock reaches  $r \sim 1.2 R_*$  a high temperature peak of  $T_g^{peak} \sim 8000$  K builds up leading to a sufficient ionised iron density. Consequently, the first emission lines show up (Fig. 4.7).

- **Phase  $\phi = 0.42 - 0.50$  — evolution of Fe II & [Fe II] emission lines:** As the shock moves further outwards the emission lines show a rather complex evolution in flux and profile (Figs. 4.7 - 4.9). The flux varies from high to low values, also the line width constantly varies as well as the line shape. A detailed analysis of the line profiles should be omitted (see Sec. 4.2.4 for details)

- **Phase  $\phi = 0.52 - 0.58$  — dust formation:** At phase  $\phi = 0.52$  one can see that  $\tau_{gr}^{-1}$  becomes positive at  $r \sim 1.5 R_*$ , which means that now dust particles start to grow at these stellar radii caused by the enhanced density due to the shock. In all phases depicted in Fig. 4.10 - 4.11 the dust growth continues and the emission lines for both examined transitions show an obvious decrease in flux, but both lines are still above the

observational limit. The line profile evolve to multicomponent peaks, which are very distinct in the permitted line M38 and in later phases also can be seen in the forbidden line 6F.

- **Phase  $\phi = 0.60 - 0.62$  — noticeable dust condensation:** When dust condensation reaches about 10% at phase  $\phi = 0.60$  (Fig. 4.12, left panels), the lines fluxes of the FeII and [FeII] emission lines are weakened so much that they get close to the observational limit. As dust continues to condense (Fig. 4.12, right panels) and dust condensation reaches about 25%, a next dust shell is formed and the emission lines get fully absorbed.

- **Until the next maximum:** no FeII and [FeII] emission lines can be seen up to the next maximum.

The appearance of the FeII and [FeII] emission lines in these studies show, that the phases of emission in the models ( $\phi_{\text{calc}} = 0.4 - 0.6$ ) are in good agreement with the observed phases of  $\phi_{\text{obs}} = 0.3 - 0.5$ .

Moreover, these calculations point out that there seems to be a correlation to dust formation: these emission lines appear with a difference in phase of  $\Delta\phi \sim 0.1$  before dust formation sets in and in particular can still be seen while the growth of dust grains takes place. The emission of the FeII and [FeII] lines then gets blocked in phases when dust condenses in a noticeable amount and a next dust shell is formed. Hence, the thermodynamical conditions of the innermost dust-forming layers can be probed *during the phase of dust growth, shortly before the formation of a new dust layer*, in particular the *shock which induces the dust formation* in these layers can be analysed in detail with the aid of FeII and [FeII] emission lines as a diagnostic tool.

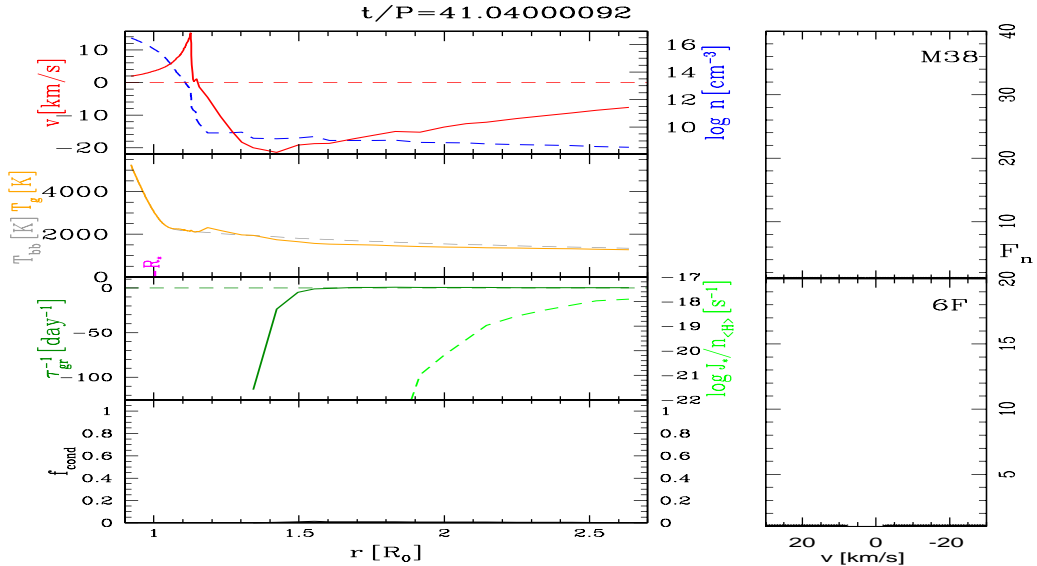


Figure 4.6.: Formation of a shock at  $t/P = 41.04 \equiv \phi = 0.38$ . For explanation of parameters see text.



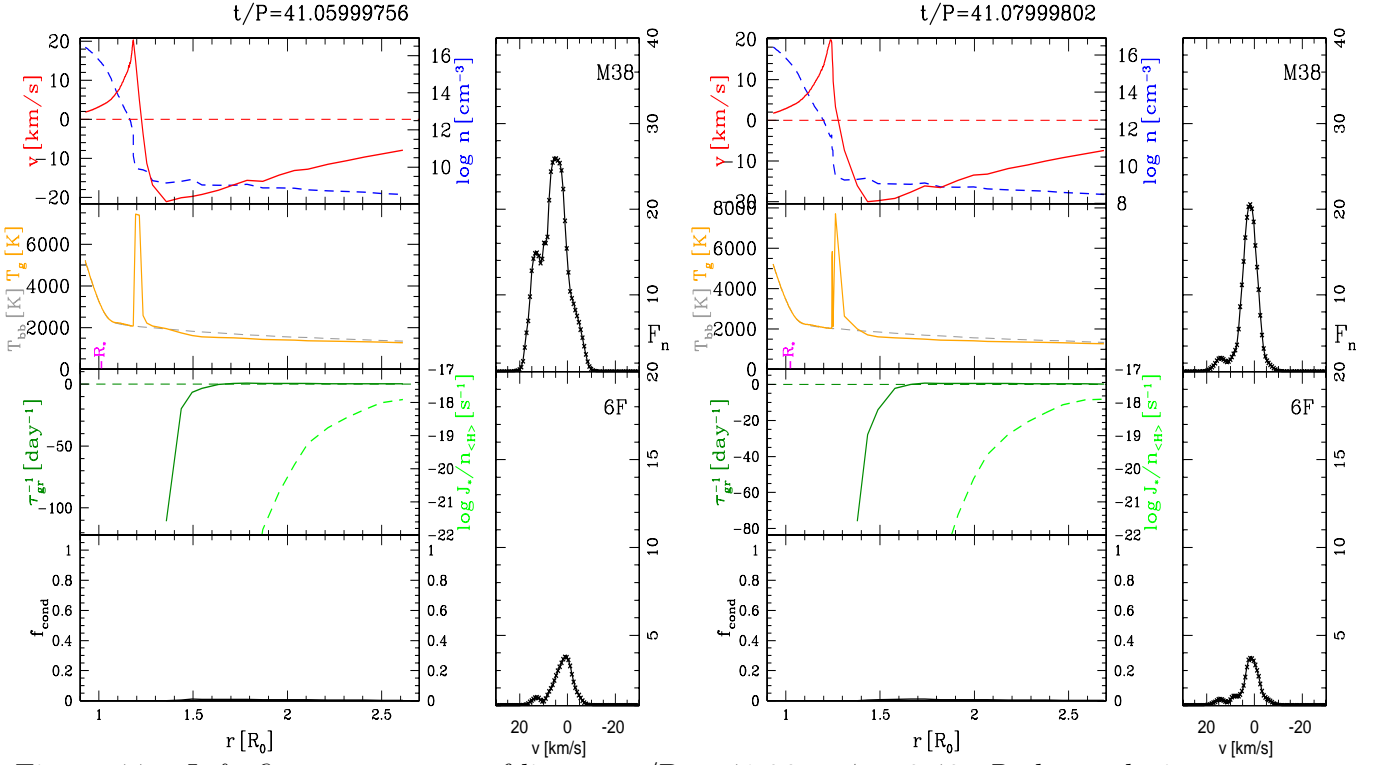


Figure 4.7.: *Left*: first appearance of lines at  $t/P = 41.06 \equiv \phi = 0.40$ . *Right*: evolution of lines at  $t/P = 41.08 \equiv \phi = 0.42$ .

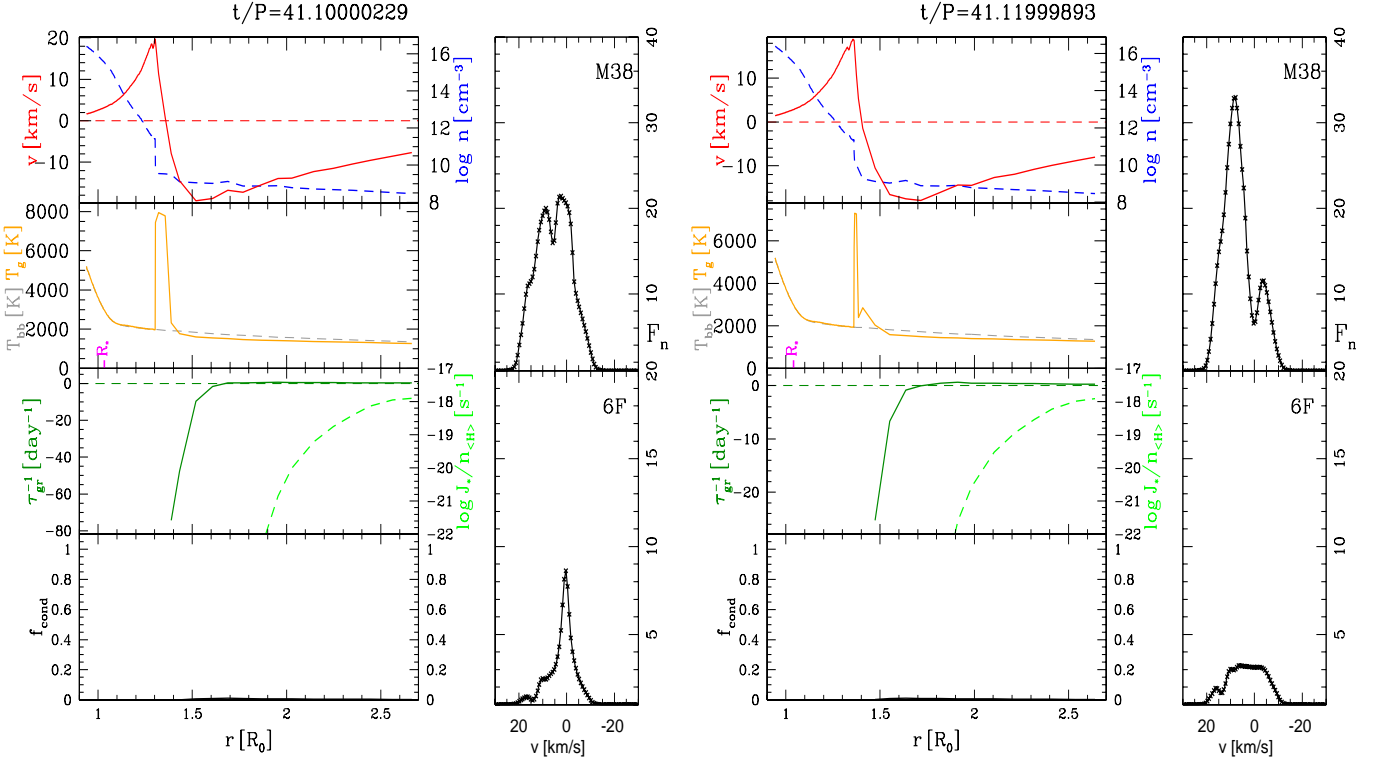
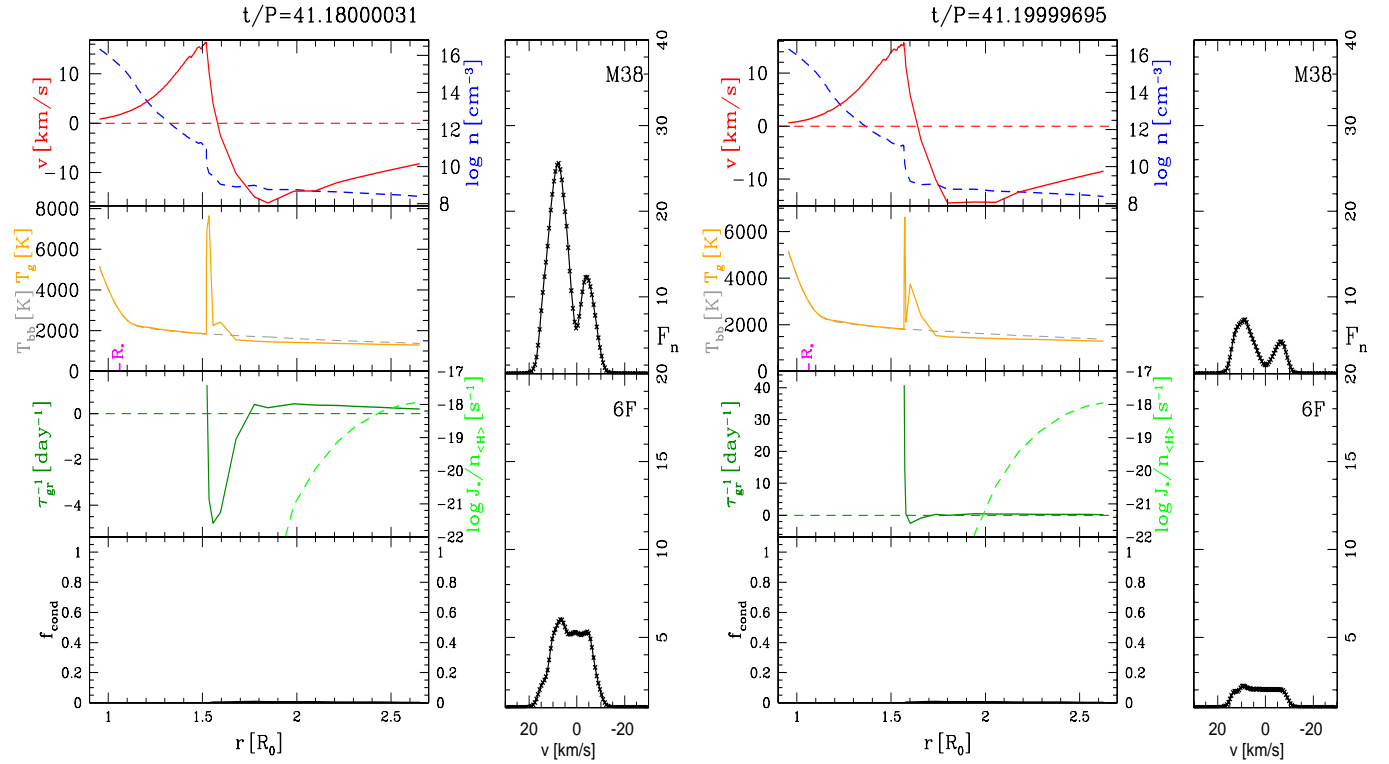
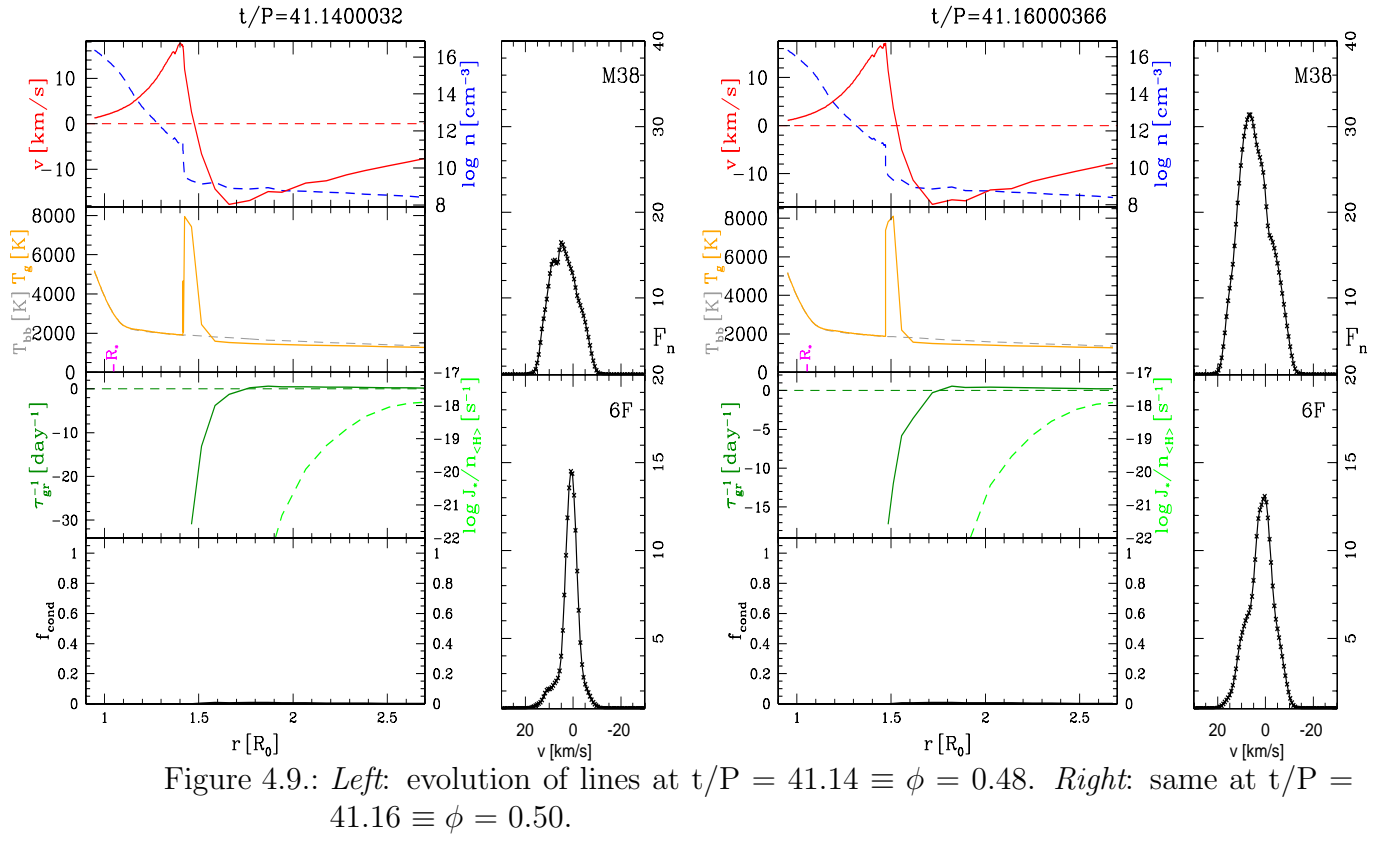


Figure 4.8.: *Left*: evolution of lines at  $t/P = 41.10 \equiv \phi = 0.44$ . *Right*: same at  $t/P = 41.12 \equiv \phi = 0.46$ .



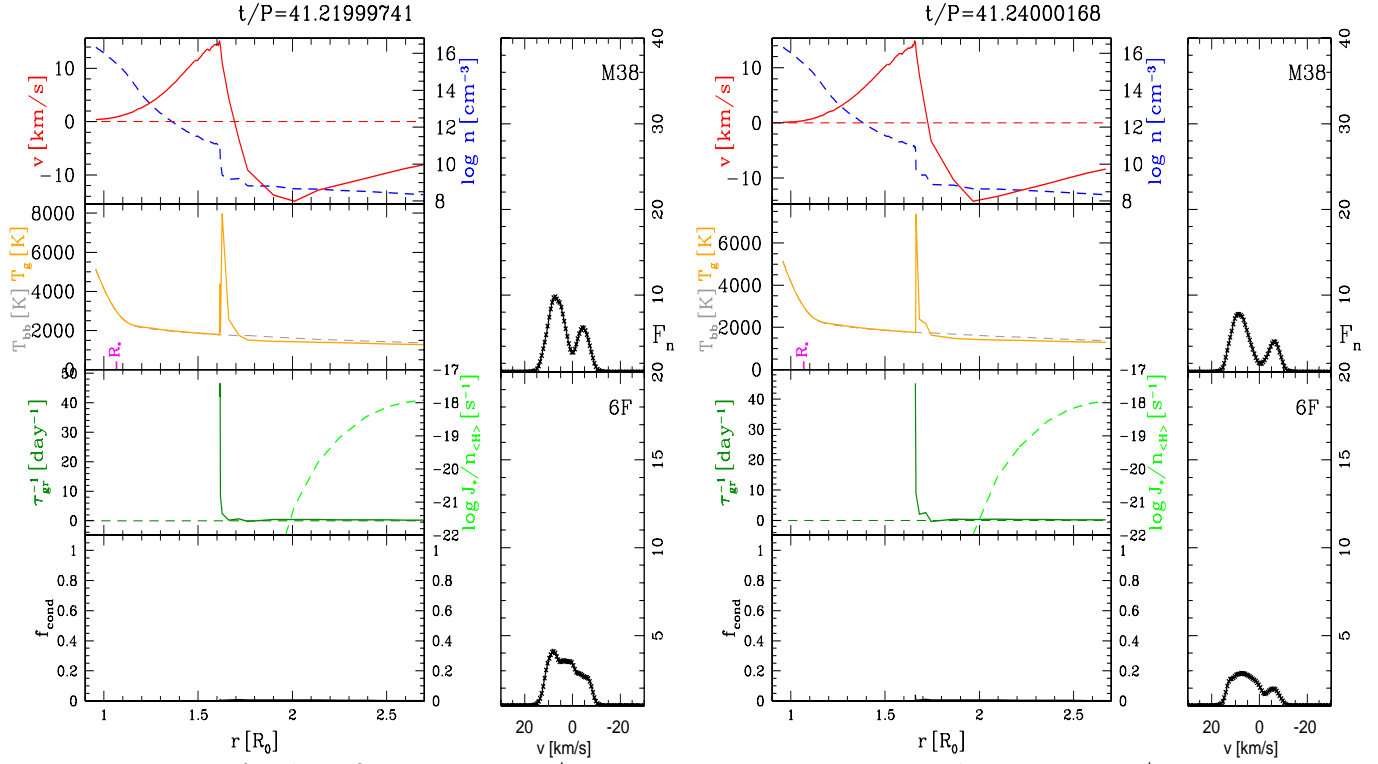


Figure 4.11.: *Left*: dust formation at  $t/P = 41.22 \equiv \phi = 0.56$ . *Right*: same at  $t/P = 41.24 \equiv \phi = 0.58$ .

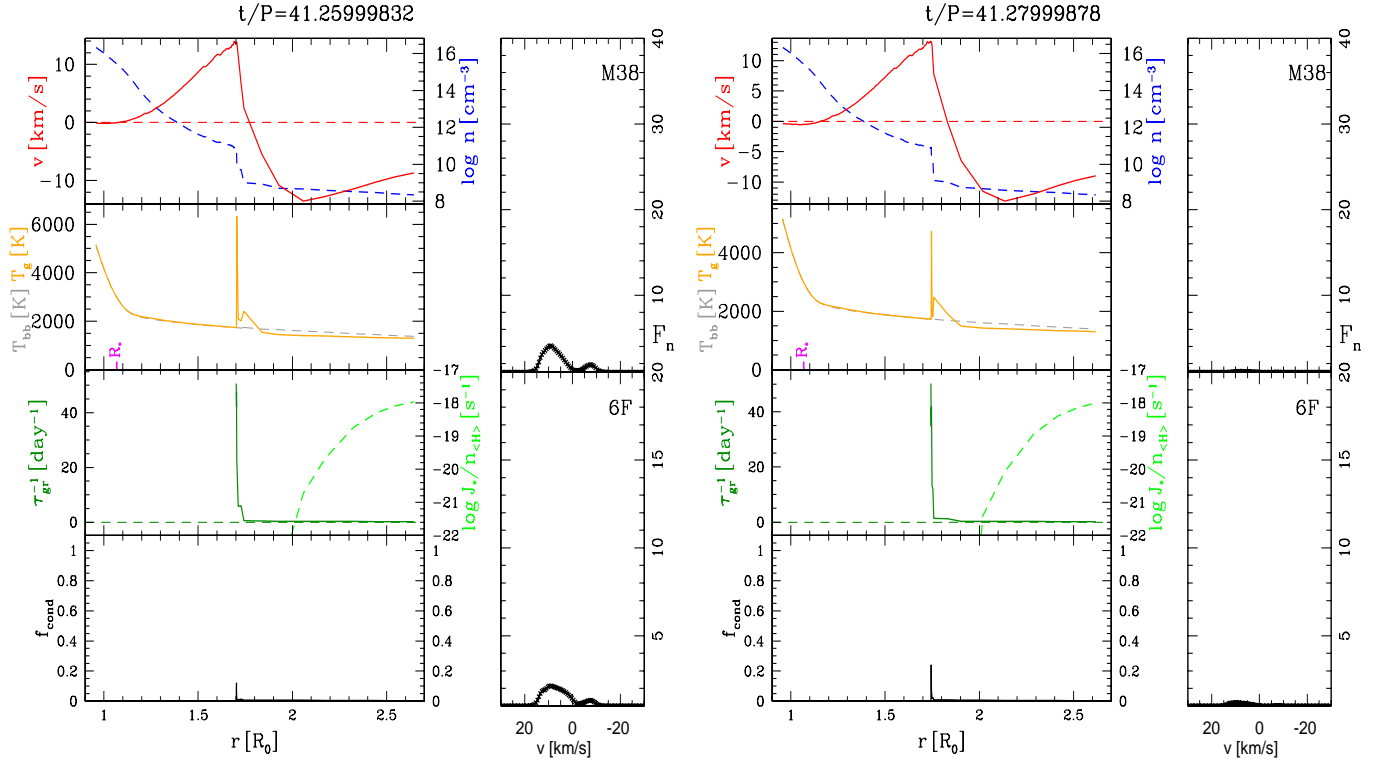


Figure 4.12.: *Left*: noticeable dust condensation at  $t/P = 41.26 \equiv \phi = 0.60$  (minimum). *Right*: dust condensation and formation of the next dust shell at  $t/P = 41.28 \equiv \phi = 0.62$ .

#### 4.2.4. Emission region in the shock front

A detailed comparison of the emission lines presented in Sec. 4.2.3 to the observations also shows some discrepancies. For example, the small line shifts of about  $\sim 2\text{--}10\text{ km s}^{-1}$  in the modelled emission lines (most shifts are near the lower limit) are only close to the observations, where no significant line shifts were noted. Also, the line width measured at FWHM of about  $\sim 10\text{ km s}^{-1}$  are always somewhat smaller than in the observations (line width  $\sim 20\text{ km s}^{-1}$ ). However, the most obvious deviation can be seen in the normalised line fluxes of  $F_n^{\text{peak}} \sim 1\text{--}30$  in the modelled lines and about  $F_n^{\text{peak}} \sim 1\text{--}10$  in the observed emission lines. To analyse these discrepancies it is of interest to examine where these lines are emitted in relation to the shock front.

One important fact of the hydrodynamical calculations which has not been stressed yet is, that these calculations of extended circumstellar shells always contain an artificial viscosity which estimates the dissipative energy input in the shock region. This must be included in order to prevent numerical problems which would be caused by the extreme jumps of the thermodynamical properties in the shock front. One has to be aware, that in regions where the artificial viscosity dominates over the radiative and adiabatic heating respectively cooling functions no physically correct model structures will be achieved. The shock structure gets artificially widened and lowered in temperature, so virtually the sharp shock front gets smeared out. This procedure is justified if the overall structure of the circumstellar shell is of interest, because the details of the shock fronts, which are negligible small compared to the whole shell, do not play an important role.

For the modelling of Fe II emission lines aspired in this work, it is however *essential* to have an exact thermodynamical shock structure, because these lines originate from the shock region. For that, one has to make sure that the emission of these lines comes from regions which are not dominated by the artificial viscosity. To check the region of emission, the components of the emission lines were measured and the according velocity marked in the hydrodynamical structure. Fig. 4.13 shows an example of such an analysis for phase  $\phi = 0.42 \equiv t/p = 41.08$ . As one can see, this simple study already shows that the line forming regions correspond to the zone where the artificial viscosity dominates, as can be seen in the second lowest panel of the left panels in Fig. 4.13. These studies have also been carried out for all occurring emission lines in the calculations, leading to the same results.

Consequently, these input models are inappropriate to model *precise* line fluxes and profiles of the Fe II and [Fe II] lines, because neither the size of the emitting volume nor the gas temperature in the peak is reliable. This sets the necessity for detailed shock structures in order to analyse the exact thermodynamical conditions, which lead to the emission of the Fe II and [Fe II] lines in M-type Mira atmospheres.

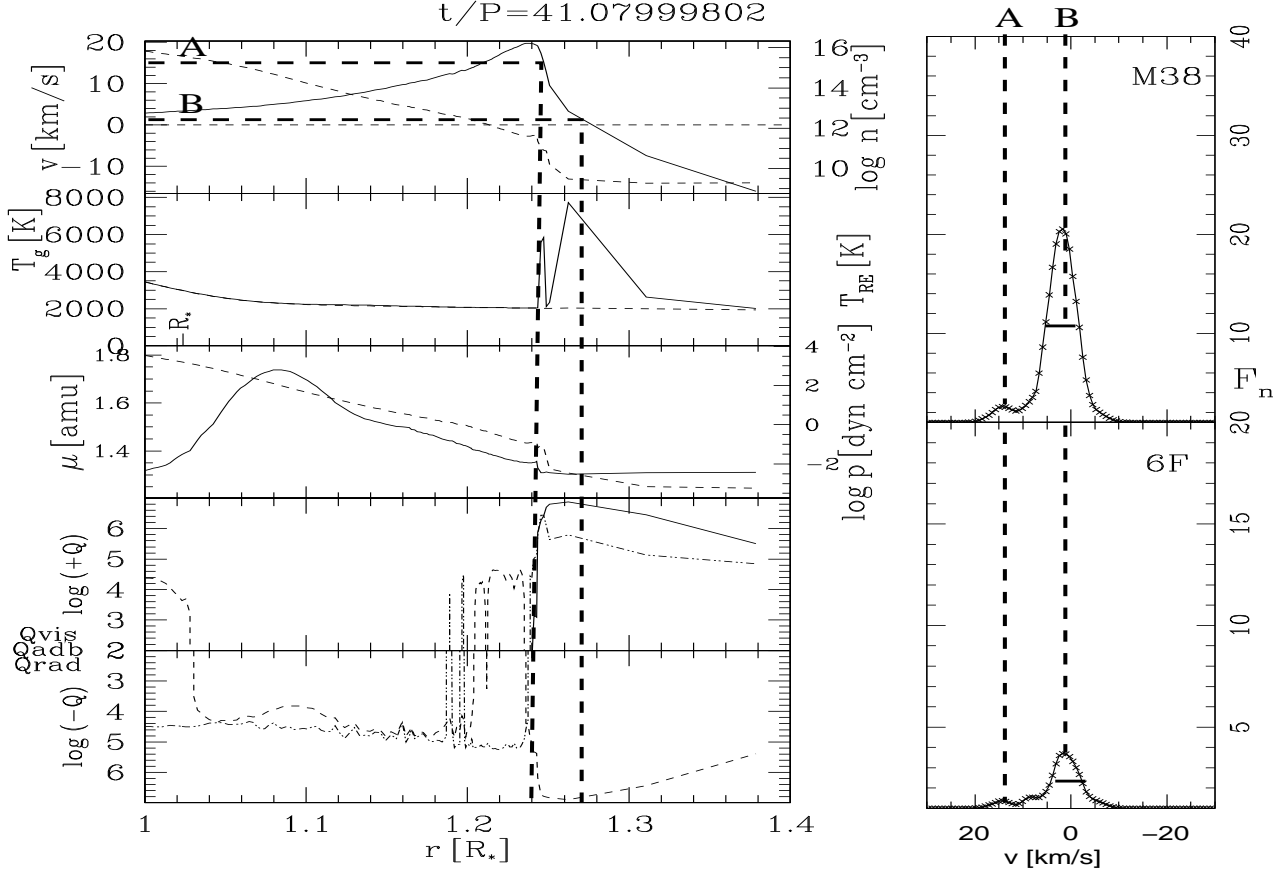


Figure 4.13.: Analysis of the Fe II & [Fe II] line emission region ( $\phi = 0.42 \equiv t/p = 41.08$ ) as marked with the thick dashed lines. *Left*: Parameters are velocity  $v$ , total number density  $n$  (dashed), gas temperature  $T_g$ , radiative equilibrium temperature  $T_{RE}$  ( $= T_{bb}$ ) (dashed), mean molar weight  $\mu$ , gas pressure  $p$  (dashed), NLTE heating (+) and cooling (-) functions with  $Q_{vis}$ : artificial viscosity,  $Q_{adb}$  (dotted-dashed): adiabatic and  $Q_{rad}$  (dashed): radiative contributions. *Right*: normalised line fluxes of the Fe II and [Fe II] lines.

### 4.3. Thermodynamical conditions for Fe II & [Fe II] emission lines

To determine the thermodynamical properties which lead to the formation of the Fe II and [Fe II] emission lines, one obviously needs detailed shock structures with a well resolved zone around the shock front. Such input for an oxygen-rich environment can be obtained from thermodynamical calculations, namely the so called *gas-box* models (Woitke et al. 1996a,b). These detailed shock models can be maintained for oxygen-rich gas compositions, but have the deficiency that they do *not* include dust. The results of Sec. 4.2 already showed that the Fe II and [Fe II] emission lines get emitted in the inner dust free zones before a new opaque dust shell is formed. It therewith is adequate to use the detailed shock structures given by the gas-box calculations for the determination of the accurate thermodynamical conditions in the emitting region.

In order to reproduce the observed normalised peak fluxes of the ionised iron lines, a wide range of models have been constructed with the gas-box calculations. One can in principle vary the 3 parameters in the gas-box calculations: the radial position of the shock front  $R$ , the shock velocity amplitude  $\Delta v$  and the pre-shock density  $\rho_{\text{pre}}$ . Two different parameter studies were carried out, namely a variation of  $\rho_{\text{pre}}$  in a series of models where  $\Delta v$  is specified as a function of  $R$  (Sec. 4.3.2), and a variation of  $\Delta v$  in a series of models where  $\rho_{\text{pre}}$  is specified as a function of  $R$  (Sec. 4.3.3). The approximated relations between  $R$  and  $\Delta v$  as well as  $R$  and  $\rho_{\text{pre}}$  were derived from a reference C-type Mira model by Schirrmacher et al. (2002) (see also Sec. 4.2.2). Note, that the reference model was only used to guide the choice of input parameters for the gas-box models, which were carried out with an *oxygen-rich* composition. The radial structures from these gas-box calculations were used as input models for the detailed NLTE radiative line transfer calculations

The complete procedure for computing Fe II and [Fe II] line fluxes is as follows: (1) choose values for the radius  $R$  of the shock front, the shock velocity amplitude  $\Delta v$  and the pre-shock density  $\rho_{\text{pre}}$ ; (2) iterate the gas-box model to a periodic solution in order to get the thermodynamic properties of the gas ( $T$ ,  $\rho$ , ionisation state, etc.) as a function of radius (or, equivalently, distance behind the shock front); and (3) use the thermodynamic properties from the gas-box model in the NLTE radiative transfer code in order to get the line fluxes and profiles. The normalised peak fluxes  $F_n = F_{\text{line}}^{\text{peak}} / F_{\text{cont}}$  resulting from each model are then sorted into three categories: those within the observed limit  $1.2 < F_n < 10$ , those smaller than the detection limit  $F_n < 1.2$  and those bigger than the observed limit  $F_n > 10$ . Following outstanding regions in the parameter spaces are analysed.

After an outline on the gas-box models in Sec. 4.3.1, the studies of models with varied pre-shock densities are presented in Sec. 4.3.2, which allow to determine the region of Fe II emission in the atmosphere. Here additional calculations with varied shock velocity amplitude have been carried out (Sec. 4.3.2.1), in order to verify the limiting factor for the right emission line fluxes. Some sample models of these investigations are discussed in Sec. 4.3.2.2. Following, studies of models with varied shock velocity amplitude

are presented in Sec. 4.3.3, which reveal suitable pre-shock density and shock velocity amplitude ranges for the emission of Fe II lines. Therewith the full set of thermodynamical shock parameters leading to the emission of Fe II and [Fe II] lines in M-type Mira atmospheres is finally determined.

### 4.3.1. Thermodynamical gas-box models

In the gas-box models the thermodynamical structure of the gas temperature  $T_g(r)$ , radiation temperature  $T_{\text{rad}}(r)$ , density  $\rho(r)$ , velocity  $v(r)$  and particle densities  $n(r)$  are calculated for gas elements (hence the name *gas-box*), which are assumed to move on ballistic trajectories, simulating a periodical shocked atmosphere. For each Lagrangian mass element, the first law of thermodynamics is solved and at each full period, the classical Rankine Hugoniot relations are solved in order to determine the post-shock state from the pre-shock state (determined by the input parameters). The calculations are repeated with fixed pre-shock pressure and velocity until all thermodynamical variations have become periodical. Finally, the radial structure of the shock wave can be reconstructed from the calculated thermodynamic variations in the Lagrangian elements, assuming that the velocity of the shock front is constant (in the Eulerian frame) and that all mass elements undergo the same periodical variations. Hence, the general trend of decreasing pre-shock densities and background radiation fields in the considered small radius interval is neglected.

The calculations strongly depend on the treatment of the state functions and, in particular, on the radiative heating/cooling rate. Here the NLTE heating and cooling functions by Voitke (1996a) are used. A detailed NLTE gas model is set up, in which all particle densities (neutral atoms, molecules, electrons and single ions) and level populations are calculated in statistical equilibrium under the influence of a continuous background radiation field, here a continuous black-body background radiation field. The gas is assumed to be optically thin in the continuum, whereas optical depth effects in spectral lines are accounted for by applying Sobolev theory according to the local mean velocity gradient  $\langle dv/dl \rangle^3$ . The net radiative heating function  $Q_{\text{rad}}$ , defined as the net photon energy exchange rate between radiation field and matter, is determined from the various free-free and bound-free (b-f) transitions, atomic lines and molecular ro-vibrational transitions. The model atoms include several thousand permitted and forbidden lines, and b-f transitions from excited levels (Voitke & Sedlmayr 1999). In addition to the photo-ionisation and direct recombination rates, collisional ionisation from all neutral (ground and excited) levels are included, which affects i. e. the determination of the electron and the Fe II particle densities.

Examples for such detailed shock structures are presented in Sec. 4.3.2.2, where they will be analysed in respect to the resulting Fe II and [Fe II] emission lines.

---

<sup>3</sup>Here a fixed value of  $\langle dv/dl \rangle = 10^{-7} \text{ s}^{-1}$  is used, a typical value for the saw-tooth like velocity fields encountered in the shocked envelopes of Mira stars.

### 4.3.2. Variation of $\rho_{\text{pre}}$

For a variety of fixed pairs of  $R$  and  $\Delta v$  the pre-shock density  $\rho_{\text{pre}}$  was varied, resulting in about 750 gas-box models. Fig. 4.14 depicts a parameter study up to  $5 R_*$  with intermediate shock amplitudes (additional parameter studies for  $5 - 10 R_*$  with  $\Delta v < 18 \text{ km s}^{-1}$  result in normalised peak fluxes which are too small so they are not depicted here). The normalised peak fluxes  $F_n = F_{\text{line}}^{\text{peak}} / F_{\text{cont}}$  resulting from each model are colour coded as follows: fluxes within the observed limit  $1.2 < F_n < 10$  are marked with green lines, those smaller than the detection limit  $F_n < 1.2$  with red lines and those bigger than the observed limit  $F_n > 10$  are indicated with blue lines. Also marked with a dotted-dashed line in Fig. 4.14 is a relation between pre-shock density and shock position, which was derived from the model by Schirrmacher et al. (2002), to give a reference for the expected parameter range of  $\rho_{\text{pre}}$  in a Mira atmosphere.

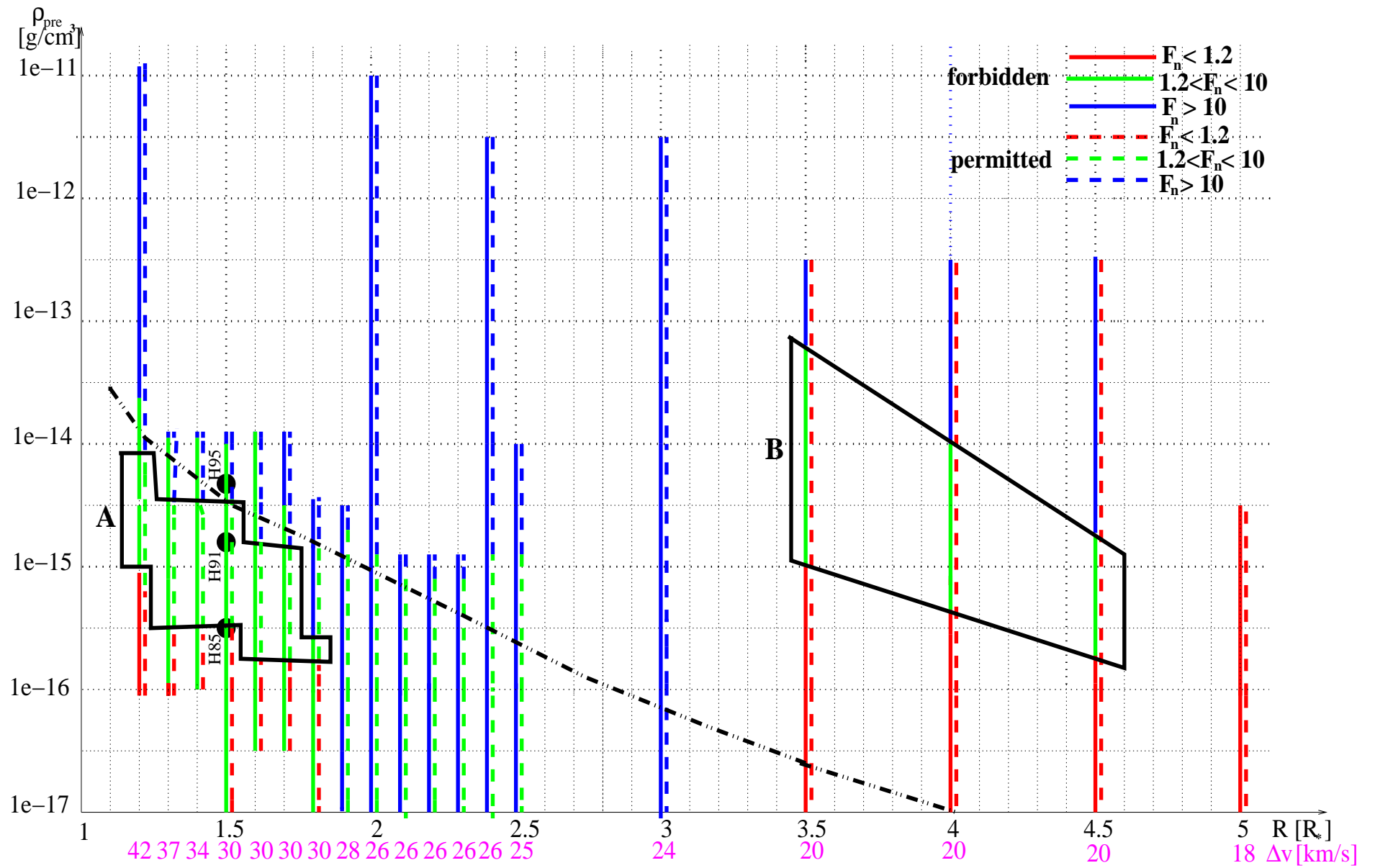
The results of these studies show, that the normalised line fluxes of the forbidden and the permitted line are both within the observed limits close to the star  $R = 1 - 2.5 R_*$  (Fig. 4.14, green lines) whereas the normalised peak fluxes are much too small in the regions  $R = 3.5 - 5 R_*$  (Fig. 4.14, red lines). For models with  $\rho_{\text{pre}} > 10^{-14} \text{ g cm}^{-3}$  the normalised peak fluxes of the Fe II lines turn out to be too large (Fig. 4.14, blue lines). These pre-shock densities are larger than the derived radial pre-shock densities resulting from the reference model. Two especially outstanding domains can be seen:

- **Region A:** A remarkable result is that there exists *only one domain*, namely region A, where the normalised peak flux of both calculated permitted and forbidden lines fit the observed fluxes. This region is close to the star's photosphere at  $R = 1.2 - 1.8 R_*$  and the densities therein correspond to our reference model in the upper limit, respectively being one order of magnitude smaller for the lower limit of region A. Additionally, *region A fits the approximated position of the shock-front  $R$  around phase  $\phi \sim 0.3 - 0.5$ .*

- **Region B:** In this region at about  $R = 3.5 - 4.5 R_*$  the forbidden line fits the observed limits, but the permitted line is below the detection limit. As both lines were always observed simultaneously, this finding does not correspond to our observations. The pre-shock density in region B is too high according to our reference model ( $\sim 1.5 - 3$  orders of magnitude higher). In addition, these lines could only be emitted from a shock  $\sim 1.5$  cycles old (i.e. from the previous pulsation cycle) since even an extreme shock with velocity  $v_s = 40 \text{ km s}^{-1}$  could at most reach  $R = 3 R_*$  around phase  $\phi = 0.5$ . However a shock with  $v_s = 10 \text{ km s}^{-1}$  could reach  $R = 3.5 R_*$  at  $\phi = 1.5$ .

Further detailed examinations of all gas-box models in region A have revealed the essential result, that in those models the Fe II ion densities are in the range of  $n_{\text{FeII}} \sim 10^5 - 10^{5.5} \text{ cm}^{-3}$  in the hot post-shock region. Higher (lower) ion densities generate normalised peak fluxes that are too large (small). *Hence, the ionised iron density is the most important factor determining the calculated normalised peak fluxes.* These results lead to the important conclusion that the Fe II emission lines can only *originate from the hot post-shock region*, where  $n_{\text{FeII}} \sim 10^5 - 10^{5.5} \text{ cm}^{-3}$ . The cooler post-shock regions do not contribute to the calculated fluxes.





37

Figure 4.14.: Parameter study for the normalised peak line fluxes of the forbidden transition [FeII] 6F (solid lines) and permitted transition FeII M38 (dashed lines). Models were constructed with a range of  $\rho_{\text{pre}}$  for each fixed  $R$  and  $\Delta v$  pair ( $R$ : the radial distance of the shock from the centre of the star,  $\Delta v$  shock velocity amplitude), which are marked on the x-axis. Dotted-dashed line: reference model by Schirrmacher et al. (2002). For explanation of the colour coding and region A and B see text. Bullets mark models shown in Fig. 4.16.

#### 4.3.2.1. The effect of $\Delta v$ on Region A

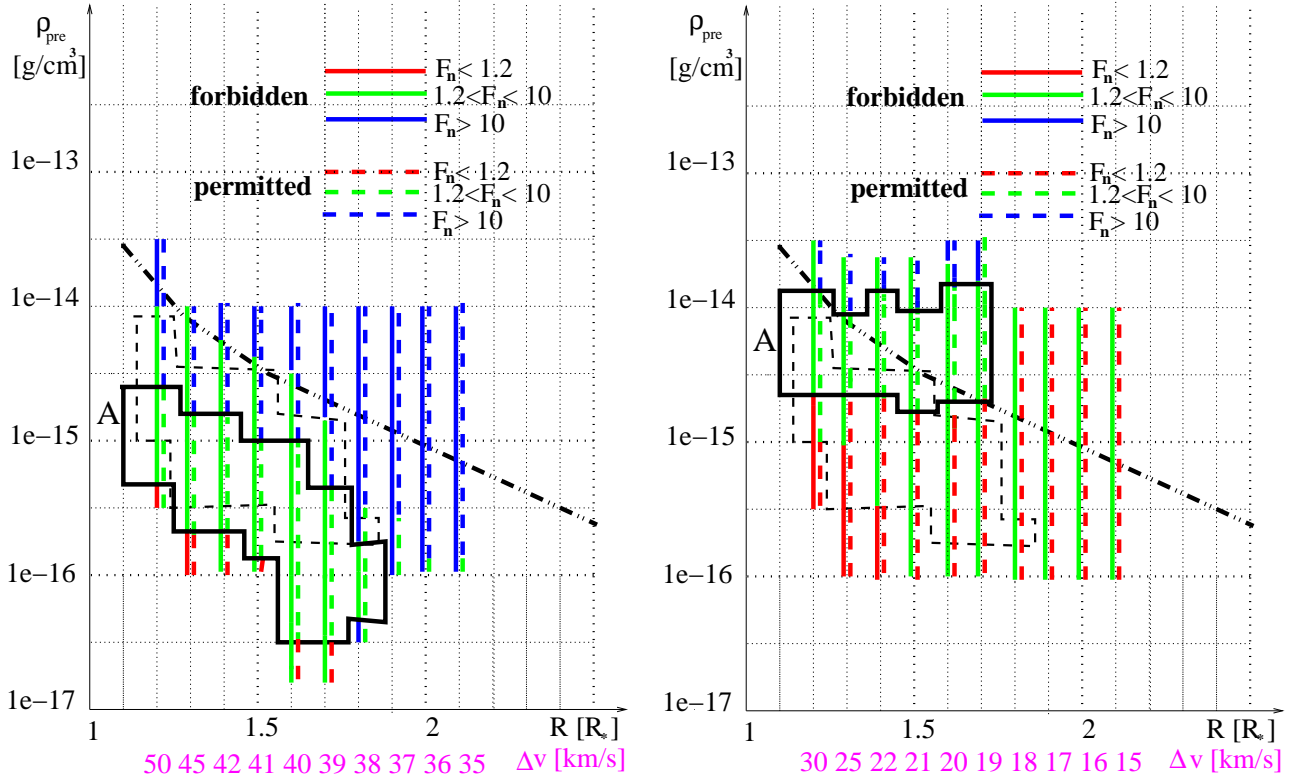


Figure 4.15.: Variation of the shock velocity amplitude in the interval  $1-2.1 R_*$ . Previous position of region A is marked with a dashed box. *Left*: Higher and *right*: lower  $\Delta v$  than in Fig. 4.14.

Additionally, the influence of different shock velocity amplitudes in the models has been investigated in order to study how the position of region A changes. The same pre-shock densities as in Sec. 4.3.2 have been assumed and models with varied velocity amplitudes of the shock wave in the interval  $1 - 2.1 R_*$  (about 200 models for each study) have been calculated.

The investigations show that *higher* shock velocity amplitudes shift region A towards *lower* pre-shock densities (left panel in Fig. 3) and *lower* velocities cause a shift towards *higher* densities (right panel in Fig. 4.15). It can also be noted, that the details of the shape of region A are slightly changed: For lower shock velocity amplitudes the region is located around  $\rho_{\text{pre}} \sim 10^{-14} \text{ g cm}^{-3}$ , whereas it is more spread out for higher shock velocity amplitudes from  $\rho_{\text{pre}} \sim 10^{-14.5}$  to  $10^{-16.5} \text{ g cm}^{-3}$ . Generally, *no shift* in the radial distance of region A results.

A detailed examination of the models again confirms that an ion density in the gas-box models of about  $n_{\text{FeII}} \sim 10^5 - 10^{5.5} \text{ cm}^{-3}$  is required in models that reproduce the observed forbidden and permitted line fluxes.

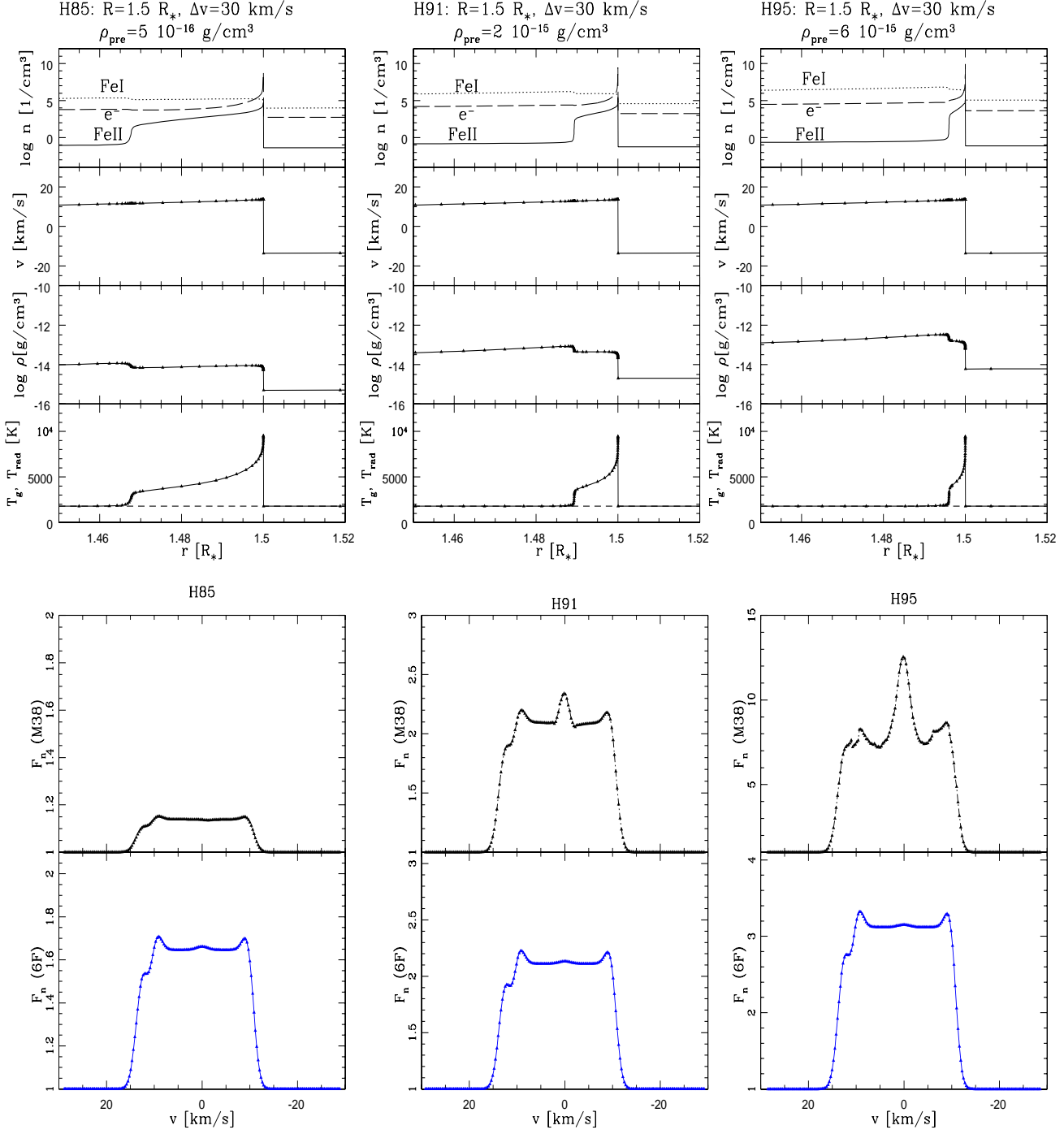


Figure 4.16.: Three models from Region A (bullets in Fig. 4.14) ordered from left to right by increasing pre-shock density. *Upper row:* gas-box shock models: particle densities  $n(r)$  of Fe II, Fe I and electrons; radial velocity  $v(r)$ ; density  $\rho(r)$ ; gas temperature  $T_g(r)$  and radiation temperature  $T_{\text{rad}}(r)$  (dashed). *Lower row:* resulting NLTE line fluxes in units of normalised flux  $F_n$ : permitted M38 transition (upper panels), forbidden 6F transition (lower panels).

#### 4.3.2.2. Sample models

Several models marked around region A in Fig. 4.14 are depicted in Fig. 4.16. These models cover the full range of observed fluxes. As noted in the two previous sections, it was found that  $n_{\text{FeII}}$  is the limiting factor for the line fluxes, so in the following those variables should be outlined that influence the particle density of Fe II.

The upper panels of Fig. 4.16 show the corresponding gas-box models for a  $\Delta v = 30 \text{ km s}^{-1}$  shock wave at  $R = 1.5 R_*$  approaching pre-shock densities of  $5 \cdot 10^{-16}$ ,  $2 \cdot 10^{-15}$  and  $6 \cdot 10^{-15} \text{ g cm}^{-3}$ . According to the model, the Fe II densities clearly follow the temporal evolution of the temperature. This strong correlation demonstrates the importance of the collisional ionisation processes (note, however, that the photo-ionisation of Fe is not considered in any “radiative precursor” due to UV radiation emergent from the shock wave itself, see e. g. Huguet et al. 1992). In the shock model, the formation of Fe II lines is clearly restricted to the high-temperature regions behind the shock waves.

The post-shock (“peak”) temperature is determined from the amount of mechanical energy dissipated by the shock wave and the pre-shock state, using the Rankine-Hugoniot relations and the assumption of statistical equilibrium. If the pre-shock gas is  $\text{H}_2$ -rich, only shock waves with velocities  $\geq 20 \text{ km s}^{-1}$  are able to completely dissociate the  $\text{H}_2$  molecules. The surplus mechanical energy is converted into thermal kinetic energy, leading easily to post shock temperatures of the order of  $\approx 8000\text{--}11000 \text{ K}$ . At these temperatures, the H atoms are ionised (mainly collisionally) which again consumes a lot of the dissipated energy. Behind the shock front, the gas cools via radiative cooling in two phases. First mainly the hydrogen b-f transitions,  $\text{Ly}\alpha$  and  $\text{H}\alpha$  as well as  $\text{Ca II H} + \text{K}$  and  $\text{Mg II h} + \text{k}$  lead to a quick temperature decrease down to about  $5000\text{--}6000 \text{ K}$  within a very narrow region behind the shock (not resolved in Fig. 4). Then permitted lines can no longer be excited collisionally and low-lying energy levels of certain forbidden and fine-structure lines, in particular of Fe I and Fe II, take over and the radiative cooling slowly continues (Woitke & Sedlmayr 1999) until temperatures appropriate for molecule formation are reached. Once the first molecules are present in the gas phase, the large amount of permitted ro-vibrational lines of polar molecules, in particular CO, causes a substantial re-increase of the radiative cooling rate and finally results in a fast relaxation towards radiative equilibrium.

The radial extent of the complete radiative post-shock zone amounts to  $\sim 0.035 R_*$ ,  $\sim 0.01 R_*$  and  $\sim 0.005 R_*$  for pre-shock densities  $5 \cdot 10^{-16} \text{ g cm}^{-3}$  (H85),  $2 \cdot 10^{-15} \text{ g cm}^{-3}$  (H91) and  $6 \cdot 10^{-15} \text{ g cm}^{-3}$  (H95), respectively — a consequence of the general trend of increasing radiative cooling rates per unit mass with increasing densities.

In summary, Fe II emission lines are expected to occur if the velocity is  $\geq 20 \text{ km s}^{-1}$  (“dissociative shock”) or if the pre-shock state is  $\text{H}_2$ -poor.

### 4.3.3. Variation of $\Delta v$

The previously presented models have shown that there is only a limited *spatial region* in Mira atmospheres where the appropriate Fe II and [Fe II] emission line fluxes can be formed via shocks. It was also found that all models that successfully reproduced observational fluxes have  $n_{\text{FeII}} \sim 10^5 - 10^{5.5} \text{ cm}^{-3}$ . However, these models considered a fairly restricted range of shock velocity amplitude  $\Delta v$ , guided by examination of reference hydrodynamical models. Here, the main aim is to vary  $\Delta v$  in order to determine the full unconstrained range of shock velocity amplitude, as well as the pre-shock density, which lead to the formation of the Fe II and [Fe II] emission lines of the observed strength.

For these studies about 450 gas-box models have been calculated for different pre-shock densities  $\rho_{\text{pre}}$  and shock velocity amplitudes  $\Delta v$ , where now  $R$  is related to  $\rho_{\text{pre}}$  according to the model of Schirrmacher et al. (2002). The results are presented in Fig. 4.17, where the same colour coding like in Fig. 4.14 has been applied. Marked with small rectangles are domains where the radiative transfer code did not converge and circles mark the domains where the gas-box calculations failed. The dashed-dotted box at  $\rho_{\text{pre}} = 7 \cdot 10^{-17} - 1 \cdot 10^{-18} \text{ g cm}^{-3}$  denotes a domain where the relaxation towards radiative equilibrium (RE) in the gas-box models remains incomplete. For such small pre-shock gas densities, the gas cannot radiate away the excess energy dissipated by a shock wave within one period (in particular the molecular cooling is not sufficient to radiate away the energy liberated by the  $\text{H}_2$  re-formation) before the next shock wave encounters the gas element. In this case, the pre-shock temperature is higher and the pre-shock density lower than in RE (the pre-shock pressure is considered as fixed here).

An examination of Fig. 4.17 shows that shocks with low velocity amplitudes  $\Delta v < 15 \text{ km s}^{-1}$ , as well as extremely high shock velocity amplitudes  $\Delta v \sim 60 \text{ km s}^{-1}$  at  $\rho_{\text{pre}} = 1 \cdot 10^{-16} - 2 \cdot 10^{-18} \text{ g cm}^{-3}$  lead to normalised line fluxes which are too small (Fig. 4.17, red lines). There exists an intermediate shock amplitude domain from roughly  $\Delta v \sim 30 - 45 \text{ km s}^{-1}$  and  $\rho_{\text{pre}} = 3 \cdot 10^{-15} - 3 \cdot 10^{-18} \text{ g cm}^{-3}$  where all normalised peak fluxes turn out to be too large (Fig. 4.17, blue lines). However, there are two in particular interesting, extended domains: (1) at high shock velocities  $\Delta v = 50 - 60 \text{ km s}^{-1}$  over the whole investigated  $\rho_{\text{pre}}$ -span (here the shocks are capable of dissociating *and* ionising the gas completely, leading to extremely high post-shock temperatures) and (2) at lower shock velocities  $\Delta v = 20 - 30 \text{ km s}^{-1}$  and  $\rho_{\text{pre}} \sim 4 \cdot 10^{-14} - 3 \cdot 10^{-15} \text{ g cm}^{-3}$  where both normalised peak fluxes of the permitted and forbidden Fe II emission lines fit the observed data (Fig. 4.17, green lines).

A detailed examination of these regions is necessary, because although the fluxes might fit the observed normalised peak line fluxes, the line profiles appear to be very different. Fig. 4.18 depicts selected models as marked by the bullets in Fig. 4.17 and the resulting Fe II and [Fe II] emission lines. Here one can already note that in all of the regions marked with **B** (B1, B2, B3, B4, B5, B5 and B6) multicomponent profiles appear as a result of the radiative transfer calculations (see model VR39 Fig. 4.18, left panels). These kind of profiles do not show any similarity to the observed single-peaked, gauss-like profiles (Richter & Wood 2001).

The only regions with appropriate normalised peak fluxes *and* single line profiles are the ones marked with **A** (A1, A2, A3) in Fig. 4.17. Although the profiles are not perfectly fitting up to this stage, there is a general trend towards the gauss-like observed profiles in the named regions, at least for the permitted lines (the forbidden lines tend to have square profiles as expected from unobscured shell emission).

Concerning region A3, it is unlikely that high shock amplitudes of  $60 \text{ km s}^{-1}$  occur at  $R \sim 6 R_*$  ( $\rho_{pre} = 1 \cdot 10^{-18} \text{ g cm}^{-3}$ ). The hydrodynamical calculation by Schirrmacher et al. (2002) show, that the shock velocity amplitude  $\Delta v$  is large in the innermost  $1-4 R_*$  and decreases as the shock moves further outwards. Another argument against this region is that the emission lines could only be emitted from this region by a shock from the previous pulsation cycle (see explanation given for region B in Sec. 4.3.3).

This leaves us with only two possible regions, which are A1 and A2. There is a markable difference in the shape of the profiles in these regions, namely that the gauss-like profiles have different widths: in region A2 the profiles are wider (Fig. 4.18, right panels) whereas in region A1 the profiles look similar to the ones in our previous study (Fig. 4.18, middle panel).

Analysis of the peak line ratio  $F_{M38}/F_{6F}$  provides an additional constraint. Most of the models in region A1 give a ratio  $\sim 1$ , as resulting from the observations (see also appendix A), whereas in region A2 the peak line ratios are always significantly higher at about  $F_{M38}/F_{6F} \sim 3$ . *This strongly suggests that region A1 is the only region fitting our observed Fe II and [Fe II] emission peak line fluxes.*

To summarise, a limited parameter range in the  $\rho_{pre}, \Delta v$  space has been found which leads to the formation of the observed Fe II and [Fe II] peak line fluxes and line ratios, as well as gauss-like profiles. It can therewith be concluded that pre-shock densities of  $\rho_{pre} = 3 \cdot 10^{-15} - 4 \cdot 10^{-14} \text{ g cm}^{-3}$  and shock amplitude velocities of  $\Delta v = 20 - 30 \text{ km s}^{-1}$ , are needed to lead to the observed Fe II emission lines. According to the reference model of Schirrmacher et al. (2002) such thermodynamical conditions can exist at a radial distance of the shock  $R = 1.1 - 1.8 R_*$ .

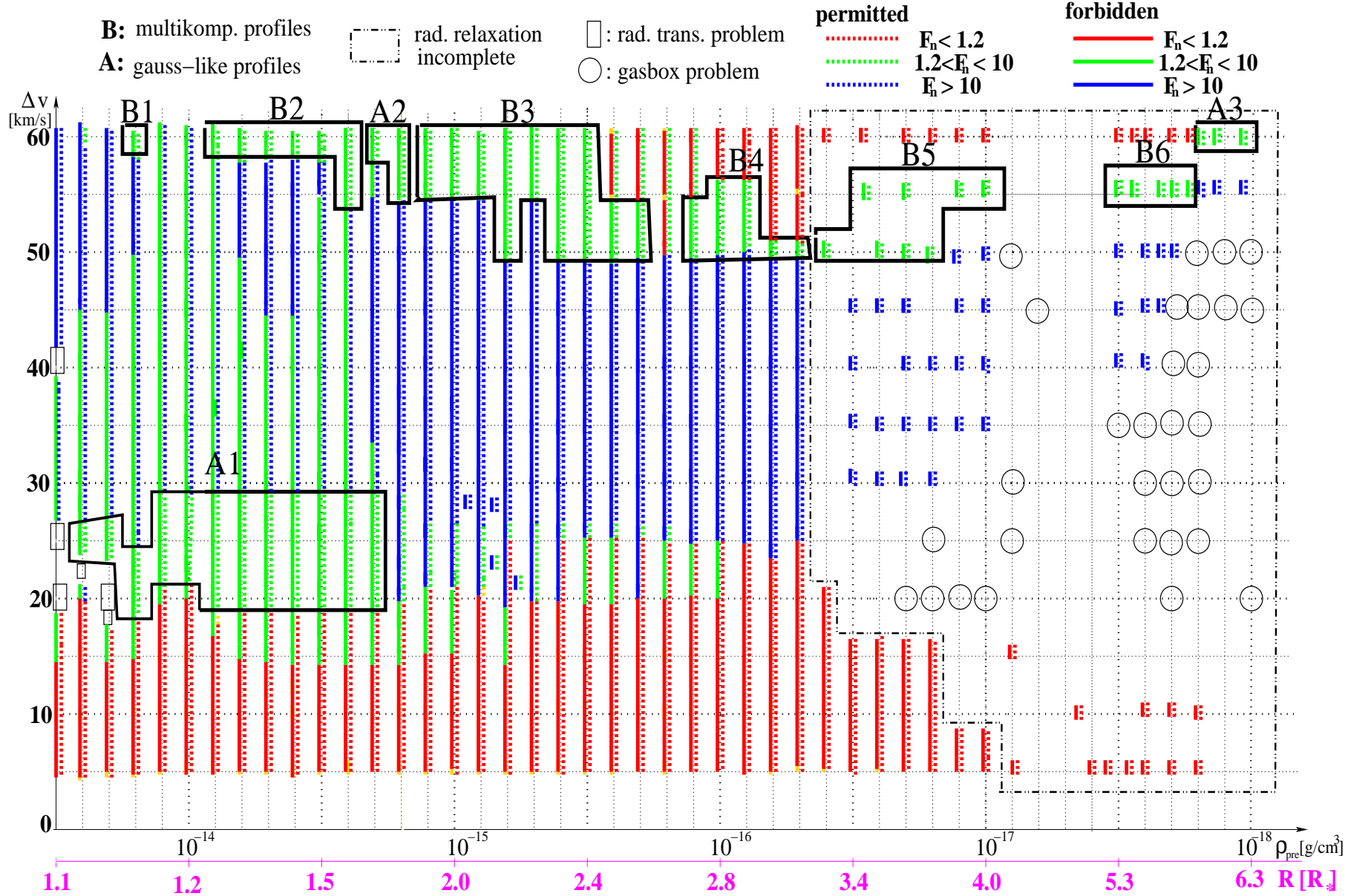


Figure 4.17.: Similar to Fig. 4.14 but for models where  $\Delta v$  varies for fixed  $\rho_{\text{pre}}$ ,  $R$  pairs. Thin rectangles mark domains where the radiative transfer calculations failed to converge and circles mark the like where the gas-box calculations failed. A whole region where the relaxation of the gas-box models towards radiative equilibrium remains incomplete is marked with a dashed-dotted box. Bullets mark models which are depicted in Fig. 4.18. For explanation of the marked regions A1-A3 and B1-B6 see text.

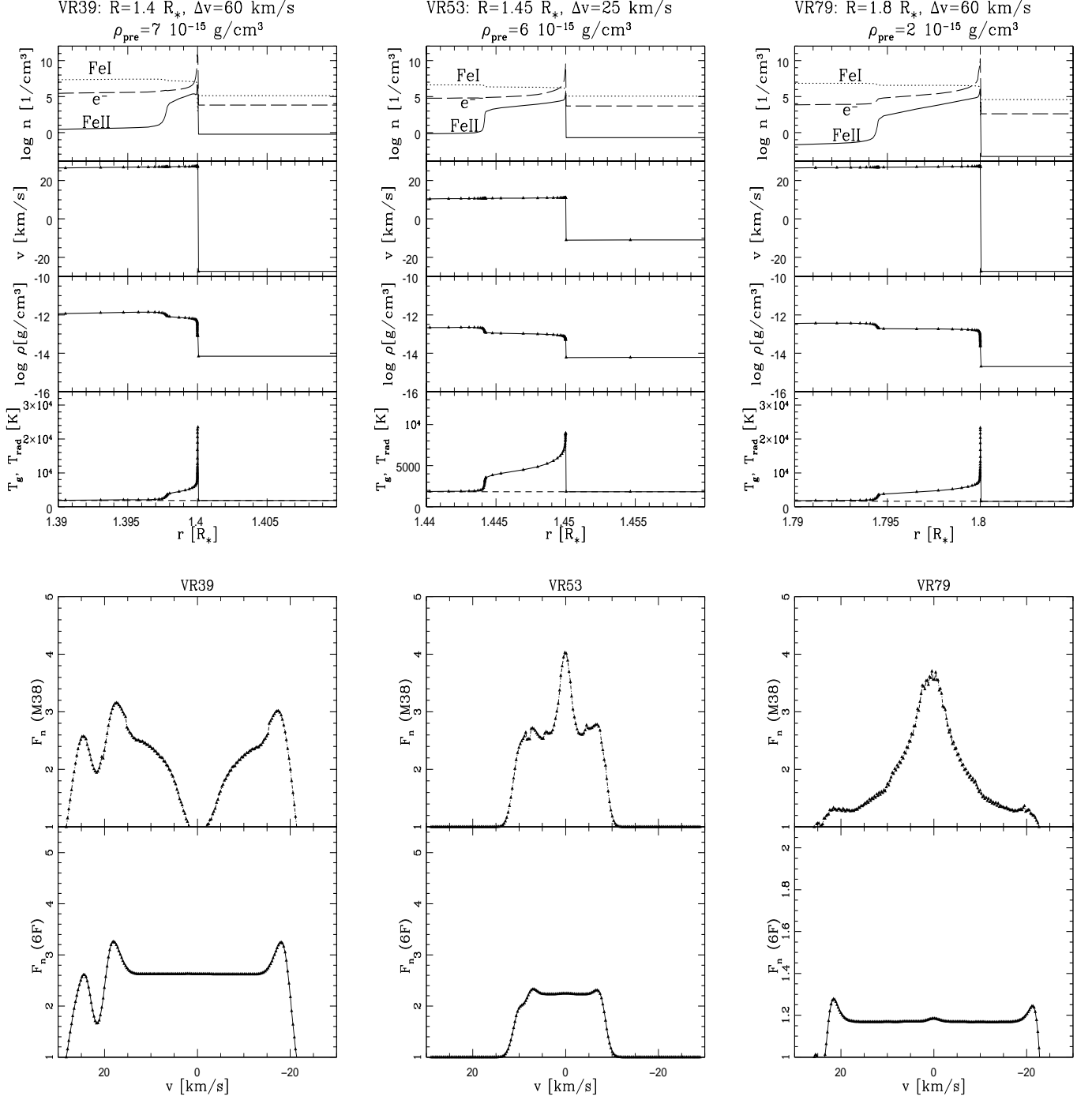


Figure 4.18.: From left to right: models from Regions B3, A1 and A2 (bullets in Fig. 4.17) *Upper row*: gas-box shock models: particle densities  $n(r)$  of Fe II, Fe I and electrons; radial velocity  $v(r)$ ; density  $\rho(r)$ ; gas temperature  $T_g(r)$  and radiation temperature  $T_{\text{rad}}(r)$  (dashed). *Lower row*: resulting NLTE line fluxes in units of normalised flux  $F_n$ : permitted M38 transition (upper panels), forbidden 6F transition (lower panels).



## 4.4. Summary

The various studies presented in this section confirm, that Fe II and [Fe II] emission lines can in fact be used as diagnostic tools to probe the inner dust-producing layers of M-type Mira atmospheres. Moreover, in this work the Fe II and [Fe II] emission lines have for the first time been *applied* as diagnostic tools to determine the thermodynamical properties of the emitting regions.

The first studies (Sec. 4.1) already prove that stationary wind models cannot explain the emission of these lines, whereas models with high artificial temperature peaks inserted in the models show, that such temperature peaks are essential to form Fe II and [Fe II] emission lines. Thus, these results point out that shock waves must be the cause for these emission lines.

Following, models of extended, shocked C-type Mira atmospheres have been studied, which include dust formation and evaporation in a self-consistent way (Sec. 4.2). The outcome of these studies show, that firstly only models with high temperature peaks resulting from the use of NLTE radiative cooling functions can explain the emission of the Fe II and [Fe II] lines. Secondly, a calculation of a time series of such models also reveals the correlation between dust formation and the emission of Fe II and [Fe II] lines: They appear in good agreement with the observations at  $\Delta\phi \sim 0.1$  before dust formation begins in the models and can still be seen while the growth of dust grains takes place. Hence, these lines are an excellent diagnostic tool to analyse the thermodynamical properties of the shock which induces dust formation in the inner regions of the atmosphere, shortly before the formation of a new dust layer. However, for studies of the thermodynamical conditions which lead to the formation of the Fe II and [Fe II] emission lines, it was found that these model structures are not detailed enough.

Consequently, dust-free thermodynamic models of periodic shock waves have been used in order to obtain detailed shock structures (Sec. 4.3). A series of detailed NLTE radiative transfer calculations performed on such models reveal that there exists only one region (Region A) close to the star's photosphere at  $1.2 - 1.8 R_*$  where the normalised peak fluxes of both the permitted and the forbidden Fe II emission line fit the observational limits. The radial position of this region corresponds to the region estimated from the observational fact that the Fe II and [Fe II] emission lines appear about half a pulsation cycle after the shock emerges from the photosphere.

Also, the variation of region A with velocity amplitude of the shock wave has been investigated and yields that higher (lower) velocities lead to the formation of the observed normalised peak fluxes at lower (higher) pre-shock densities.

It was found that the ion density of Fe II is the crucial factor for the peak fluxes, and deduced that the Fe II emission lines can only originate from the hot post-shock region, where the Fe II density can reach  $n_{\text{FeII}} \sim 10^5 - 10^{5.5} \text{ cm}^{-3}$ .

The limited parameter range to produce the observed normalised peak fluxes has therewith been determined: pre-shock densities of  $\rho_{\text{pre}} = 3 \cdot 10^{-15} - 4 \cdot 10^{-14} \text{ g cm}^{-3}$  and shock amplitude velocities of  $\Delta v = 20 - 30 \text{ km s}^{-1}$ . According to the hydrodynamical

reference model of Schirrmacher (2002) these parameter combinations exist in shocks at  $R = 1.1 - 1.8 R_*$ .

Additionally, the fact that the FeII and [Fe II] emission lines occur only following a bright maximum in the observations points out that these emission lines are presumably produced by a stronger-than-normal shock. This implicates, that the absence of Fe II and [Fe II] emission lines in most pulsation cycles is most likely due to the shock velocity  $\Delta v$  at  $1.1 - 1.8 R_*$  *being less than* the limit of  $\sim 20 \text{ km s}^{-1}$  which our NLTE radiative transfer models require. This perhaps indicates that current hydrodynamical models such as the reference model, which lead us to predict Fe II and [Fe II] emission lines in every cycle, have shock velocities larger than those in real Miras. In that case, the current hydrodynamical models probably overestimate mass loss rates. Improved modelling of the shock waves and the NLTE radiative transfer in the post-shock region of Miras is required to confirm these suggestions.

## 5. Conclusions & Outlook

The Fe II and [Fe II] emission lines in M-type Mira variables have been known for almost 60 years, but they have so far never been modelled in order to reveal the valuable information they contain about the complex hydro- and thermodynamical conditions of these pulsating variable stars. The extensive studies of these emission lines in M-type Mira variables presented in this work have build a bridging between high-resolution observations and self-consistent hydro- and thermodynamical models with the aid of detailed NLTE radiative line transfer calculations. Therewith, it has been shown that these emission lines can be utilised as a diagnostic tool to determine the thermodynamical conditions near the dust-forming zones in M-type Miras, and nevertheless, they have been to applied as such.

The results originate from two major parts of this work: the observations and the detailed NLTE radiative line transfer modelling, which are summarised in the following in order to answer the long outstanding questions about the Fe II and [Fe II] emission lines posed in the introduction of this thesis.

**In the observational part** (Chapter2) the time-resolved high-resolution observations of a M-type Mira sample have been presented. Quantitative data on the shapes, widths and fluxes of metallic emission lines of Fe I, Mg I, Mn I and Si I — in particular of Fe II and [Fe II] — as well as hydrogen emission lines H $\gamma$ , H $\delta$ , H $\zeta$ , H $\eta$  have been observed. Focusing on the detected permitted Fe II line (M 38) and the forbidden lines [Fe II] 6F, [Fe II] 7F, and [Fe II] 21F it has been found that they are the faintest emission lines observed with roughly gauss-like line profiles for the permitted lines, respectively square profiles for the forbidden lines. No significant line shifts have been detected. These lines have been observed at late phases around minimum visible light  $\phi \sim 0.3\text{--}0.5$  and, most importantly: they have *only* been detected in stars which have just had a bright light maximum. This indicates, that their erratic appearance may be because they require an exceptionally bright maximum to be formed. Evidence has been presented that brighter maxima are associated with stronger shock waves.

The observations have already suggested that in particular the Fe II and [Fe II] emission lines are a good diagnostic tool to analyse the thermodynamical conditions in the inner, dust-forming atmospheric layers of M-type Miras, because

- from the phase of their appearance it can be estimated that they must be originating from a region within the inner  $3 R_*$ , where roughly the dust-forming region is located, too.

- the fact that these lines show an erratic appearance gives the additional advantage to derive an upper boundary for the thermodynamical conditions in the zones of their emission.

With the **NLTE radiative line transfer modelling** (Chapter 4) the presumptions stated by the observations then have been checked, in order to develop and use the Fe II and [Fe II] emission lines as a funded diagnostic tool. Therefore, the code `nlte-feII` has been utilised (see Chapter 3), which treats the radiative transfer time-independently, spherically symmetric, and in the comoving frame formalism, using a 3-level-FeII-atom (including the permitted line: M38, 4583.84 Å and the forbidden emission line: 6F, 4417.51 Å) and calculating an equilibrium chemistry to obtain the required particle densities. The calculations have been performed on various thermo- and hydrodynamical input models, with the following results:

- (i) Preliminary studies of *stationary wind models* and models with an *artificially inserted high temperature peak* yield, that
  - high temperature peaks are essential for the formation of the Fe II and [Fe II] emission lines.
  - shock waves as a mechanism to obtain such high temperature peaks in the atmosphere consequently must be the cause for the emission lines.
- (ii) Investigations of self-consistent hydrodynamical models of shocked, extended, dusty C-type Mira atmospheres, namely of the so called *CHILD-code models* and *modified CHILD-code models*, have been accomplished. These models include a consistent treatment of hydrodynamics, thermodynamics, chemistry, dust formation and growth and of the grey radiative transfer problem. Here, in particular, the potential correlation between dust formation and the emission of Fe II and [Fe II] lines has been analysed. The outcome of these studies shows:
  - Only models with sufficiently high temperature peaks caused by the use of NLTE radiative cooling functions (*modified CHILD-code models*) lead to the emission of the Fe II and [Fe II] lines.
  - The phases of Fe II and [Fe II] line emission obtained from the modelling are in good agreement with the observational findings.
  - Dust formation and the emission of Fe II and [Fe II] lines are correlated in such a way, that the shock which induces dust formation in the innermost atmospheric layers can be analysed by the aid of these emission lines during the phase of dust growth, shortly before the formation of a new dust layer.

(iii) Detailed thermodynamical models of periodic shock waves in an oxygen-rich, dust-free gas composition (*gas-box models*) have been used as input models, in order to determine the exact thermodynamical properties in the dust-free, inner atmospheric zones, which lead to the formation of the FeII and [FeII] emission lines. Two extended parameter studies were performed, which reveal:

- There exists only one region close to the star's photosphere at  $1.2 - 1.8 R_*$  where the normalised peak fluxes of both the permitted and the forbidden FeII emission line fit the observational limits. The radial position of this region corresponds to the region estimated from the observations.
- The observed normalised peak fluxes can be modelled by a combination of the shock velocity amplitude and the pre-shock density in the following way: higher (lower) velocities lead to the formation of the observed normalised peak fluxes at lower (higher) pre-shock densities.
- The ion density of FeII is the *crucial* factor the peak fluxes. FeII emission lines can only originate from regions where FeII density is  $n_{\text{FeII}} \sim 10^5 - 10^{5.5} \text{ cm}^{-3}$ .
- From the required ion density of Fe II it can be deduced that the Fe II emission lines can only originate from the hot post-shock region.
- The appropriate pre-shock density and shock amplitude velocity for the emission of the observed Fe II and [FeII] emission lines is determined to be in the range of  $\rho_{\text{pre}} = 3 \cdot 10^{-15} - 4 \cdot 10^{-14} \text{ g cm}^{-3}$  and  $\Delta v = 20 - 30 \text{ km s}^{-1}$ .
- To summarise, the limited parameter range to produce the observed normalised peak fluxes is:

<ul style="list-style-type: none"> <li>* pre-shock density: <math>\rho_{\text{pre}} = 3 \cdot 10^{-15} - 4 \cdot 10^{-14} \text{ g cm}^{-3}</math></li> <li>* shock amplitude velocity: <math>\Delta v = 20 - 30 \text{ km s}^{-1}</math></li> <li>* position of shock front from the star: <math>R = 1.2 - 1.8 R_*</math>.</li> <li>* ionised iron density: <math>n_{\text{FeII}} \sim 10^5 - 10^{5.5} \text{ cm}^{-3}</math></li> </ul>
---

Additionally, the fact that the FeII and [FeII] emission lines occur only following a bright maximum points out that these emission lines are presumably produced by a stronger-than-normal shock. This implicates, that the absence of FeII and [FeII] emission lines in most pulsation cycles is most likely due to the shock velocity  $\Delta v$  at  $1.1 - 1.8 R_*$  being *less than* the limit of  $\sim 20 \text{ km s}^{-1}$  which the NLTE radiative transfer models require. This perhaps indicates that current hydrodynamical models such as the reference model (Schirrmacher et al. 2002), which predict FeII and [FeII] emission lines in every cycle, have shock velocities larger than those in real Miras. In that case, the current hydrodynamical models probably overestimate mass loss rates. Improved modelling of the shock waves and the NLTE radiative transfer in the post-shock region of Miras is required to confirm these suggestions.

Future work will concentrate on an improvement of the NLTE radiative transfer code as well as on an refinement of the input models.

Firstly, it is planed to achieve a better modelling of the line profiles of the FeII emission lines, in order to extract the full information given by the observed emission lines. It has to be tested, whether the deviating shapes of the calculated emission lines result from the radiative transfer calculations, e. g. a refined frequency grid could be necessary, or if possibly the neglection of the dust shells in the outer atmosphere cause this discrepancy. If the latter is the case, then the idea would be the construct a “hybrid-model” by substituting the smeared out shock front region of the modified CHILD-code models with detailed shock fronts of the gas-box calculations in order to have a detailed shock model *with* dust. Such input data should be generated in the near future and detailed radiative transfer calculations should be performed thereon.

Secondly, the FeII-model-atom should be enlarged towards a 142 level atom. Now the essential data, also including the collisional data, has kindly been provided by Dr. Anil K. Pradhan, a member of the IRON-Project<sup>1</sup>. The modification of the code will be started in the near future, in order to check the influences of higher energy levels on the modelled transitions M 38 and 6F presented in this work.

A bigger but nevertheless very promising project would be, to include model-atoms of all observed atoms and ions in the radiative transfer code and carry out investigations of a detailed time series of input models, in order to model all observed emission lines in half a pulsation cycle. The Balmer lines and the silicon line originating from deep down in the stellar atmosphere could reveal details of the shock formation, whereas e. g. the various FeI lines could provide insights into atmospheric layers close to the photosphere. This would be a challenging task, and of cause only selected and dominant lines should be modelled, but if successful such calculations will determine the history of the innermost shock on its way through  $\sim 1 - 2 R_*$ . This will give strong constraints on the hydrodynamical models and will allow to test the models according to the observations of Mira atmospheres in great details.

Regarding a wider field of astronomy than stellar astrophysics, Fe II and [Fe II] emission lines are observed in various astrophysical objects, partly in different spectral windows: They are very dominant in a variety of gaseous nebulae, such as the Orion nebula (see e. g. Osterbrock et al. 1992), can be detected in supernova remnants (see e. g. Hudgins et al. 1990, Rudy et al. 1994), are present in Seyfert galaxies (see e. g. Osterbrock 1990) and in circumstellar nebulae of luminous blue variables (see e. g. Johnson et al. 1992). It would be most interesting to develop the Fe II and [Fe II] emission lines as a *general* diagnostic tool to probe also different excitation mechanisms apart from shock fronts in various astrophysical objects.

---

<sup>1</sup><http://www.astronomy.ohio-state.edu/pradhan>

# A. Appendix

Here all observed total and peak fluxes corresponding to line profiles depicted in Figs. 2.2 - 2.19 (Sec. 2) are presented, ordered by the according atoms and ions.  $F_{\text{peak}}$  denotes the peak flux in the line in  $\text{erg cm}^{-2} \text{s}^{-1} \text{\AA}^{-1}$  and  $F_{\text{tot}}$  is the total flux in the line in  $\text{erg cm}^{-2} \text{s}^{-1}$ . Numbers followed by a colon correspond to fluxes derived by normalising to the AAVSO light curve (see Sec. 2.1.5 for details).

Table A.1.: Mg I Line Fluxes

Star	Phase	<b>Mg I</b> (M 1; 4571 Å)		<b>Mg I</b> (M 3; 3829 Å)		<b>Mg I</b> (M 3; 3832 Å)		<b>Mg I</b> (M 3; 3838 Å)	
		$F_{\text{peak}}$	$F_{\text{tot}}$	$F_{\text{peak}}$	$F_{\text{tot}}$	$F_{\text{peak}}$	$F_{\text{tot}}$	$F_{\text{peak}}$	$F_{\text{tot}}$
RR Sco	0.29	1.3-12	4.5-13	-	-	-	-	-	-
	0.48	2.9-13	6.6-14	-	-	-	-	-	-
R Aql	0.01	-	-	1.1-11	2.8-12	1.4-11	3.4-12	1.1-11	2.8-12
	0.32	2.0-12	4.8-13	-	-	-	-	-	-
	0.39	2.6-12:	7.5-13:	-	-	-	-	-	-
	0.50	6.5-13	1.7-13	-	-	-	-	-	-
R Car	-0.09	-	-	3.6-11:	1.0-11:	3.4-11:	5.7-12:	1.9-11:	3.7-12:
	0.11	-	-	2.7-11	9.6-12	3.2-11	7.2-12	3.0-11	1.5-12
	0.39	1.8-11:	3.7-12:	-	-	-	-	-	-
	0.45	6.7-12:	1.5-12:	-	-	-	-	-	-
	0.57	1.0-12	3.1-13	-	-	-	-	-	-
	0.66	4.0-13	1.4-13	-	-	-	-	-	-
R Leo	0.43	6.6-12:	1.4-12:	-	-	-	-	-	-
	0.63	9.5-13	1.8-13	-	-	-	-	-	-
	1.49	7.4-12	2.0-12	-	-	-	-	-	-
S Scl	0.52	2.6-13	6.8-14	-	-	-	-	-	-
	0.58	1.5-13	4.9-14	-	-	-	-	-	-
R Hya	0.12	9.4-12:	3.2-12:	-	-	-	-	-	-
	0.21	8.4-12	3.1-12	-	-	-	-	-	-
	0.53	1.4-12:	4.7-13:	-	-	-	-	-	-

Table A.2.: H and Si I Line Fluxes

Star	Phase	$\mathbf{H}_{\gamma}$ (4340 Å)		$\mathbf{H}_{\delta}$ (4101 Å)		$\mathbf{H}_{\zeta}$ (3889 Å)		$\mathbf{H}_{\eta}$ (3835 Å)		$\mathbf{Si\ I}$ (M 2; 4102 Å)	
		$F_{\text{peak}}$	$F_{\text{tot}}$	$F_{\text{peak}}$	$F_{\text{tot}}$	$F_{\text{peak}}$	$F_{\text{tot}}$	$F_{\text{peak}}$	$F_{\text{tot}}$	$F_{\text{peak}}$	$F_{\text{tot}}$
RR Sco	0.29	8.2-12	3.2-12	1.1-11	3.7-12	5.3-12	1.6-12	4.3-12	1.5-12	8.5-13	7.2-13
	0.58	5.0-13	2.7-13	3.5-12	1.2-12	-	-	-	-	1.2-12	6.8-13
R Aql	0.01	1.4-10	8.3-11	3.5-10	1.6-10	1.2-10	5.8-11	1.0-10	5.2-11	1.9-11	1.1-11
	0.32	3.0-12	1.6-12	3.2-12	1.0-12	1.1-12	4.9-13	1.2-12	2.8-13	-	-
	0.39	1.5-12:	1.0-12:	1.9-12:	6.2-13:	-	-	-	-	-	-
R Car	-0.16	6.1-11:	2.0-11:	1.6-10:	4.7-11:	-	-	-	-	1.9-11:	6.9-12:
	-0.09	1.1-9:	7.8-10:	1.8-9:	9.7-10:	3.1-10:	1.9-10:	1.9-10:	1.2-10:	1.2-10:	5.2-11:
	0.11	6.8-10	2.7-10	1.0-9	3.7-10	5.0-10	1.9-10	4.1-10	1.6-10	4.3-11	1.2-11
	0.39	3.7-12:	2.2-12:	-	-	-	-	-	-	-	-
S Scl	0.02	7.0-11	3.7-11	3.3-10	1.4-10	8.0-11	4.1-11	5.0-11	3.5-11	1.4-11	6.8-12
R Hya	0.08	3.0-10:	1.3-10:	2.7-10:	1.0-10:	1.7-10:	6.0-11:	8.8-11:	3.0-11:	1.8-11:	6.8-12
	0.12	2.1-10:	9.1-11:	1.1-10:	4.3-11:	9.5-11:	3.4-11:	3.2-11:	1.0-11:	2.2-11:	4.9-12:
	0.21	3.2-11	1.7-11	2.2-11	8.5-12	1.3-11	4.3-12	1.2-11	5.4-12	2.4-12	9.8-13

Table A.3.: Fe II and [Fe II] Line Fluxes

Star	Phase	$\mathbf{Fe\ II}$ (M 38 (4583 Å))		$\mathbf{[FeII]\ 6F}$ (4457 Å)		$\mathbf{[FeII]\ 7F}$ (4359 Å)		$\mathbf{[FeII]\ 7F}$ (4287 Å)		$\mathbf{[FeII]\ 21F}$ (4276 Å)		$\mathbf{[FeII]\ 21F}$ (4243 Å)	
		$F_{\text{peak}}$	$F_{\text{tot}}$	$F_{\text{peak}}$	$F_{\text{tot}}$	$F_{\text{peak}}$	$F_{\text{tot}}$	$F_{\text{peak}}$	$F_{\text{tot}}$	$F_{\text{peak}}$	$F_{\text{tot}}$	$F_{\text{peak}}$	$F_{\text{tot}}$
RR Sco	0.29	2.3-13	4.7-14	-	-	-	-	-	-	-	-	-	-
R Car	0.39	7.7-13:	5.8-13:	-	-	1.2-12:	2.5-13:	2.7-12:	5.5-13:	-	-	-	-
R Leo	1.49	2.4-13	7.3-14	2.3-13	9.0-14	5.4-13	1.4-13	7.8-13	3.0-13	2.6-13	7.9-14	5.4-13	1.4-13



Table A.4.: Fe I Line Fluxes

Star	Phase	<b>Fe I</b> (M 2; 4461 Å)		<b>Fe I</b> (M 2; 4375 Å)		<b>Fe I</b> (M 3; 4216 Å)		<b>Fe I</b> (M 42; 4307 Å)		<b>Fe I</b> (M 42; 4202 Å)	
		F <sub>peak</sub>	F <sub>tot</sub>	F <sub>peak</sub>	F <sub>tot</sub>	F <sub>peak</sub>	F <sub>tot</sub>	F <sub>peak</sub>	F <sub>tot</sub>	F <sub>peak</sub>	F <sub>tot</sub>
RR Sco	0.29	-	-	3.6-13	1.2-13	-	-	1.4-12	7.1-13	3.9-12	7.4-13
	0.48	-	-	-	-	-	-	1.3-13	4.7-14	-	-
R Aql	0.01	-	-	-	-	-	-	-	-	9.9-12	2.3-12
	0.32	-	-	-	-	-	-	9.7-13	5.0-13	2.2-12	5.1-13
	0.39	-	-	-	-	-	-	1.4-12:	5.6-13:	2.0-12:	4.3-13:
	0.50	-	-	-	-	-	-	3.5-13	1.1-13	-	-
R Car	-0.09	-	-	1.6-11:	1.6-12:	-	-	-	-	2.9-11:	6.5-12:
	0.11	-	-	2.4-11	4.4-12	-	-	-	-	4.5-11	1.0-11
	0.39	1.6-12:	2.7-13:	1.4-12:	1.7-13:	-	-	1.2-11:	5.6-12:	9.5-12:	3.5-12:
	0.45	-	-	-	-	-	-	2.1-12:	7.6-13:	1.8-12:	6.2-13:
	0.57	-	-	-	-	-	-	7.3-13	2.1-13	-	-
	0.66	-	-	-	-	-	-	2.6-13	6.6-14	-	-
R Leo	0.43	-	-	-	-	-	-	1.5-12:	2.8-13:	-	-
	0.63	-	-	-	-	-	-	4.1-13	1.0-13	-	-
	1.49	3.6-13	7.9-14	4.0-13	8.4-14	2.5-13	5.3-14	3.7-12	1.5-12	2.6-12	1.0-12
S Scl	0.02	-	-	-	-	-	-	-	-	6.5-12	1.7-12
	0.52	-	-	-	-	-	-	2.6-13	8.4-14	-	-
	0.58	-	-	-	-	-	-	1.3-13	3.9-14	-	-
R Hya	0.08	-	-	-	-	-	-	8.0-12:	3.1-12:	4.3-11:	1.1-11:
	0.12	-	-	-	-	-	-	9.8-12:	2.8-12:	1.9-11:	5.2-12:
	0.21	-	-	-	-	-	-	5.5-12	2.5-12	1.1-11	2.9-12
	0.53	-	-	-	-	-	-	2.5-12:	7.8-13:	-	-

Table A.5.: Fe I Line Fluxes continued

Star	Phase	<b>Fe I</b> ( <sub>M 73</sub> ; 3852 Å)		<b>Fe I</b> ( <sub>M 828</sub> ; 4427 Å)	
		F <sub>peak</sub>	F <sub>tot</sub>	F <sub>peak</sub>	F <sub>tot</sub>
RR Sco	0.29	4.8-12	1.2-12	4.2-13	9.2-14
R Aql	0.01	1.5-11	3.5-12	-	-
	0.32	3.2-12	9.7-13	-	-
R Car	-0.09	2.7-11:	3.9-12:	-	-
	0.11	1.1-10	2.9-11	-	-
R Leo	1.49	-	-	4.2-13	9.1-14
S Scl	0.02	8.5-12	1.9-12	-	-
R Hya	0.08	3.6-11:	6.8-12:	-	-
	0.12	1.9-11:	4.2-12:	-	-
	0.21	8.3-12	3.7-12	-	-

# Bibliography

- [1] Alexander D. R., Rypma R. L., & Johnson, H. R., 1983, ApJ 272, 773
- [2] Van Belle G. T., Dyck H. M., Thompson R. R., Benson J. A., & Kannappan S. J., 1997, AJ 114, 2150
- [3] Bessell M. S., Scholz M., & Wood P. R., 1996, A&A 307, 481
- [4] Bolick U., Richter He., & Sedlmayr E., 2002, ASP Conference Series, Stellar Atmosphere Modeling, in press
- [5] Bowen G. H., 1988, ApJ 329, 299
- [6] Cernicharo J., Alcolea J., Baudry A., & Gonzalez-Alfonso E., 1997, A&A 319, 607
- [7] Dere K. P., Landi E., Mason H. E., Monsignori Fossi B. C., & Young P. R., 1997, A&AS 125, 149
- [8] Dominik C., 1992, PhD thesis, Institut für Astronomie und Astrophysik, TU-Berlin, Germany
- [9] G. Engeln-Müllges und F. Uhlig, 1996, Numerical Algorithms with C, Springer Verlag
- [10] Feuchtinger M. U., Dorfi E. A., & Höfner S., 1993, A&A 273, 513
- [11] Fleischer A. J., Gauger A., & Sedlmayr E., 1992, A&A 266, 321
- [12] Fox M. W., Wood P. R., & Dopita M. A., 1984, ApJ 286, 337
- [13] Fuhr J. R., Martin G. A., & Wiese W. L., 1988, J. Phys. Chem. Ref. Data 17, Suppl.4.
- [14] Groenewegen M. A. T., Baas F., Blommaert J. A. D. L., Stehle R., Josselin E., & Tilanus, R. P. J., 1999, A&AS 140, 197
- [15] Habing H., 1996, A&AR 7, 97
- [16] Hinkle K. H., 1978, ApJ 220, 210
- [17] Hinkle K. H., Hall D. N. B., & Ridgway S. T., 1982, ApJ 252, 697

- [18] Hinkle K. H., Scharlach W. W. G., & Hall D. N. B., 1984, ApJS 56, 1
- [19] Hofmann K.-H., Scholz M., & Wood P. R., 1998, A&A 339, 846
- [20] Höfner S., & Dorfi E., 1997, A&A 319, 648
- [21] Höfner S., 1999, A&A 346, L9
- [22] Hudgins D., Herter T. & Joyce R. J., 1990, ApJ 354, L57
- [23] Huguet E., Gillet D. & Lafon, J.-P. J, 1992, A&A 255, 233
- [24] Jacob A. P., Bedding T. R., Roberts J. G. & Scholz M., 2000, MNRAS 312, 733
- [25] Jeong K. S., 2000, PhD thesis, Institut für Astronomie und Astrophysik, TU-Berlin, Germany
- [26] Johnson D. R. H. , Barlow M. J., Drew J. E. & Brinks E., 1992, MNRAS 255, 261
- [27] Joy A. H., 1947, ApJ 106, 288
- [28] Joy A. H., 1954, ApJS 1, 39
- [29] Jura, M., 1986, Irish astr. J. 17, 322
- [30] Loup, C., Forveille, T., Omont, A., & Paul, J. F., 1993, A&AS 99, 291
- [31] Mattei J. A., Mayer E. H., & Baldwin M. E., 1980, Sky Telesc. 60, 180
- [32] Merrill P. W., 1945, ApJ 102, 347
- [33] Merrill P. W., 1946a, PASP 58, 304
- [34] Merrill P. W., 1946b, ApJ 103, 27
- [35] Merrill P. W., 1947a, ApJ 105, 360
- [36] Merrill P. W., 1947b, ApJ 106, 274
- [37] Merrill P. W., 1958, *Lines of the Chemical Elements In Astronomical Spectra*, Carnegie Institution of Washington Publication 610, Second Printing
- [38] Mihalas D., 1978, *Stellar Atmospheres*, W. H. Freeman and Company, Second Edition
- [39] Mihalas D., & Weibel Mihalas B., 1999, *Foundation of Radiation Hydrodynamics*, Dover Publications, corrected reprint of first edition by Oxford University Press 1984
- [40] Mihalas D., Kunasz P. B., & Hummer D. G., 1975, ApJ 202, 46

- [41] Miller G. E., & Scalo J. M., 1979, ApJS 41, 513
- [42] Nogami D., Kato T., Baba H., & Kunjaya C., 1997, Electronic Publishing, Now and the Future, Joint Discussion 12, 23rd meeting of the IAU, Kyoto, Japan
- [43] Osterbrock D. E., Shaw R. A. & Veilleux S., 1990, ApJ 352, 561
- [44] Osterbrock D. E., Tran H. D. & Veilleux S., 1992, ApJ 389, 305
- [45] Puls J., 1991, A&A 248, 581
- [46] Reid M. J., & Dickson D. F., 1976, ApJ 209, 505
- [47] Richter He., & Wood P. R., 2001, A&A 369, 1027
- [48] Richter He., Wood P. R., Woitke P., Bolick U. & Sedlmayr E., 2002a, A&A, submitted
- [49] Richter He., Wood P. R., Woitke P., Bolick U., & Sedlmayr E., 2002b, ASP Conference Series, Stellar Atmosphere Modeling, in press
- [50] Richtmyer R. D., & Morton K. W., 1967, in John Wiley & Sons, New York, 2nd edition
- [51] Rudy R. J., Rossano G. S., & Puetter R. C., 1994, ApJ 426, 646
- [52] Rybicki G. B., & Hummer D. G., 1991, A&A 245, 171
- [53] Rybicki G. B., & Hummer D. G., 1992, A&A 262, 209
- [54] Schirmacher V., 2000, masters thesis, Institut für Astronomie und Astrophysik, TU-Berlin, Germany
- [55] Schirmacher V., Woitke P., & Sedlmayr E., 2002, A&A in preparation
- [56] Scholz M., & Tsuji T., 1984, A&A 130, 11
- [57] Thackeray A. D., 1937, ApJ 86, 499
- [58] Wallerstein G., 1975, ApJ S 291, 375
- [59] Wallerstein G., & Knapp, G. R., 1998, ARAA 36, 369
- [60] Willson L. A., 1976, ApJ 205, 172
- [61] Willson L. A., 1982, in *Pulsations in Classical and Cataclysmic Variable Stars*, pp. 269, Cox, J. P. and Hansen, C. J. (Boulder, CO : JILA)
- [62] Winters J. M., 1994, PhD thesis, Institut für Astronomie und Astrophysik, TU-Berlin, Germany

- [63] Winters J. M., Le Bertre T., Jeong K. S., & Helling Ch., Sedlmayr E., 2000a, A&A 361, 64
- [64] Winters J. M., Keady J. J., Gauger A., & Sada P. V., 2000b, A&A 359, 651
- [65] Woitke P., Krueger D., & Sedlmayr E., 1996a, A&A 311, 927
- [66] Woitke P., Goeres A., & Sedlmayr E., 1996b, A&A 313, 217
- [67] Woitke P., 1997, PhD thesis, Institut für Astronomie und Astrophysik, TU-Berlin, Germany
- [68] Woitke P., & Sedlmayr E., 1999, A&A 347, 617
- [69] Wood P. R., 1979, ApJ 227, 220
- [70] Wood P. R., 1987, in *Stellar Pulsation*, eds. A. N. Cox, W. M. Sparks & S. G. Starrfield (Springer-Verlag: Berlin), Lecture Notes in Physics vol. 274, p.250
- [71] Young K., 1995, ApJ 445, 872

## Acknowledgment

This work would not have been possible without the help of some people who have participated in its formal performance and others who volunteered to take part in its realisation and supported me. I owe them sincere gratefulness.

I wish to thank Prof. Dr. Erwin Sedlmayr for being my supervisor and for the possibility to work in his research group. His inspiring comments were always very important to me.

Piv. Doz. Dr. Jens Peter Kaufmann I would like to thank for being the second referee of this thesis and Prof. Dr. G. von Oppen I wish to thank for agreeing to be the chairman of the board of examiners.

A very special thanks goes to Dr. Peter R. Wood. Not only did he enable the observational part of my thesis with his collaboration, but also our intense and detailed discussions about the theoretical modelling inspired me enormously.

In particular, I wish to thank Dipl.-Phys. Uwe Bolick who provided the first version of the radiative transfer code which I then developed further for my purposes; without him my work would not have succeeded so quickly.

Furthermore, I want to thank all my colleagues who participated in my work by supporting me with their thermo- and hydrodynamical models:

Dr. Jan Martin Winters I thank for the stationary wind models and CHILD-code models, but also for the discussion we had about the first results of my parameter studies.

I also wish to thank Dipl.-Phys. Vasco Schirrmacher for his work concerning the modified CHILD-code models, which he kindly calculated especially for the stellar parameters I needed. Also a big thanks for the many fruitful discussions we had about the hydro-models and for reading this thesis for corrections.

Another thanks goes to Dr. Peter Voitke for providing the code for the detailed shock-front calculations and for the helpful discussions in the first half of the time of my dissertation.

A very special thanks goes to Dr. Beate Patzer, who not only helped me enormously with the corrections of this thesis, but who always supported me with her advice along the way of my dissertation.

I also would like to thanks Dipl.-Phys. Astrid Wachter and Dr. Michael Hegemann for reading this thesis for corrections.

Last but not least I wish to thank all other colleagues in the Zentrum für Astronomie und Astrophysik for having an “open door” when I needed help.

This work was partly supported by the German Deutscher Akademischer Austauschdienst, DAAD with a HSP III grant, project number D/99/15656 and by the Deutsche Forschungsgemeinschaft, DFG project number SE 420/21-1, SE 420/21-2.





# Lebenslauf

## Persönliche Daten

geboren am	21. März 1971 in Berlin
Eltern	Wolfgang Richter (Dipl. Bauingenieur) Ehefrau Dagmar Richter, geb. Schreck (Industriekauffrau)
Familienstand	ledig
Staatsangehörigkeit	Deutsch

## Ausbildungsdaten

1977 - 1983	Grundschule, Grundschule am Königsgraben Berlin Lankwitz
1983 - 1990	Gymnasium, Beethoven-Oberschule Berlin Lankwitz
Juni 1990	Abschluß: Abitur
Juli 1990 - Juni 1991	Au-pair Aufenthalt in London
Oktober 1991	Beginn des Physikstudiums am Fachbereich 4 der Technischen Universität Berlin
April 1995 - März 1999	Studentische Hilfskraft mit Lehraufgaben im Institut für Atom- und Molekülphysik der TU
Oktober 1998	Abschluß des Physikstudiums: Diplom Thema der Diplomarbeit: <i>Strahlungstransport und Moleküllinienbildung in zirkumstellaren Hüllen unter der Bedingung des NLTE</i>

## Beruflicher Werdegang

Mai - Oktober 1999	DAAD HSP III grant (Doktorandenstipendium) für Auslandstudium in Australien
Jan. 2000 - Dez. 2002	Wissenschaftliche Mitarbeiterin im DFG Projekt <i>Verbotene Emissionslinien in Miras</i> am Zentrum für Astronomie und Astrophysik, TU Berlin

Berlin, den 27. Januar 2003



## Erinnerung

*Und du wartest, erwartest das Eine,  
das dein Leben unendlich vermehrt;  
das Mächtige, Ungemeine,  
das Erwachen der Steine,  
Tiefen, dir zugekehrt.  
Es dämmern im Bücherständer  
die Bände in Gold und Braun;  
und du denkst an durchfahrene Länder,  
an Bilder, an die Gewänder  
wiederverlorener Fraun.*

*Und da weißt du auf einmal: das war es.  
Du erhebst dich, und vor die steht  
eines vergangenen Jahres  
Angst und Gestalt und Gebet.*

Rainer Maria Rilke, aus "Buch der Bilder"